For Reference

NOT TO BE TAKEN FROM THIS ROOM

Ex libris
universitatis
albertaensis

QUAECUMQUE VERA

Digitized by the Internet Archive
in 2023 with funding from
University of Alberta Library

https://archive.org/details/Chiu1977

THE UNIVERSITY OF ALBERTA

AN EXPERIMENTAL STUDY OF HEATED SURFACE DISCHARGES INTO AMBIENTS WITH CROSS-CURRENTS

by

© VINCENT M.H. CHIU

A THESIS

SUBMITTED TO THE FACULTY OF GRADUATE STUDIES AND
RESEARCH IN PARTIAL FULFILMENT OF THE REQUIREMENTS
FOR THE DEGREE OF MASTER OF SCIENCE

DEPARTMENT OF CIVIL ENGINEERING

EDMONTON, ALBERTA

SPRING 1977

ABSTRACT

The effect of cross-currents on the behavior of surface heated water discharges has been studied. Six experiments have been carried out with two runs in each of the large, moderate, and small Richardson number groups. Within the range of source Richardson numbers studied, the temperature profiles in both lateral and vertical directions have been found to be similar. Attempts have also been made to correlate the variations of axial excess temperature decay, jet half-width, half-depth, and trajectory with the ratio of the jet velocity to the velocity of the cross-current.

ACKNOWLEDGEMENTS

The author wishes to express his sincere gratitude to Dr. N. Rajaratnam for his guidance, advice and constructive criticism throughout the course of this study. Thanks are due to Dr. Pande B.B. Lal for his valuable suggestions in the experimental work.

The assistance of Mr. S. Lovell, R. Gitzel, and D. McGowan in constructing and maintaining the equipment is greatly appreciated.

Special thanks are due to Dr. R. Gerard for the graphical work and to Mr. B. Berry for the cross-current velocity measurement.

The author is grateful to Miss F. Fok for her encouragement and also to the National Research council for the financial support of this study through a grant to Dr. N. Rajaratnam.

TABLE OF CONTENTS

Page

CHAPTER 1 INTRODUCTION

1.1 General 1

1.2 Growth in Electrical Energy Requirement 2

1.3 Cooling Water Requirements and Efficiencies 3

1.4 Alternate Cooling Methods 5

1.5 Description of the Problem 10

CHAPTER 2 LITERATURE REVIEW

2.1 General 12

2.2 Integral Prediction Method 14

2.2.1 Carter's Model 22

2.2.2 Hoope's Model 28

2.2.3 Motz and Benedict's Model . 35

2.2.4 Stefan and Vaidyaraman's Model 43

2.3 Stolzenbach and Harleman's Model . 50

2.4 Phenomenological Model 57

2.4.1 Paddock, Policastro, Frigo's Model 57

2.4.2 Elliott and Harkness's Model . 60

2.4.3 Asbury and Frigo's Model ... 64

CHAPTER 3 EXPERIMENTAL ARRANGEMENT AND INSTRUMENTATION

3.1 Experimental objectives 68

3.2 Experimental equipments 68

3.2.1 Model Basin and Hot Water Supply System 68

Page

3.2.2 Cross Flow 69

3.2.3 Outlet Water Collecting System 73

3.3 Instrumentation for Thermal Measurements 75

3.3.1 Thermistor Probes 75

3.3.2 Probe Calibration 77

3.3.3 Location of Thermistor Probes. 78

3.3.4 Data Acquisition System .. 80

CHAPTER 4 EXPERIMENTAL RESULTS AND ANALYSIS

4.1 General 85

4.2 Temperature Measurement 87

4.3 Cross-Flow Velocity Profiles 89

4.4 Excess Temperature Profiles 89

4.5 Similarity of Surface Temperature Profiles 94

4.6 Similarity of Temperature Profiles on the Vertical Plane Along Axis of Jet 97

4.7 Temperature Decay Along the Axis .. 104

4.8 Correlation of the Temperature Coefficient with the Velocity Ratio 110

4.9 Isotherms 116

4.10 Jet Trajectory 124

4.11 Variation of Half-Width 132

4.12 Variation of Half-Depth 142

CHAPTER 5 CONCLUSIONS AND RECOMMENDATIONS 154

REFERENCES 157

APPENDIX 162

LIST OF TABLES

Table		Page
1.1	Heat Discharge Into Canadian Waters from Power Generation and Industrial Process	6
4.1	Experimental Details	88
4.2	Values of the Temperature Coefficient C_T ..	118
4.3	Analysis of Jet Trajectory	128
4.4	Values of Spreading Ratio	143
4.5	Values of the Half-Width Coefficient C_b	147
4.6	Values of the Half-Depth Coefficient C_h	151
A-1	Calibration Equations for Thermistor Probes	163
A-2	Measured Excess Temperature Decay Along Jet Centerline on Surface	164
A-3	Measured Half-Width at Surface	165
A-4	Measured Half-Depth Along Jet Trajectory ...	166

LIST OF FIGURES

Figure		Page
1.1	Electric Energy Demand Projection in Canada up to the Year 2000	4
1.2	Electric Energy Demand Projection in U.S.A. up to the Year 2020	4
2.1	Definition Sketch	16
2.2	Ideal Model of a Velocity Distribution in a Surface Jet for Velocity U	17
2.3	Geometrical Characteristics of the Jet (From Stolzenbach and Harleman)	51
2.4	Fractional Excess Temperature vs. A/Q (From Asbury and Frigo)	66
3.1	General View on the Model Basin	70
3.2	Hot Water Supply System	71
3.3	Schematic Diagram of the Basin	72
3.4	Cross Flow System	74
3.5	Water Collecting System	76
3.6	Typical Calibration Curve for Thermistor Probes	79
3.7	Thermistor Probes	81
3.8	Data Acquisition System	82
3.9	Data Acquisition and Processing System .	84
4.1	Surface Velocity Structure of the Ambient Current	90
4.2	Flow Structure of the Ambient Current .	91
4.3	Measured Temperature Distribution on Surface for $R_{io} = 0.035$	92

Figure Page

4.4 Excess Temperature Profiles on Surface Along Jet Axis for $R_{io} = 0.035$ 93

4.5 Excess Temperature Profiles on the Vertical Plane Along the Jet Axis for $R_{io} = 0.75$ 95

4.6 Non-dimensional Temperature Profiles on Surface for $R_{io} = 1.14$ 96

4.7 Non-dimensional Temperature Profiles on Surface for $R_{io} = 0.75$ 98

4.8 Non-dimensional Temperature Profiles on Surface for $R_{io} = 0.10$ 99

4.9 Non-dimensional Temperature Profiles on Surface for $R_{io} = 0.035$ 100

4.10 Non-dimensional Temperature Profiles on Surface for $R_{io} = 0.29$ 101

4.11 Non-dimensional Temperature Profiles on Surface for $R_{io} = 0.56$ 102

4.12 Non-dimensional Temperature Profiles Along the Jet Axis for $R_{io} = 0.035$ 103

4.13 Non-dimensional Temperature Profiles Along the Jet Axis 105

4.14 Non-dimensional Temperature Profiles Along the Jet Axis 106

4.15 Upstream Excess Temperature Decay Along Jet Axis on Surface 107

4.16 Downstream Excess Temperature Decay Along Jet Axis on Surface 108

4.17 Non-dimensional Plot of Temperature Decay on Surface 109

4.18 $(\Delta T_o / \Delta T_{ma})^{3/2}$ vs. $x_1 / \sqrt{A_o}$ for Large R_{io} 112

4.19 $(\Delta T_o / \Delta T_{ma})^{3/2}$ vs. $x_1 / \sqrt{A_o}$ for Moderate R_{io} 115

Figure Page

4.20 ($\Delta T_o / \Delta T_{ma}$) vs. $x_1 / \sqrt{A_o}$ for Small R_{io} 117

4.21 Variation of Temperature Coefficients with Velocity Ratio 119

4.22 Isotherms 120

4.23 Jet Trajectories on Surface 125

4.24 Jet Trajectories on Surface 126

4.25 Variation of Angles of Deflection with Velocity Ratios 129

4.26 Non-dimensional Plot of Angles of Deflection against Velocity Ratio 130

4.27 Correlation of Richardson number and Angle of Deflection with the Velocity Ratio 131

4.28 Non-dimensional Plot of Half-Width 133

4.29 Variation of Half-Width with Distance Along Jet Axis 134

4.30 Variation of Half-Width with Distance Along Jet Axis 135

4.31 Non-dimensional Plot of Half-Width for Large R_{io} 137

4.32 Non-dimensional Plot of Half-Width for Moderate R_{io} 139

4.33 Non-dimensional Plot of Half-Width for Small R_{io} 141

4.34 Correlation of Half-Width Coefficients with the Velocity Ratio 144

4.35 Jet Expansion Ratio 145

4.36 Jet Expansion Ratio against Velocity Ratio . 146

4.37 Variation of Half-Depth with Distance Along Jet Axis 148

Figure Page

4.38 Variation of Half-Depth with Distance Along Jet Axis 149

4.39 Correlation of Half-Depth Coefficients with Velocity Ratios 152

4.40 Non-dimensional Plot of Half-Depth 153

LIST OF SYMBOLS

A_o = inlet area

b = half-width of jet

b_o = width of inlet

b_a = average half-width

b_u = upstream half-width

b_d = downstream half-width

b_T = temperature half-width

b_v = velocity half-width

C_b = half-width coefficient

C_d = pressure drag coefficient

C_f = friction drag coefficient

C_h = half-depth coefficient

C_t = temperature coefficient

h = half-depth of jet

h_o = initial jet depth

h_v = velocity half-depth

k = surface heat exchange coefficient

D_p = pressure drag

D_f = friction drag

Q_o = discharge

R_e = Reynold's number

R_{io} = source Richardson number

r_h = hydraulic radius

T = temperature at any point

T_o = jet discharge temperature

T_a = ambient temperature

T_m = jet centerline temperature

ΔT_{ma} = average excess centerline temperature

U = jet velocity

U_s = surface jet velocity

U_m = jet centerline velocity

U_o = jet discharge velocity

U_1 = cross-current velocity

V_e = lateral entrainment velocity

W_e = vertical entrainment velocity

W = wind speed

W_m = mean width

z_o = jet thickness

ρ = jet density

ρ_a = ambient density

τ_w = wind stress

α_1, α_2 = entrainment coefficients

α = velocity ratio

λ_v, λ_h = similarity parameters in vertical and horizontal direction respectively

Θ_o = initial discharge angle between jet centerline and X-axis

Θ = jet angel between centerline and X-axis

β = angle between wind direction and Y-axis

CHAPTER 1

INTRODUCTION

1.1 General

The heated water discharge from the power generating stations has certain effects on the environment. The effects are caused by the change in temperature of the lake or river which is the source of the condenser cooling water supply.

The physical properties of water, such as density, viscosity, specific weight, surface tension, vapor pressure, gas solubility and diffusion, change with temperature. Among the above mentioned properties, the dissolved oxygen in water affects greatly the aquatic life. The excessive temperature increase in the water decreases the saturation levels of oxygen, and generally causes vertical stratification which cuts down oxygen circulation to the lower layers and also increases the evaporation.

Biologically, many species of aquatic life are physiologically tolerant to a small change in temperature but will suffer greatly if temperature exceeds some critical limit. Lower forms of aquatic life, such as bacteria, algae, parasites and bacilli, can adapt to the change very easily and actually take advantage of it by multiplying rapidly. But some higher species of aquatic life, suffer most from the temperature change. Thus, the

population structure of the whole ecosystem in the waterbody gets shifted or modified to an undesirable state.

Heat addition to the waterbodies mainly comes from power plants, industry, municipal and irrigation return water. Parker and Krenkel (1969) indicate that power plants are responsible for about 75% of this waste heat discharge. The problem has been further aggravated by the increasing demand on electric power, the increasing size of the power plants, and the transition from fossil to nuclear fuel plants which have a comparatively lower thermal efficiency.

1.2 Growth in electric energy requirement

The consumption of electric energy has been rising sharply during the past decade as a result of a continuing development of the 'electric society'. Today, more household appliances are electrically powered. The growth in population, economy and the upgrading of living standards are the major factors contributing to this increasing demand.

In Canada, per capita use of electric energy is the second highest among the nations of the world. The demand has tripled during the past 25 years. In 1972, the domestic demand for electricity has increased to 231,000 million Kilowatt hours as compared to 40,000 million Kilowatt hours in 1945. In U.S., the situation is even worse as the demand is doubled every 10 years.

Figure 1.1 and Figure 1.2 show the forecast of electric energy demand in Canada (An Energy Policy of Canada, Phase I, 1973) and in U.S.A. (Parker and Krenkel, 1969) up to the years 2000 and 2020 respectively. The projected figure indicates that 1,132,000 million Kilowatt hours of electric energy must be generated to meet the demand by the end of this century in Canada.

Most of the power plants in Canada today are hydro or use fossil fuel. In 1970, hydro-power stations supplied 76% of total electricity generated in Canada and 25% in U.S.A. Because sites suitable and economical to develop for hydro-power stations in North America have been used up and sites in remote areas are not favourable due to increased transmission costs, the demand for electric power would be met mainly by the fossil fuel and nuclear power plants in the future. The present forecast indicates that a decreasing proportion of electricity will be generated from hydroelectric stations and an increasing proportion from nuclear plants by the end of this century. Hydroelectric energy production might double to about 310 billion kwh which is 30 % of the demand by the year 2000 but nuclear power plants will provide at least one-third of the total energy required.

1.3 Cooling water requirements and efficiencies

Power plants operate at a very low rate of thermal efficiency. A significant part of the heat is disposed into the waterways which causes thermal pollution. Present

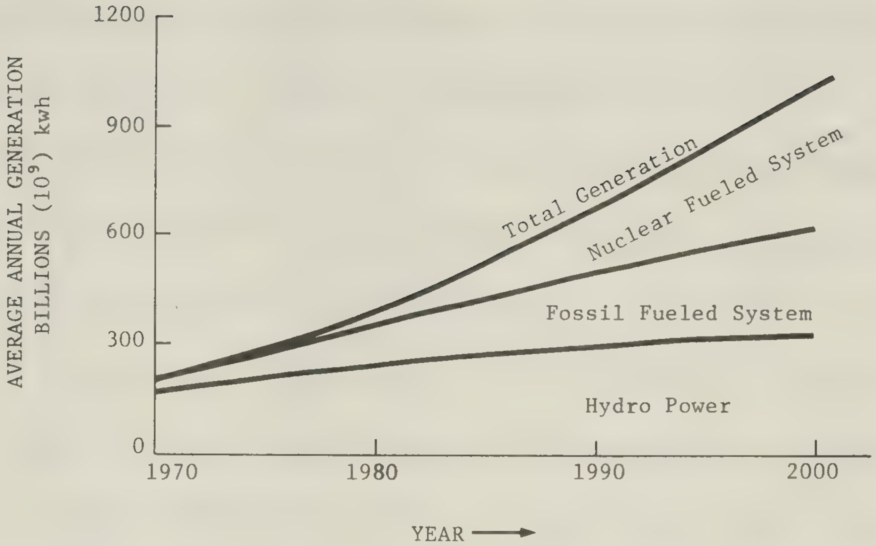

FIGURE 1.1 ELECTRIC ENERGY DEMAND PROJECTION IN CANADA UP TO THE YEAR 2000
(AN ENERGY POLICY FOR CANADA, PHASE 1)

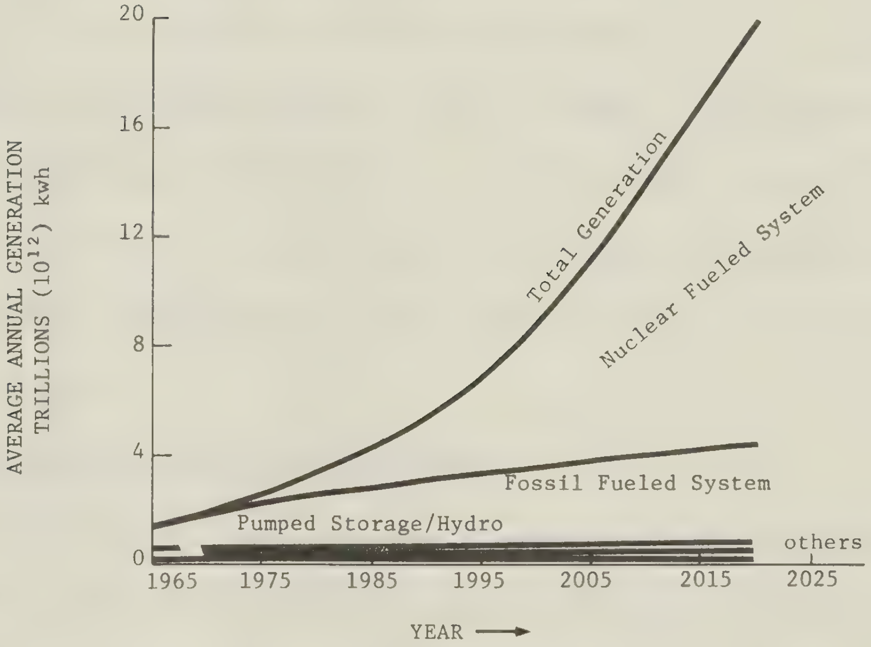

FIGURE 1.2 ELECTRIC ENERGY DEMAND PROJECTION IN U.S.A. UP TO THE YEAR 2020
(PARKER & KRENKEL)

levels of efficiency are about 40% for fossil fuel plants and 30% for nuclear plants. The efficiency is controlled by thermodynamic considerations and by the economics of power plant design. Safety requirements and the limitation of material may not permit any substantial increase in efficiency and significant technological improvements on thermal efficiency are not foreseen in the near future.

In the U.S., 50 trillion gallons of water were required for cooling purposes in 1968 and the amount is expected to be doubled by 1980. The report on Energy Policy of Canada gives the order of magnitude of known heated discharges into Canadian water from various sources for the year 1970, which are summarised on table 1.1. It also gives the projected figures for the year 2000 based on the thermal efficiency mentioned. It is clear that if the current trends are to continue, the heated discharge, and the increased evaporation will have significant effects on our environment.

1.4 Alternative Cooling Methods

The waste heat from the power plants is usually released to the atmosphere or disposed into the waterways by one of the following cooling methods:

(i) Once-through cooling system: This is so far the cheapest mode of heat disposal. Water is pumped from a lake or river and circulates through large heat exchangers. The warm water is then discharged

Table 1.1

HEAT DISCHARGE INTO CANADIAN WATERS FROM POWER GENERATION AND INDUSTRIAL PROCESSES

	Great Lakes		Other Fresh Water		Total Water		Total	
Year	1970	2000	1970	2000	1970	2000	1970	2000
Heat rejection BTU/hr x 10^{10}	3.165	60	1.65	38.6	1.21	38.1	6.025	136.7
Water loss by evaporation to dispose of added heat US gal/day x 10^{6}	69	1308	36	846	28	838	133	2292

back into the source, most often by an open channel outfall. The excessive temperature is reduced by both direct heat transfer to the atmosphere and mixing of the warm water with cooler source water. There are two distinct modes of outfall discharges:

a. Surface discharge from an effluent channel.

b. Sub-surface discharge from submerged outfalls:

    1. Single jet and

    2. Multiple jet

Because of the excessive temperature, the warmer effluent is always buoyant relative to the source waterbody. Umrath (1971) favours the scheme of heated discharge as a surface jet. His argument is that if the jet discharged as a submerged jet, most of its heat is absorbed by the cooler water as it slowly rises to the surface thus affecting the aquatic life to a maximum. But if the heated water is discharged at the surface, most of the heat will be released to the atmosphere by evaporation and relatively little is transferred down to the cooler waterbody. In the latter mode of discharge, the impact on the environment and aquatic life by the heat discharge is reduced to a minimum. For economic reasons, once-through cooling systems are generally given first considerateion.

(ii) Cooling Ponds: Cooling pond is one of the simplest methods of water cooling. Cooling of the warm

water occurs through evaporative cooling, direct transfer of heat to the air, and radiation. Low heat transfer rate and high land prices make this method unfavourable in some areas. Generally, one to two acres of land surface is required per megawatt of installed capacity. Berman (1971) suggests a heat transfer rate of 75 to 150 BTU/hr/ft^2; thus, for power plants with heat load greater than 800,000 BTU/hr, acres of land must be acquired to achieve the cooling purpose. Besides the large area acquired, other disadvantages include the requirement of blowdown of the concentrated dissolved solids and the collection of impurities due to large surface open to the atmosphere. Local meteorologic conditions such as air temperature, relative humidity, wind speed and solar radiation must be studied before the determination of the location and size of the pond.

(iii) Spray pond: The addition of spray modules to the cooling pond can increase the heat transfer rate but also increases the water loss due to evaporation. The heat transfer rate is about 4,000 to 10,000 BTU/hr/ft^2 for spray pond as compared to 75-150 BTU/hr/ft^2 for cooling ponds without spray modules. Spray ponds, however, are usually unsuitable for a cooling range greater than 18°F. In general, it is also uneconomical for large size

plants. As the size of the pond increases, the air passing by the sprays is already saturated so the sprays modules on the downwind side are not very effective.

(iv) Dry cooling towers: The basic idea of the dry tower cooling system derives from the cooling system of an automobile. The heated effluent is circulated through the radiator and the air is forced to pass the radiator by the fan. The water is cooled by heat transfer through the walls of the radiator to the air. This system can be used where fluids to be cooled are at a high temperature. It eliminates water problems such as availability, chemical treatment and corrosion; but the installation and maintenance costs are high.

(v) Wet cooling towers: This system works like the spray pond but the heated effluent is sprayed inside a large tower. Major mode of heat dissipation is evaporation which can be achieved by movement of air over the water droplets. Air movement can be obtained by using fans or by natural convection. The cooled water collects in the basin at the bottom of the tower. There are many types of wet cooling towers. The type choosen depends upon the requirements of the particular system.

In general, the choice of cooling method depends on location, available technology, economy and the objectives to be attained. In most cases, the once-through cooling system is preferred if the plant location is close to a water source because of economic reasons. Cooling ponds require too large an area and the spray ponds are not very effective for large plants. Very high capital and maintenance costs associated with cooling towers make this system unfavourable. Besides, localized ground fog problems associated with cooling ponds and cooling towers make the once-through cooling method preferable where feasible.

1.5 Description of the problem

The impact on environment by waste heat disposal has aroused unprecedented public awareness recently. Some states in U.S. have set up regulations restricting the rise in temperature in the receiving water to some distance away from the point of discharge in order to protect the environment; but some states have no restrictions at all. In Canada, investigations have been carried out in varies lakes to study the waste heat distribution and its effects on the ecological system.

The discharge of heated water on the surface of a lake spreads out like a surface buoyant jet. The temperature distribution in the discharge is considered as function of the discharge channel geometry, the initial velocity and

temperature rise, the magnitude of the ambient current, and the surface heat transfer rate. The spread of the warm water has two distinct regions given as:

(i) Near-field region or jet region where the momentum of heat discharge must be considered.

(ii) The far region where surface heat transfer aspects and ambient turbulence of the receiving water body are significant.

From the design point of view, the jet regime is of particular interest because most of the criteria are set for within this region. The outlet must be so designed that it meets the prescribed temperature criteria. Also, a complete knowledge of the temperature distribution is important for the selection of the location of the intake in order to prevent recirculation problems.

CHAPTER 2

LITERATURE REVIEW

2.1 General

The purpose of this study is to study the characteristics of heated water discharges into a large water source with small ambient current such as lakes. As the heated water is discharged into the ambient water, it creates a tangential separation surface due to the velocity difference between the jet and the ambient. This shear between the moving jet and the ambient fluid creates turbulence which travels both inwards to the jet centerline and outwards towards the ambient fluid. Eventually, this turbulent mixing action reaches the jet axis at some distance from the outfall and the jet centerline velocity begins to decrease. The region before the mixing action intrudes into the centerline is called the zone of flow establishment and is of rather limited extent. The region further downstream (in the near field) is called the zone of established flow and is generally assumed that the velocity profiles are fully developed and are similar. These two regions combined together is known as the near-field region. At some distance from outfall, the kinetic energy of the discharge would be sufficiently dissipated; the ambient turbulence dominates over the jet turbulence and governs the behavior of the jet. This region is classified as the far-field region and is

generally much larger than the near-field region. In the presence of an ambient current, the jet is forced to bend over in the direction of the ambient current due to the pressure difference created between the upcurrent and leeward sides of the jet. The curvature of the bent-over jet may be large or small depending on the velocity ratio, buoyancy and other factors. The addition of cross-flow momentum due to entrainment is the other basic mechanism causing the plume to level off. As soon as the jet bends over and becomes aligned with the ambient current, the cross-current interaction ceases for all practical purposes.

A review on the existing literature reveals that few investigations have been done on simulating the characteristics of heated water discharges into a large water source. Most investigators study a two-dimensional surface jet assuming that the entrainment in the vertical direction is negligible. This assumption may not be justified if the local Richardson number is in the small Richardson number group (i.e. less than 0.1) in which case the jet thickness increases in the longitudinal direction. Therefore, a study on the three-dimensional surface discharge with ambient current is of immediate interest and the author hopes to provide some useful experimental information towards solving this complicate problem in this study.

2.2 Integral Prediction Methods

This method is the most common approach in the model development. A set of differential equations for conservation of heat, momentum, and volume are derived for a control volume, and then integrated over the jet in the vertical and lateral directions to obtain the general expressions.

To solve these differential equations numerically, some assumptions must be made. In addition to the Boussinesq Approximation, which states that the density difference can be neglected except in terms involving gravity, velocity and temperature profiles are assumed to be similar in consecutive transverse sections. Morton (1961) states that the assumption of similar profiles suppresses all details of the transverse structure of the jet, and any profile shape can be used without loss of additional physical information. Most researchers propose a Gaussian type distribution which generally agrees well with the experimental data.

The entrainment velocity is usually related to some characteristic velocity of the jet by coefficients. Platten and Keffer (1968) proposed an expression for entrainment velocity for nonbuoyant round jets in air as:

$$V_e = \alpha_1 (U_m - U_1 \cos \theta) + \alpha_2 U_1 (\cos \theta - \cos \theta_o) \quad (2.2.1)$$

where θ_o is the angle between direction of cross flow velocity and centerline of inlet; α_1 and α_2 are entrainment coefficients which have to be determined empirically. The second term in Equation 2.2.1 is included to account for the entraining effect of internal rotation imparted to the jet by the cross-flowing current. A simpler form is adopted by Morton (1956), and Motz and Benedict (1972). They assume that the entrainment velocity is to be proportional to the magnitude of difference between some characteristic velocity in the jet and the velocity of ambient unaffected by the jet. This gives:

$$V_e = \alpha_1 (U_m - U_1 \cos \theta) \tag{2.2.2}$$

which has exactly the same form as the first term in Equation 2.2.1.

To develop the governing equations, we consider the regimes of moderate and large Richardson number (i.e. with the source Richardson number greater than 0.1). In these two regimes, the thickness of the surface jet can be assumed to be approximately constant at a very short distance from the outlet. This assumption constitutes a great simplication in analytical modeling.

Referring to Figure 2.1 and 2.2, the derived equations for conservation of volume, momentum, and heat flux for a control volume can be written as:

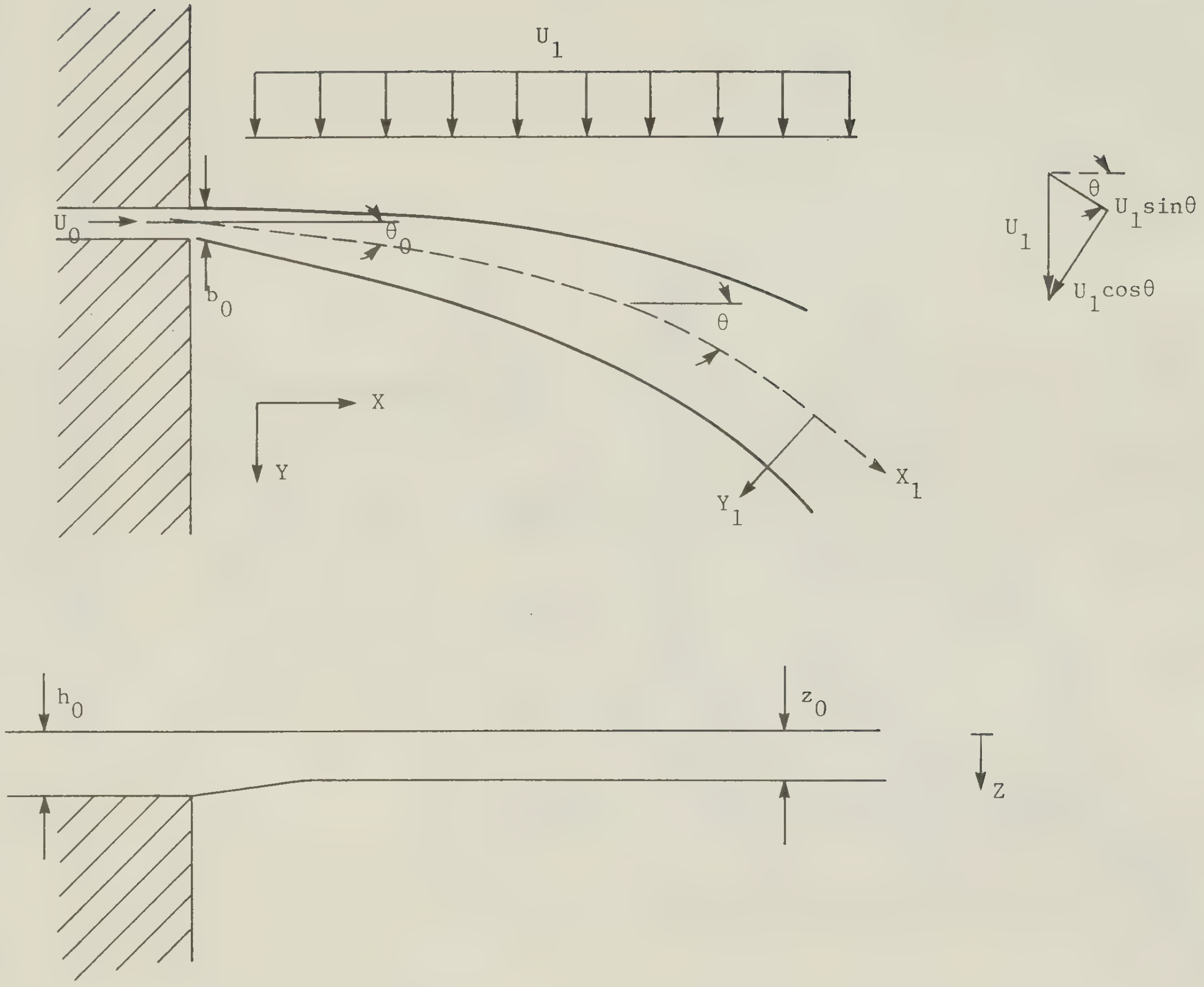
U_1
U_0
θ_0
b_0
θ
X
Y
X_1
Y_1
U_1
θ
$U_1 \sin\theta$
$U_1 \cos\theta$
h_0
z_0
Z

FIGURE 2.1 DEFINITION SKETCH

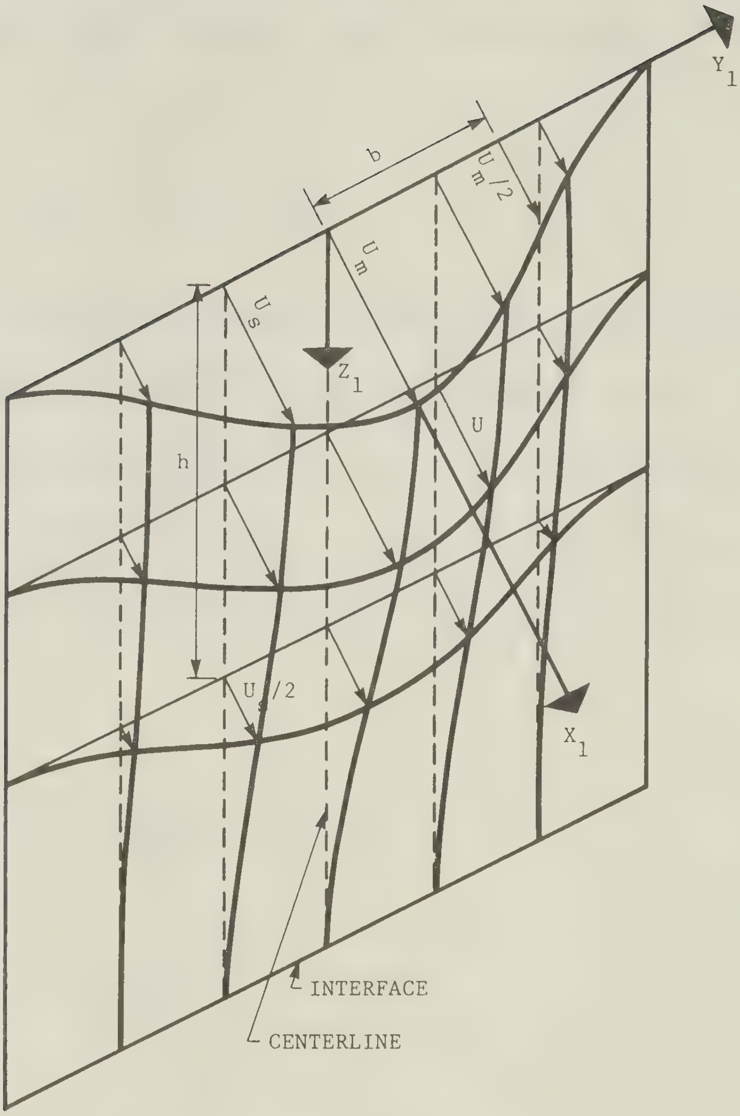
Y_1
b
$U_m/2$
U_m
U_s
Z_1
U
h
$U_s/2$
X_1
INTERFACE
CENTERLINE

FIGURE 2.2 IDEAL MODEL OF A VELOCITY DISTRIBUTION IN A SURFACE JET FOR VELOCITY U

(PANDE, 1975)

Conservation of volume flux

The rate of volume flux change in the jet between two sections along the axis should equal to the ambient flow entrained within that two sections. This gives:

$$\frac{d}{dx_1}\int_0^{\bar{b}_v}\int_0^{z_o} U\, dy_1\, dz_1 = 2\, |V_e|\, z_o \tag{2.2.3}$$

where $|V_e|$ is the depth-average entrainment velocity; $\bar{b}_v$ is the distance measured from the axis towarding to the edge to the point where the velocity is 1% of the centerline velocity and is usually taken as 2.25 times the half-width (b_v) of the same section and Z_o is the depth of the jet. Assuming:

$$\frac{U_s}{U_m} = f_1\left(\frac{y_1}{b_v}\right) = f_1(\eta) \tag{2.2.4a}$$

$$\frac{U}{U_s} = f_2\left(\frac{z_1}{h_v}\right) = f_2(\xi) \tag{2.2.4b}$$

gives

$$\frac{U}{U_m} = f_1(\eta)f_2(\xi) \tag{2.2.5}$$

where b_v and h_v are the half-width and the half-depth in the lateral and vertical directions respectively. Substituting Equation 2.2.5 into Equation 2.2.3 gives the final form of the conservation of volume flux as:

$$F_1 \frac{d}{dx_1} U_m h_v b_v = 2 \; |V_e| \; z_o \tag{2.2.6}$$

where $F_1 = \int_0^{2.25} \int_0^{2.25} f_1(\eta) f_2(\xi) \, d\eta \, d\xi = \text{constant}$

Conservation of Momentum Flux in X Direction

The momentum flux of the jet in the X-direction is balanced by the pressure drag created by the cross flow in the same direction. This gives:

$$2 \frac{d}{dx_1} \int_0^{\bar{b}_v} \int_0^{z_o} U \rho \, (U \cos \theta) \, dy_1 \, dz_1$$

$$= - C_d \frac{\rho_a U_1^2 \cos^2 \theta}{2} z_o \sin \theta \tag{2.2.7}$$

Applying the relationship as in Equation 2.2.5 to Equation 2.2.7 leads to:

$$F_2 \frac{d}{dx_1} 2 \, U_m^2 \, b_v \, h_v \cos \theta = - C_d \frac{U_1^2 \cos^2 \theta}{2} z_o \sin \theta \tag{2.2.8}$$

where $F_2 = \int_0^{2.25} \int_0^{2.25} (f_1(\eta))^2 \, (f_2(\xi))^2 \, d\eta \, d\xi$

$= \text{constant}$

note that the friction drag is neglected in the above equation.

Conservation of Momentum Flux in Y direction

The variation of the momentum flux in the Y direction can be written as:

$$2 \frac{d}{dx_1} \int_0^{\bar{b}_v} \int_0^{z_o} \rho U^2 \sin \theta \, dy_1 \, dz_1 - 2 \rho |V_e| \, z_o \, U_1 = C_d \, \rho_a \frac{U_1^2 \cos^2 \theta}{2} z_o \cos \theta \qquad (2.2.9)$$

The second term in Equation 2.2.9 is the momentum flux increased or decreased due to the entrained ambient fluid. Combining with Equation 2.2.5, the equation for the conservation of momentum flux in Y direction is:

$$2 F_2 \frac{d}{dx_1} U_m^2 \, b_v \, h_v \sin \theta - 2 V_e \, z_o \, U_1 = C_d \frac{U_1^2 \cos^3 \theta}{2} z_o \qquad (2.2.10)$$

wherein the direct contribution of wind shear stress on the water surface has been neglected.

Conservation of Heat Flux

Neglecting the heat loss on the surface, the equation for conservation of heat flux is:

$$\frac{d}{dx_1} \int_0^{\bar{b}_T} \int_0^{z_o} 2 \, \Delta T \, U \, dy_1 \, dz_1 = 0 \qquad (2.2.11)$$

where $\bar{b}_T$ is the location at which the temperature excess is about 1% of the centerline temperature excess of the same section. Further simplification leads to:

$$F_1 \frac{d}{dx_1} 2 \, \Delta T \, U_m \, b_v \, h_v = 0$$

or

$$\frac{d}{dx_1} \Delta T \, U_m \, b_v \, h_v = 0 \qquad (2.2.12)$$

where

$$\Delta T = T - T_a$$

Geometrical Equations

$$\frac{dx}{dx_1} = \cos \theta \qquad (2.2.13a)$$

$$\frac{dy}{dx_1} = \sin \theta \qquad (2.2.13b)$$

We now have four integral equations (Equation 2.2.6, 2.2.8, 2.2.10, 2.2.12) and a pair of geometrical equations (Equation 2.2.13a and Equation 2.2.13b). To proceed with the solution of these equations, we have to make further assumptions regarding the velocity and temperature distributions, and entrainment velocity.

Velocity distribution

$$\frac{U - U_1 \sin \theta}{U_m - U_1 \sin \theta} = \exp\left(-0.693 \left(\frac{y_1}{b_V}\right)^2\right) \qquad (2.2.14a)$$

Temperature distribution

$$\frac{T - T_a}{T_m - T_a} = \exp\left(-0.693 \left(\frac{y_1}{b_T}\right)^2\right) \qquad (2.2.14b)$$

Entrainment velocity

$$V_e = \alpha_1 (U_m - U_1 \sin \theta) \qquad (2.2.15)$$

Numerical methods can be used to solve the above differential equations to yield the jet trajectory, velocity and temperature decay, jet half-width and half-depth.

2.2.1 Carter's Model

Carter developes a mathematical model based on his experiments and the experimental results of Rouse on air jets. He treats the problem as a two-dimensional surface discharge with uniform cross-current and assumes top-hat distributions for velocity and temperature across the width and depth of the jet. He considers a jet in a cross-current as an obstruction in a uniform stream with some of the ambient current intruding into the jet and the

rest of the oncoming stream being deflected around the jet.

According to Rouse and Carter, the faces of the inlet exert a force downstream due to the pressure gradient across them, causing the jet to attain momentum at the orifice. The momentum equation in the Y direction can be written as:

$$d\,(\rho U_m^2\, b h_o)\sin\theta - U_1\, V_e\, \rho_a\, h_o\, dx_1 = \tfrac{1}{2}\rho_a\, C_d\, U_1^2\, h_o \cos\theta\, dx_1 \qquad (2.2.1.1)$$

Balancing the rate of change of X momentum with the X component of the pressure drag yields the momentum equation in the X direction.

$$d\,(\rho\, U_m^2\, h_o\, b)\cos\theta = -\tfrac{1}{2}\,\rho_a\, C_d\, U_1^2\, h_o \sin\theta\, dx_1 \qquad (2.2.1.2)$$

These two momentum equations are then integrated from $x_1 = 0$ to the arbitrary centerline position x_1 and then dividing Equation 2.2.1.2 by Equation 2.2.1.1 gives the slope of the centerline trajectory at the point (x,y):

$$\frac{dy}{dx} = \frac{\left[\cos \theta_o - \frac{C_d}{2\alpha^2 b_o} x\right]\left[1 - f \frac{U_1}{U_m \sin \theta}\right]}{\sin \theta_o + \frac{C_d}{2\alpha^2 b_o} y} \qquad (2.2.1.3)$$

where f is defined as the fraction of the control volume that is ambient fluid. Carter derived the equation for jet trajectory for both the zone of flow establishment and zone of established flow.

For the zone of flow establishment, Carter assumes no dilution, i.e. f = 0, which does not appear to be a correct assumption. With this assumption, Equation 2.2.1.3 is solved to yield a circular jet trajectory described by:

$$\left[y + \frac{2\alpha^2 b_o \sin \theta_o}{C_d}\right]^2 + \left[x - \frac{2\alpha^2 b_o \cos \theta_o}{C_d}\right]^2 = \left[\frac{2\alpha^2 b_o}{C_d}\right]^2 \qquad (2.2.1.4)$$

For the region of established flow, Carter assumes $U = U_1$. This assumption basically replaces the need for a continuity equation but does not seem logical. Besides, there is no hard evidence to suppport this assumption other than the author's observation that the flow

turned rapidly paralled to the ambient current. Thus, in Equation 2.2.1.3

$$1 - f \frac{U_1}{U_m \sin \theta} = 1 - f \qquad (2.2.1.5)$$

For 1 - f = constant, Carter states that the trajectory is an ellipse with the same center but with semi-major and semi-minor axis given by $2\alpha^2 b_o/C_d$ and $(1 - f)^{\frac{1}{2}} 2\alpha^2 b_o/C_d$ respectively. These axes are proved to be incorrect later by Policastro and Tokar. The decrease in temperature along the jet axis is related to dilution which Carter defines as the fraction of a unit volume that is initially part of the jet discharge; the remainder is part of the ambient stream and denoted by f. Their relationship can be expressed as:

$$1 - f = \frac{T_m - T_a}{T_o - T_a} = \frac{\Delta T_m}{\Delta T_o} \qquad (2.2.1.6)$$

Carter plots his experimental data on a log-log graph paper and shows that the equation

$$\frac{\Delta T_m}{\Delta T_o} = \left[\frac{x_1}{b_o}\right]^{-\frac{1}{4}} \qquad (2.2.1.7)$$

fits the data well. This equation also reveals that the excess centerline temperature decay has a form apparently

independent of the velocity ratio α. Data analysis gives a value 2.5 b_o as the length of the temperature flow establishment region but 3 b_o is believed to be more adequate by other researchers.

The determination of θ_o and C_d depend heavily on the measurements made by Rouse on an air jet in an air cross-current. The auther derives the expression for θ_o by balancing the pressure gradient in the Y direction with the rate of change of Y momentum across the orifice. The expression gives:

$$\sin \theta_o = \frac{1}{\alpha} \frac{C_d}{2} \tag{2.2.1.8}$$

The value of C_d has been determined as a function of α from Rouse's experimental data on boundary pressure distribution. An independent estimate of C_d can be made from the measured length of the zone of flow establishment. Since the trajectory in the region of flow establishment is described by a circle, the arc of the circle is then equal to the central angle measured in radians multiplied by the radius. Thus:

$$2.5\ b_o = \left[\frac{2\ \alpha^2\ b_o}{C_d}\right] \left[(\theta_o - \theta_c)\ \frac{2\ \pi}{360}\right] \tag{2.2.1.9}$$

or

$$\theta_o - \theta_c = \frac{225}{\pi} \frac{C_d}{\alpha^2} \qquad (2.2.1.10)$$

where θ_c is the angle at the end of the flow establishment region. Based on previous assumption that the Y velocity component in the region of established flow equals U_1, this gives:

$$\sin \theta_c = \frac{1}{\alpha} = \frac{U_1}{U_o} \qquad (2.2.1.11)$$

Solving Equation 2.2.1.8, 2.2.1.10, 2.2.1.11, yields the values for θ_o and C_d.

Carter's model is different from other models in several aspects. The drag force defined as:

$$D_p = \frac{\rho_a C_d A U_1^2}{2} \qquad (2.2.1.12)$$

is an artificiality to match theoretical jet trajectories with experimental data. Fan, and Motz and Benedict adopt the same form but with an additional term. Fan chooses

$$D_p = \frac{\rho_a C_d A U_1^2}{2} \sin^2 \theta \qquad (2.2.1.13)$$

whereas Motz and Benedict choose

$$D_p = \frac{\rho_a C_d A U_1^2}{2} \sin \theta \qquad (2.2.1.14)$$

so to cause D_p to approach zero as the jet orients itself parallel to the current. The length of flow establishment is assumed constant with respect to velocity ratio but this assumption is not supported with experimental data. The continuity equation is not used. The assumption that the Y component of jet velocity equals ambient velocity in established flow region is also a doubtful approximation especially in the vicinity of the end of the flow-establishment region for large velocity ratios.

2.2.2 Hoope's Model

Hoopes et al (1971) derive a mathematical model including direct wind stress by applying mass, momentum, and heat conservation to a control volume of the jet. The model is two-dimensional and the Richardson numbers are less than 0.1 which belongs to the small Richardson number group in our system of classification.

To develop the conservation of mass equation, the flow across a surface of the control volume perpendicular to the jet axis is considered. The increase in jet flow due to entrainment is:

$$dQ = I_1 \, z \, \frac{d\,(U_m\, b)}{dx_1} \, dx_1 \qquad (2.2.2.1)$$

in which

$$U_s = U_m \, f(y_1/b) \qquad (2.2.2.2A)$$

and

$$I_1 = \int_{-1}^{+1} f(\frac{y_1}{b}) \; d(\frac{y_1}{b}) \qquad (2.2.2.2B)$$

$f(y_1/b)$ is an assumed form for the lateral velocity distribution. The authors also assume that transverse velocity profiles are similar at all sections. This leads to

$$f(y_1/b) = \exp\,(-(\frac{y_1}{b})^2) \quad \text{for } y_1 < n \qquad (2.2.2.3A)$$

$$f(y_1/b) = \frac{U_1 \sin \theta}{U_m} \quad \text{for } y_1 > n \qquad (2.2.2.3B)$$

If $n > b$, then the evaluation of I_1 will give a value 1.49. Equation 2.2.2.3A and 2.2.2.3B describe a Gaussian distribution for $y_1 < n$ and a constant velocity for $y_1 > n$. The entrainment velocity is simply assumed to be proportional to the jet center-line velocity and the amount of fluid entrained into the control volume is:

$$dQ = V_e \ (2 \ z_o \ dx_1) = \alpha_1 \ U_m \ (2 \ z_o \ dx_1) \qquad (2.2.2.4)$$

Equating Equation 2.2.2.1 and 2.2.2.4 yields the continuity equation.

$$\frac{d \ U_m \ b}{dx_1} = \frac{2 \ \alpha_1}{I_1} \ U_m \qquad (2.2.2.5)$$

where α_1 is the entrainment coefficient. The momentum flux is expressed in X and Y direction separately. In X-direction.

$$\Sigma F_x = F_{px} + F_{sx} = \tau_w \ (2b \ dx_1) \ \sin \beta \qquad (2.2.2.6)$$

where F_{px} and F_{sx} are the net pressure and shear forces in X direction respectively. β is the angle between wind direction and Y axis. The wind stress may be expressed as

$$\tau_w = \rho_a \ C_d \ W^2 \qquad (2.2.2.7)$$

where W is the wind velocity. The authors consider only the wind shear at the water surface; the pressure force, drag force, and the centrifugal force are all neglected. Therefore

$$M_x = \rho I_2 U_m^2 bz \cos \theta \qquad (2.2.2.8)$$

in which

$$I_2 = \int_{-1}^{+1} \left(f\left(\frac{y_1}{b}\right)\right)^2 d\left(\frac{y_1}{b}\right) \qquad (2.2.2.8A)$$

If $f(y_1/b)$ is given by Equation 2.2.2.3, then I_2 will have a value of 1.20. Substituting Equation 2.2.2.7 and 2.2.2.8 into 2.2.2.6 gives the momentum equation in the X-direction.

$$\frac{d(U_m^2 b \cos \theta)}{dx_1} = \frac{2 b \sin \beta}{\rho I_2 z} \tau_w \qquad (2.2.2.9)$$

In Y direction, the momentum equation is

$$\Sigma F_y = F_{py} + F_{sy} = \tau_w (2b\ dx_1) \cos \beta = \frac{dM_y}{d_y} - \rho U_1 dQ$$

$$(2.2.2.10)$$

The last term in Equation 2.2.2.10 is the influx of momentum flux due to entrainment. Assuming

$F_{py} = 0$, thus

$$M_Y = \rho I_2 U_m^2 bz \sin \theta \qquad (2.2.2.11)$$

Solving Equation 2.2.2.7, 2.2.2.10 and 2.2.2.11 gives the final form of the momentum equation in the Y-direction as:

$$\frac{d(U_m^2 b \sin \beta)}{dx_1} = \frac{2 \tau_w \cos \beta}{\rho I_2 z} b + \frac{2 \alpha_1 U_1}{I_2} U_m \qquad (2.2.2.12)$$

Before solving the governing equations, the authors introduce three dimensionless variables. They are:

volume flux $$\gamma = \frac{z U_m b I_1}{z_o U_o b_o I_1} \qquad (2.2.2.13A)$$

momentum flux $$m = \frac{z U_m^2 b I_2}{z_o U_m b_o U_1 I_1} \qquad (2.2.2.13B)$$

centerline distance $$\xi = \frac{x_1 z U_1}{z_o U_o b_o} \frac{2\alpha_1}{I_2} \qquad (2.2.2.13C)$$

In addition, they introduce

$$h = m \cos \theta \qquad (2.2.2.13D)$$

and $$\nu = m \sin \theta \qquad (2.2.2.13E)$$

With the aid of Equation 2.2.2.13A to 2.2.2.13E, Equation 2.2.2.5, 2.2.2.9 and 2.2.2.12 can be solved numerically to yield the characteristics of the jet, i.e. U_m, b, θ, in terms of dimensionless volume and momentum flux. These characteristics equations are:

$$\frac{d\gamma}{d\xi} = \frac{m}{\gamma} \qquad (2.2.2.14)$$

$$\frac{dh}{d\xi} = \frac{\gamma^2}{m} 1_x \qquad (2.2.2.15)$$

$$\frac{d\nu}{d\xi} = \frac{\gamma^2}{m} 1_y + \frac{m}{\gamma} \qquad (2.2.2.16)$$

in which

$$1_x = 2\left(\frac{I_2}{I_1}\right)^2 \frac{\tau_w \sin\beta}{\rho\, \alpha_1\, U_1^2} \frac{U_o\, b_o\, z_o}{U_1\, z^2} \qquad (2.2.2.17A)$$

$$1_y = 2\left(\frac{I_2}{I_1}\right)^2 \frac{\tau_w \cos\beta}{\rho\, \alpha_1\, U_1^2} \frac{U_o\, b_o\, z_o}{U_1 z^2} \qquad (2.2.2.17B)$$

Applying conservation of thermal energy to the control volume gives:

$$\frac{d}{dx_1} \left(\int_{-b}^{b} U_s \, (T - T_a) z \, dy_1 \right) = - \int_{-b}^{b} K \, (T - T_a) \, dy_1 \qquad (2.2.2.18)$$

in which K is the surface heat exchange coefficient. The authors assume the similarity profile for the lateral temperature distribution as:

$$T - T_a = (T_m - T_a) \, g(\frac{y_1}{b}) \qquad (2.2.2.19)$$

Combining Equation 2.2.2.18 and 2.2.2.19 yields the conservation of heat equation.

$$T_m = \frac{Q_o}{Q} \, (T_o - T_a) \, \exp(- \frac{2K \, I_4 \, t}{I_3 \, z}) + T_a \qquad (2.2.2.20)$$

in which

$$I_3 = \int_{-1}^{+1} f(\frac{y_1}{b}) \, g(\frac{y_1}{b}) \, d(\frac{y_1}{b}) \qquad (2.2.2.21A)$$

$$I_4 = \int_{-1}^{+1} g(\frac{y_1}{b}) \, d(\frac{y_1}{b}) \qquad (2.2.2.21B)$$

$$t = \int_0^{x_1} \frac{dx_1}{U_m} \qquad (2.2.2.21C)$$

If the surface heat loss is negligible, i.e. $K = 0$, then Equation 2.2.2.20 reduces to:

$$T_m = \frac{Q_o}{Q} (T_o - T_a) + T_a \qquad (2.2.2.22)$$

A weak point in this model involves the author's analysis of entrainment. Ellison and Turner, Keffer and Baines, Monton, and Fan have all defined entrainment in terms of the difference between a characteristic jet velocity and the velocity of the moving ambient current instead of directly related to the centerline velocity as in Hoope's model. The assumption of similar profiles for velocity and temperature makes the model capable of handling only very small cross flows. They assume a linear spreading of the jet and this may not be true if the level of the ambient turbulence is low and buoyancy effects are predominant. The model also fails to handle the lack of symmetry on windward and leeward sides of the jet which is reflected in an obvious change in entrainment coefficient.

2.2.3 Motz and Benedict's Model

This steady, turbulent, two-dimensional jet

model is developed based upon the framework established by Morton, Fan, Hoopes and Carter. The argument on no vertical entrainment is discussed by Ellison and Turner in which they find that the Richardson number increases gradually to one or greater along the jet axis regardless the source Richardson number. When the Richardson number is close to or greater than unity, buoyancy forces dominate over inertia forces and entrainment of the ambient water occurs only at the sides of the jet and not to any significant extent at the bottom.

A control volume is segregated from the jet to develop the governing equations. The equation for the volume flux can be written by balancing the rate of change of volume flux and the fluid entrained.

Thus:

$$\frac{d}{dx_1}(U_m b) = \frac{2\alpha_1}{\sqrt{\pi}}(U_m - U_1 \sin\theta) \qquad (2.2.3.1)$$

The entrainment velocity is defined as:

$$V_e = \alpha_1 (U_m - U_1 \sin\theta) \qquad (2.2.3.2)$$

which is an improvement over the form used in the model

of Hoopes et al. The entrainment coefficient α_1, as in other models, has to be determined empirically. The momentum equations in the X and Y directions are:

$$\frac{d}{dx_1}(U_m^2 \, b \cos \theta) = -\frac{\sqrt{2}}{\sqrt{\pi}} \frac{C_d \, U_1^2 \cos \theta \sin \theta}{2} \qquad (2.2.3.3)$$

$$\frac{d}{dx_1}(U_m^2 \, b \sin \theta) = \frac{2\sqrt{2}\,\alpha_1}{\sqrt{\pi}} (U_m - U_1 \sin \theta) U_1 + \frac{C_d \, U_1^2 \cos^2 \theta}{\sqrt{2\pi}} \qquad (2.2.3.4)$$

respectively. The heat conservation equation is simply expressed as:

$$\frac{d}{dx_1}(U_m \, \Delta T_m \, b) = 0 \qquad (2.2.3.5)$$

and also the two geometric equations:

$$\frac{dx}{dx_1} = \sin \theta \qquad (2.2.3.6)$$

$$\frac{dy}{dx_1} = \cos \theta \qquad (2.2.3.7)$$

Thus, there are six equations which are functions of the jet axis distance x_1. Before solving the above differential equations, the temperature and velocity profiles have to be assumed and some dimensionless parameters are introduced. Motz and Benedict assume similarity in both the temperature and velocity profiles and choose an exponential form for the similarity profiles. The Gaussian profiles chosen are:

$$U = U_m \exp\left(-\left(\frac{y_1}{b}\right)^2\right) \qquad (2.2.3.8)$$

$$\Delta T = \Delta T_m \exp\left(-\left(\frac{y_1}{b}\right)^2\right) \qquad (2.2.3.9)$$

The dimensionless parameters are:

volume flux $$V = \frac{U_m\ b}{U_o\ b_o} \qquad (2.2.3.10A)$$

momentum flux $$M = \frac{U_m^2\ b}{U_o^2\ b_o} \qquad (2.2.3.10B)$$

jet axis distance $$S_1 = \frac{2\ \alpha_1}{\sqrt{\pi}} \frac{x_1}{b_o} \qquad (2.2.3.10C)$$

velocity ratio $$\frac{1}{\alpha} = \frac{U_1}{U_o} \qquad (2.2.3.10D)$$

reduced drag coefficient $$C_D{}' = \frac{C_d}{4\,\alpha_1} \qquad (2.2.3.10E)$$

geometric distance $$X = \frac{2\,\alpha_1}{\sqrt{\pi}}\,\frac{x}{b_o} \qquad (2.2.3.10F)$$

$$Y = \frac{2\,\alpha_1}{\sqrt{\pi}}\,\frac{y}{b_o} \qquad (2.2.3.10G)$$

The drag force D_p, is assumed to be related to the ambient velocity in the following form:

$$D_p = \frac{C_d\,U_1^2\,z_o}{2}\,\sin\theta \qquad (2.2.3.11)$$

With the additional information on the drag and entrainment coefficient, the authors are able to solve Equation 2.2.3.1, 2.2.3.3., 2.2.3.4, 2.2.3.5, 2.2.3.6 and 2.2.3.7 by a fourth-order Runge-Kutta method to yield the jet trajectory, width, velocity and temperature decay.

Because this model is developed only for the zone of established flow, the authors try to estimate the

length of the flow establishment. This can be done by plotting the value of temperature versus distance on log-log graph paper and finding the maximum distance up to which temperature equals the inlet temperature. Another plot on the log-log paper shows that the length of the flow establishment has a linear relationship with the velocity ratio. Another method to estimate the length of the flow establishment is by determining the jet half-width at the end of the zone of flow establishment. This can be achieved by relating the heat flux through the end section of the flow establishment to the inlet section assuming that the heat loss is negligible in the near field region. This gives:

$$2\, U_o\, T_o\, h_o\, b_o = U_o\, T_o\, z_o\, b_o' \sqrt{\pi} / \sqrt{2}$$

or $$b_o' = 1.6\, b_o \qquad (2.2.3.12)$$

where b_o' is the half-width at the end of the zone of flow establishment.

The value of α_1 and C_d has also been determined graphically by the authors. The value of C_d obtained from laboratory and field data is approximately equal to

0.5. However, the value of α_1 scatters so much that no conclusion can be drawn. Besides, no correlation between the α_1 and the velocity ratio is found.

Paddock, et al (1973) have compared the theorectical prediction by Motz and Benedict's model to the field data obtained at the Point Beach Nuclear Power Plant and Palisades Nuclear Power Plant on Lake Michigan, U.S.A. They briefly summerize the inadequancies of this model as follows:

1. Buoyant forces, as well as vertical entrainment, are ignored in the model development. For densimetric Froude number less than about 2, buoyant spreading is quite important; for densimetric Froude number exceeding about 5, a substantial amount of vertical entrainment may be expected. Consequently, the types of discharges for which the model may be used is limited. The entrainment coefficient, determined from data fitting, must actually account for spreading due to buoyancy as well as from jet entrainment.
2. Data presented by Motz and Benedict show considerable variation in the value of entrainment coefficient from one situation to another. A particularly interesting contrast is observed when one

compares the Motz-Benedict data for 90° discharge to the Romberg-Ayers lake data. Although most of the initial conditions are similar, the entrainment coefficients are different by 10. Limited field results indicate that the entrainment coefficient remains essentially constant at a particular location with changing values of velocity ratio. This behavior is consistent with laboratory findings showing α_1 to be relatively independent of α.

3. The model is actually restricted to small ambient currents. The simulation assumes that the jet velocity approaches zero at large distances normal to the jet centerline. The assumption of Gaussian profiles for temperature and velocity and the assumption of equal rates of entrainment on offshore and leeside of the jet are not valid for ambient currents that are not very small.
4. The model does not simulate unequal rates of spread for momentum and heat.
5. The model does not treat turbulent intensity in the crossflow, due to the assumption that such turbulence and its effect on mixing are negligible. Although some account of this effect may be made

in the choice of entrainment coefficient, any such treatment would be only qualitative in nature.

2.2.4 Stefan and Vaidyaraman's Model

Stefan and Vaidyaraman develope a dynamic three-dimensional jet model under the effects of wind and cross-current. The governing equations are defined as: volume flux

$$Q(x_1) = \int_{-nb}^{nb} \int_{o}^{mh} U \, dz_1 \, dy_1 \tag{2.2.4.1}$$

heat flux

$$H(x_1) = \int_{-nb}^{nb} \int_{o}^{mh} C_p \, \rho \, U \, \Delta T \, dz_1 \, dy_1 \tag{2.2.4.2}$$

momentum flux

$$M(x_1) = \int_{-nb}^{nb} \int_{o}^{mh} \rho \, U^2 \, dz_1 \, dy_1 \tag{2.2.4.3}$$

Parameters m and n in the above integrals are finite numbers. The authors propose that a value of

n = m = 3 is adequate for Gaussian type distributions in velocity and temperature. As done in other research work, the temperature and velocity profiles are considered to be similar along the jet axis and are described by:

$$\frac{U - U_1 \sin \theta}{U_m - U_1 \sin \theta} = \exp\left(-\tfrac{1}{2}\,(y_1/b)^2\right)\,\exp\left(-\tfrac{1}{2}\,(z_1/h)^2\right) \tag{2.2.4.4}$$

$$\frac{T - T_a}{T_o - T_a} = \exp\left(-\tfrac{1}{2}\,(y_1/\lambda_h\, b)^2\right)\,\exp\left(-\tfrac{1}{2}\,(z_1/\lambda_v\, h)^2\right) \tag{2.2.4.5}$$

λ_h , λ_v in Equation 2.2.4.5 are known as the similarity parameters and the authors consider that a value of 1.05 is adequate. The assumption of similarity profiles and such a low value of λ_h indicate that the model results should be applicable for small values of Richardson numbers. The authors then apply the entrainment principle with variable values of entrainment coefficients to yield the volumetric flux increases in the flow direction.

$$\frac{dQ(x_1)}{dx_1} = \alpha_1 \, (U_m - U_1 \sin \theta) \, \frac{(h + b)}{2} \qquad (2.2.4.6)$$

The entrainment velocity is assumed to be proportional to the difference between the centerline velocity and the component of the ambient velocity in the same direction. For horizontal buoyant surface jet, the entrainment is a function not only of the centerline velocity but also of the degree of stratification, hence, a variable entrainment coefficient along the jet must be used. The authors adopt an average entrainment coefficient, which is calculated by the following relationship, for each cross section:

$$\alpha_1 = (\lambda_h h + \lambda_v b)/(h + b) \qquad (2.2.4.7)$$

The horizontal entrainment coefficient λ_h is assigned an average value of 0.059 as in the plane jet. The vertical entrainment, λ_v , through the bottom part of the surface jet is inhibited by buoyancy and must be equal to or less than horizontal entrainment, depending on the overall Richardson number. The authors establish the following relationship:

$$\frac{\lambda_v}{\lambda_h} = 1.0 - 1.33 \log (6.32/\sqrt{R_i}) \qquad (2.2.4.8)$$

where

$$R_i = \left(\frac{\Delta\rho}{\rho_a}\right) g \lambda_v h/U_m \qquad (2.2.4.8A)$$

The above relationship fits experimental data of Ellison and Turner, but only apply with the range of $0.79 > R_i > 0.025$, and $0 < (\lambda_v / \lambda_h) < 1.0$.

The rate of the plume spread is broken into two parts, one is due to turbulent mixing and the other is due to buoyancy. The authors assume that these effects can be superimposed. The horizontal and vertical spreading due to turbulent mixing are expressed as:

$$\left(\frac{db}{dx_1}\right)_T = C_1\frac{(U_m - U_1 \sin \theta)}{U_m} \qquad (2.2.4.9)$$

$$\left(\frac{dh}{dx_1}\right)_T = \left(\frac{\lambda_v}{\lambda_h}\right)^{\frac{1}{2}} \left(\frac{db}{dx_1}\right)_T \qquad (2.2.4.10)$$

respectively. The lateral spreading of the jet is assumed to be the same as that for non-buoyant jet except that the absolute spreading angle is distorted by the ambient velocity. C_1 is assigned a value of 0.081 which is considerably lower than the average of 0.097 taken for non-buoyant jets. Equation 2.2.4.10 implies that the vertical and horizontal spreading ratio is proportional to the square root of the vertical and horizontal mixing ratio.

The rate of lateral spreading due to buoyancy is given by the authors as:

$$\left(\frac{db}{dx_1}\right)_B = \frac{C_2}{U_s} \left(g\, h\, \lambda_v \frac{\Delta\rho}{\rho_a}\right)^{\frac{1}{2}} \qquad (2.2.4.11)$$

in which

$$U_s = U_m \exp(-1/2) \qquad (2.2.4.11A)$$

A value of 0.4 is recommended for C_2. As the width of

the plume increases, the depth should decrease. Thus:

$$\left(\frac{dh}{dx_1}\right)_B = -\frac{h}{b}\left(\frac{db}{dx_1}\right)_B \qquad (2.2.4.12)$$

As mentioned, the authors consider the effects of turbulence and buoyancy on spreading may be additive, therefore, the total spread of the jet in the horizontal and vertical direction are:

$$\frac{db}{dx_1} = \left(\frac{db}{dx_1}\right)_T + \left(\frac{db}{dx_1}\right)_B \qquad (2.2.4.13)$$

$$\frac{dh}{dx_1} = \left(\frac{dh}{dx_1}\right)_T + \left(\frac{dh}{dx_1}\right)_B \qquad (2.2.4.14)$$

respectively.

The rate of change of heat flux is balanced by the heat loss to the atmosphere through the water surface. This gives:

$$-\frac{d\,H(x_1)}{dx_1} = K\int_{-nb}^{nb} (T - T_E)\,dy_1 \qquad (2.2.4.15)$$

in which K is the coefficient of surface heat transfer and T_E is the equilibrium temperature.

Only the wind stress on the surface and the drag forces created by the ambient flow are given consideration in the momentum flux. The wind force is:

$$F_w = 2nb\,\tau_w \tag{2.2.4.16}$$

The pressure drag exerted on the jet is:

$$D_p = C_d \; \frac{\rho(U_1 \cos\theta)^2}{2} \, h \tag{2.2.4.17}$$

and the friction drag is given by:

$$D_f = C_f \, \rho \, (U_m - U_1 \cos\theta)^2 \, (b + h)\, \pi/\sqrt{2} \tag{2.2.4.18}$$

The drag coefficient C_d in Equation 2.2.4.17 has been given a value of unity. The rate of change of momentum flux in terms of the external forces is:

$$\frac{dM}{dx_1} = D_f + F_w \cos(\beta - 90^\circ + \theta) \; \frac{dQ}{dx_1} \, \rho \, U_1 \sin\theta \tag{2.2.4.19}$$

$$\frac{dM}{dy_1} = -\frac{dQ}{dx_1} \, \rho \, U_m \cos\theta = -\frac{M}{R} + D_p - F_w \sin(\beta - 90^\circ + \theta) \tag{2.2.4.20}$$

in which β is the angle between the wind direction and the direction of the ambient current.

An examination of these equations reveals that an important forces created due to density differential between jet fluid and ambient has been ignored, thus limiting the model's applicability for small Richardson numbers only. Besides, the consideration of a friction drag when a form drag due to separation has been considered does not appear to be realistic.

2.3 Stolzenbach and Harleman's Model

Stolzenbach and Harleman use a different approach to develop a three-dimensional mathematical model for the horizontal surface discharge from a rectangular open channel. The effect of ambient current is also considered. Like in nonbuoyant jet, the authors assume an initial core region, void of shear followed by the main turbulent region; but unlike most jet analysis, the authors divide the structure of each cross section into four regions: an unsheared core region, a vertically sheared region, a horizontally sheared region, and a region sheared in both directions, as shown in Figure 2.3.

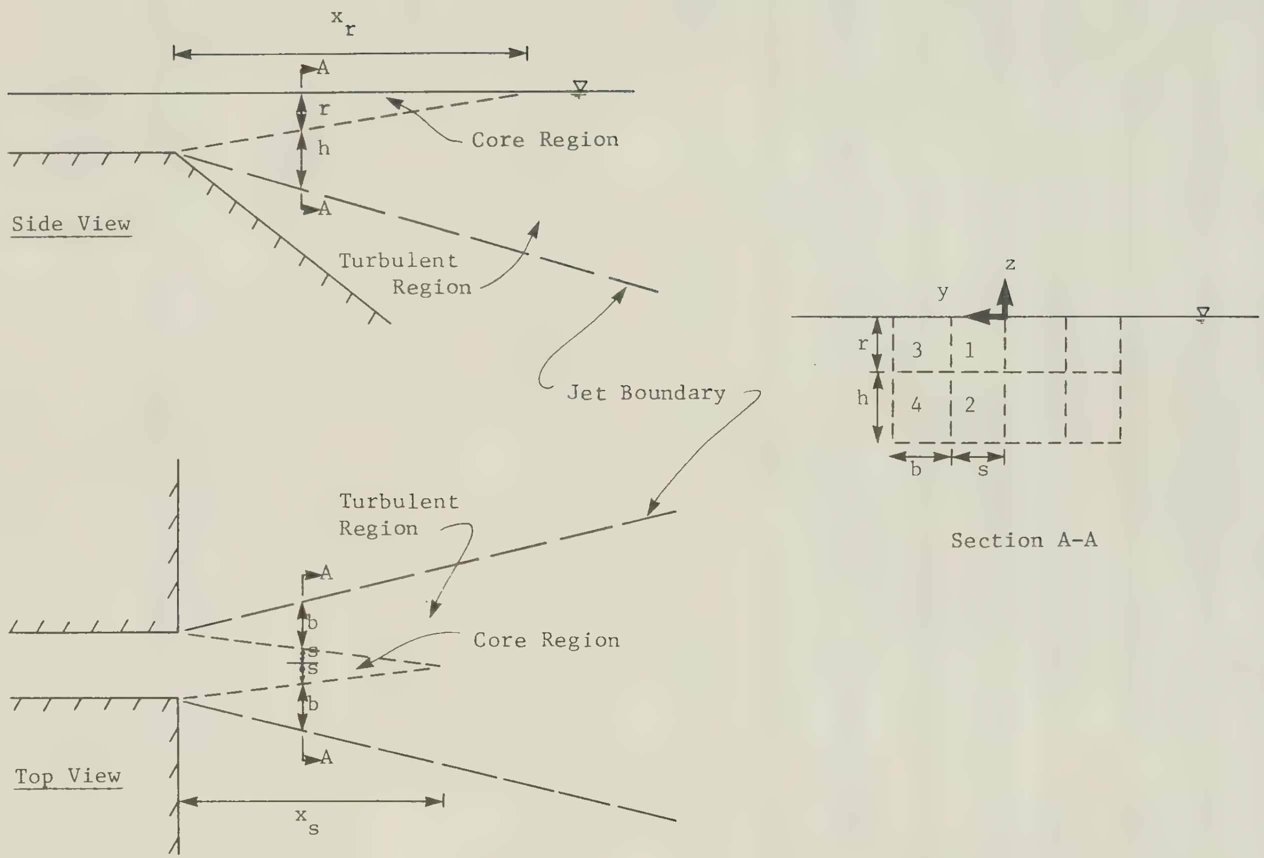
x_r
A
r
h
A
Core Region
Side View
Turbulent Region
Jet Boundary
z
y
3
1
4
2
r
h
b
s
Section A-A
Turbulent Region
A
b
s
s
b
A
Core Region
Top View
x_s

FIGURE 2.3 GEOMETRICAL CHARACTERISTICS OF THE JET
(STOLZENBACH & HARLEMAN, 1971)

To derive the basic model equations, the authors choose the integral method as in most jet analysis. The continuity equations, momentum equations in x and y direction, are written for each region along with the conservation of heat equation and the trajectory equation. The boundary conditions are different for different regions. The velocities and temperatures at each cross section are presumed to be related to the centerline values by similarity functions. The velocity and excess temperature are represented mathematically by:

$$U = U_m F_y F_z - U_1 \cos \Theta \qquad (2.3.1)$$

and

$$\Delta T = \Delta T_m T_y T_z \qquad (2.3.2)$$

respectively. The free parameters F_y, F_z, T_y and T_z are defined as:

$$\left.\begin{array}{ll}
F_y = T_y = 1.0 & 0 < |y| < s \\
F_y = f(\zeta_y),\ T_y = t(\zeta_y) & s < |y| < b + s \\
 & \zeta_y = \dfrac{|y| - s}{b} \\
F_y = T_y = 0 & b + s < |y| \\
F_z = T_z = 1.0 & -r < z < 0 \\
F_z = f(\zeta_z),\ T_z = t(\zeta_z) & -r-h < z < -r \\
 & \zeta_z = \dfrac{-z - r}{h} \\
F_z = T_z = 0 & z < -h-r
\end{array}\right] \quad (2.3.3)$$

The form of similarity functions are taken directly from Abramovich's work:

$$f = (1 - \zeta^{3/2})^2 \qquad (2.3.4)$$

and

$$t = \sqrt{f} = 1 - \zeta^{1.5} \qquad (2.3.5)$$

The authors also relate the entrainment velocities to the centerline velocity by appropriate coefficients. The lateral entrainment coefficient are determined by nonbuoyant jet theory alone and the authors assume it remains unchanged by buoyancy effects. The vertical entrainment coefficient is related to the local temperature gradient by the local Richardson number using the experimental results of Ellison and Turner. The vertical entrainment velocity ($\tilde{W}_e$) and lateral entrainment ($\tilde{V}_e$) are thus defined as:

for $z_1 = -r-h$

$$\left.\begin{array}{ll} \tilde{W}_e = W_e - U_1 \cos\theta \dfrac{dh}{dx_1} & 0 < y_1 < s \\ \tilde{W}_e = W_e \; f(\tilde{\zeta}_y) - U_1 \cos\theta \dfrac{dh}{dx_1} & s < y_1 < b + s \\ \tilde{W}_e = 0 & b + s > y_1 \end{array}\right] \qquad (2.3.6)$$

for $y_1 = s + b$

$$\tilde{V}_e = V_e + U_1 \cos \Theta \frac{db}{dx_1} \qquad -r < z_1 < \eta$$

$$\tilde{V}_e = V_e \; f(\tilde{\xi}_z) + U_1 \cos \Theta \frac{db}{dx_1} \qquad -r-h < z_1 < -r \tag{2.3.7}$$

$$\tilde{V}_e = 0 \qquad -r-h > z_1$$

With these additional equations, the authors are able to integrate the basic equations over the jet cross section to yield a system of simultaneous, first-order, nonlinear ordinary differential equations which can then be solved numerically. The complete solution may be written in non-dimensional form as:

$$\left.\begin{array}{l} \dfrac{T - T_a}{T_o - T_a} \\ \\ \dfrac{U}{U_o} \end{array}\right] = \text{function}\left(R_{io}, \frac{h_o}{b_o}, \frac{U_1}{U_o}, \frac{K}{\rho C_p U_o}, \Theta_o\right) \tag{2.3.8}$$

In this model, the adequacy of dividing the jet structure into four rectangular regions is in question. The presumed jet cross-section structure is based upon nonbuoyant jet theory but may not be valid

for buoyant jets. The division of the cross section also complicates the problem and makes the necessity of specifying the inter-regional velocities to fulfill the continuity requirement. The form of these interregional velocities are unknown and therefore must be guessed. The authors also require that no turbulent momentum transfer occurs between regions of the jet or between the jet and ambient water. This is tantamount to dropping the Reynold's stress terms in the equations of motion. As a consequence, turbulent jet diffusion has to be artificially simulated through the entrainment coefficient and similarity forms for temperature and velocity. This model is also only valid for small ambient currents in relation to the initial discharge velocity. For significant crossflow, the assumption of constant lateral entrainment coefficient may not be adequated. The negligence of the pressure drag in the governing equations also makes this model valid only for small cross-current. If the cross flow velocity is sufficiently large, the drag coefficient will no longer be negligible.

Paddock et al (1973) have compared their field data collected at Point Beach Nuclear Power Plant with Stolzenbach and Harleman's prediction, and have found

that the model predicts more rapid decay of centerline temperature and velocity. The lateral spread of the jet is much greater than the measurements. The model also tends to underpredict lateral spread in the region of flow establishment. Besides the above comments mostly associated with analytical modeling, there are practical difficulties in actually obtaining a numerical solution to the set of ordinary differential equations. For many cases, Paddock et al find that the matrix which must be reduced is nearly singular and much precision is lost in solving for the derivatives.

2.4 Phenomenological Model

2.4.1 Paddock, Policastro, Frigo's Model

Paddock et al present a phenomenological model for the prediction of jet trajectory, centerline temperature and velocity decay, half-width, half-depth and isotherm areas. The model is developed based on the measurements made at the Point Beach Unit I and Palisades Nuclear Power Plants on Lake Michigan. Velocity and temperature profiles are assumed to be similar and of the Gaussian type in the lateral direction. The

widths of these profiles are assumed to grow linearly with the distance along the jet centerline. After preliminary examination of the Point Beach data, the authors give the following equations:

For the temperature excess:

$$T = T_m (\tfrac{1}{2})^{(y_1/b_T)^2} \qquad (2.4.1.1)$$

where

$$T_m = \begin{cases} C_1 \ \Delta T_o & \text{for } x_1 \leqslant C_2 \ b_o/C_1^2 \\ T_o \left[\dfrac{C_2 \ b_o}{x_1} \right]^{\frac{1}{2}} & \text{for } x_1 > C_2 \ b_o/C_1^2 \end{cases}$$

and also $b_T = C_3 \ b_o + C_4 \ x_1$ (2.4.1.2)

in which C_1, C_2, C_3, C_4 are free parameters.

The velocity excess takes a similar form as the temperature excess:

$$U = U_m (\tfrac{1}{2})^{(y_1/b_v)^2} \qquad (2.4.1.3)$$

where $$U_m = \begin{cases} C_5 \ U_o & \text{for } x_1 \leqslant C_6 \ b_o/C_5^2 \\ U_o \left[\dfrac{C_6 b_o}{x_1} \right]^{\frac{1}{2}} & \text{for } x_1 > C_6 \ b_o/C_5^2 \end{cases}$$

$$b_v = C_7 \, b_o + C_8 \, x_1 \tag{2.4.1.4}$$

The temperature centerline trajectory is given in its parametric form:

$$x_1 = \xi \cos (R_T \, \theta_o) - \frac{k_T}{100 \, b_o} \, \xi^2 \sin (R_T \, \theta_o) \tag{2.4.1.5}$$

$$y_1 = \xi \sin (R_T \, \theta_o) + \frac{K_T}{100 \, b_o} \, \xi^2 \cos (R_T \, \theta_o) \tag{2.4.1.6}$$

The velocity centerline has a form analogous to that for the temperature centerline:

$$x_1 = \xi \cos (R_u \, \theta_o) - \frac{K_u}{100 \, b_o} \, \xi^2 \sin (R_u \, \theta_o) \tag{2.4.1.7}$$

$$y_1 = \xi \sin (R_u \, \theta_o) + \frac{K_u}{100 \, b_o} \, \xi^2 \cos (R_u \, \theta_o) \tag{2.4.1.8}$$

The free parameters C_1, C_2, C_3, C_4, C_5, C_6, C_7, C_8, R_T, R_u, K_u in the above expressions have to be determined by fitting to the field data. With the above set of equations, the authors use the minimization technique to yield the predictions. The comparison of data is presented graphically. The Point Beach jet

studies indicate that the centerline excess temperature and excess velocity ratios decay at about the same rate which can be expressed as:

$$\frac{T_m}{T_o} \simeq \frac{U_m}{U_o} \simeq \left[\frac{4.2\ b_o}{x_1} \right]^{\frac{1}{2}} \qquad (2.4.1.9)$$

Data fitting reveals that generally the temperature spreading is wider than the velocity spreading in the lateral directions. Comparing their data with other established models, the authors comment that the Pritchard model compares rather well with their limited data but is often conservative when model-data discrepancies exist. The Stolzenbach-Harleman and Prych models predict too rapid a temperature and velocity decay accompanying too great a lateral spread. The Motz-Benedict model is too sensitive to the entrainment coefficient with little consistent data available for its determination for accurate prediction. Because this model is developed based on the data taken from Lake Michigan, its applicability to other sites still remains to be tested.

2.4.2 Elliott and Harkness Model

Using set of rather extensive measurements

in Lake Ontario, Elliott and Harkness choose a predominantly phenomenological approach to develope their mathematical model for the prediction of the size, shape and orientation of the thermal plume. 19 surveys out of the original 53, which were all taken in Lake Ontario, are rejected due to instrument failure or unfavorable measurement conditions.

The authors use the least-square analysis to determine the functional relationship between the temperature and the area of an isotherm of the form:

$$\frac{T_o - T}{T_o - T_a} = C_1\left(\frac{A}{Q(T_o - T_a)}\right)^{C_2} \qquad (2.4.2.1)$$

The term $Q(T_o - T_a)$ proportional to the heat outflow rate and is included to make the expression valid for arbitrary values. But its choice of use as a scale does not seem to be adequate because the area enclosed by the isotherm also depends upon the initial momentum, aspect ratio, and the source Richardson Number. Before fitting the data to evaluate the regression coefficients C_1 and C_2, the data are segregated and grouped into three seasons: Winter, spring and fall, and summer. It was found that C_1 is equal to 0.307, 0.354,

0.336; and C_2 has the values 0.712, 0.478, 0.364 for the three seasons respectively. The authors notice that the measured isotherms exhibit a perplexing irregularity in shape that would seem to defy any systematization attempts. Measurements taken under nominally identical conditions produce radically different shapes. The plumes do, however, occupy a certain region of the lake surface near the outfall and they are elongated in the direction of flow away from the outfall. It is, therefore, postulated that a shape factor and not the shape is contained in the data. The authors thus define a mean width as:

$$W_m = \frac{A}{d} = C_3 \left(\frac{A}{(1 + F_o)^{1/2}} \right)^{C_4} \qquad (2.4.2.2)$$

where $C_3 = 0.717$ and $C_4 = 0.552$ are the values determined by fitting to the data.

It is also difficult to obtain an expression for the trajectory by using the statistical methods because the path could be expected to depend on the shape of the outfall structure, the outfall velocity, the Richardson number, the wind speed and direction, the lake current and lake bottom topography. The authors choose an analytical method which is similar to the one used by

Platten and Keffer (1968). The conservation of momentum in the direction perpendicular to ambient current is:

$$\frac{d}{dx_1} (b\ U^2 \sin \theta) = 0 \qquad (2.4.2.3)$$

Momentum increased due to entrainment is given as:

$$\frac{d}{dx_1} (b\ U^2 \cos \theta) = \frac{2\ U_1\ V_e}{I_1} \qquad (2.4.2.4)$$

$$I_1 = \int_{-1}^{+1} \exp\ (-2 (y_1/b)^2)\ d(y_1/b) = \sqrt{\pi/2} \qquad (2.4.2.4A)$$

Conservation of mass flux gives:

$$\frac{d}{dx_1} (b) = \frac{2\ V_e}{I_2} \qquad (2.4.2.5)$$

$$I_2 = \int_{-1}^{+1} \exp\ (-(y_1/b)^2)\ d(y_1/b) = \sqrt{\pi} \qquad (2.4.2.5A)$$

In the above expressions, the drag force due to lake current, wind shear, buoyant force, are all assumed to be negligible. Solving Equation 2.4.2.3,

2.4.2.4, 2.4.2.5 yields:

$$\frac{d\theta}{dx_1} = \frac{2 V_e U_1}{I_1 b_o U_o^2 \sin\theta_o} \sin^2\theta \qquad (2.4.2.6)$$

and

$$V_e = \alpha_1 (U_m - U_1 \sin\theta) + \alpha_2 U_1 (\sin\theta - \sin\theta_o) \qquad (2.4.2.7)$$

Equation 2.4.2.6, along with the assumed form for the entrainment velocity, can be solved numerically to yield the jet trajectory. The entrainment coefficients α_1 and α_2 are found by fitting the data to the theorectical solution and turn out to be equal to 0.14 and 0.6 respectively.

2.4.3 Asbury and Frigo's Model

Asbury and Frigo's study is a completely phenomenological approach in attempting to find a relationship between the plume surface area and the excess temperature based upon the field data available from other investigators. Seven sets of data, which fulfill the criterion set by the authors, are selected in this

study. The criteria are:

a. sufficient data to permit the drawing of at least three closed isotherms.
b. measurements of the intake and outfall temperatures.
c. measurement of the volumetric discharge flow rate.
d. measurement of the lake temperature.

For comparison of the data, the authors plot it in a dimensionless form, as suggested by Edinger and Polk in their study of thermal plume dispersion, which is shown in Figure 2.4. The authors explain that the discharge Q is chosen as a scaling parameter because it is difficult to assign plume-wide values to other variables and this prevents the parameterization of scaling area in terms of other variables such as ambient velocity, ambient diffusivity, and plume depth. The most straightforward parameterization of the scaling area, therefore, is of the form $A_n = Q^c$ and c is found to fit the data best when assign a value equal to one.

A study on the figure indicates the curve fits the data reasonably well. The authors feel that the sources of scatter among the data points are:

a. Large plume-to-plume variation in ambient diffusivity,

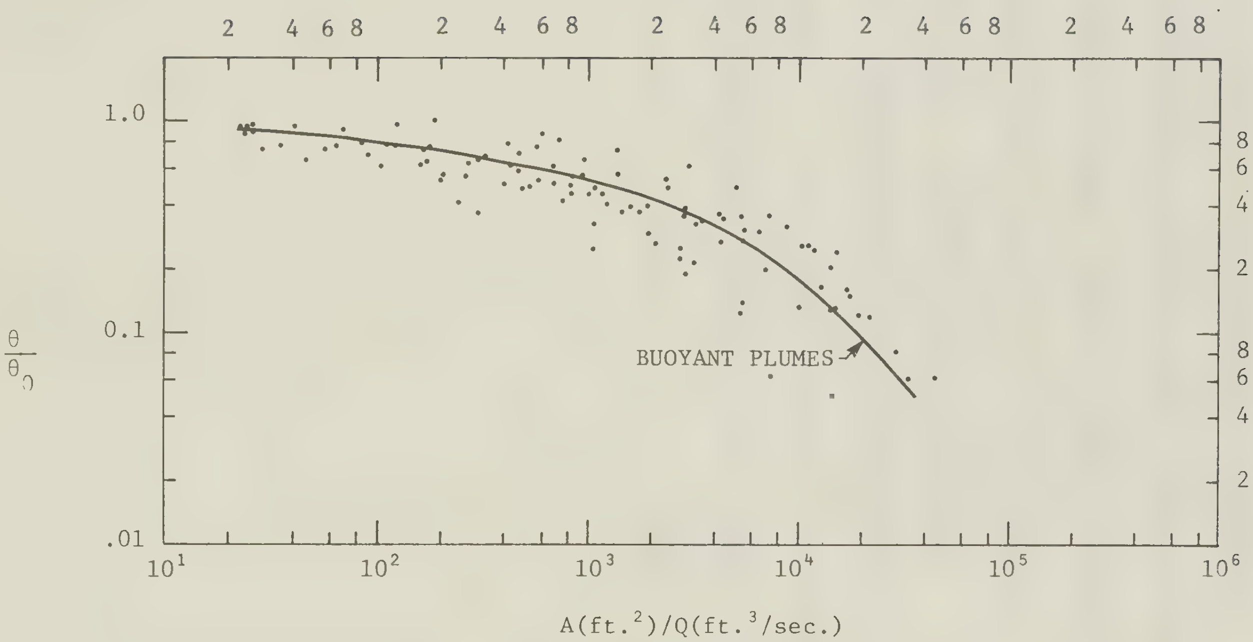

FIGURE 2.4 FRACTIONAL EXCESS TEMPERATURE $(\frac{\theta}{\theta_0})$ VS. THE RATIO $\frac{\text{SURFACE AREA (A)}}{\text{DISCHARGE FLOW RATE (Q)}}$

(ASBURY & FRIGO, 1971)

ambient velocity and plume depth. Although the magnitude of the scaling area should be strongly dependent upon them, these variables have not been included in the parameterization.

b. Inaccurate plume areas, especially in the far-field region, where plume meandering can produce significant errors in the mapping of thermal plumes.

c. Different outfall geometries.

d. The parameterization A_n/Q may not be the best choice. There may exist a more suitable parameterization, which would lead to a better consistent grouping of the data.

CHAPTER 3

EXPERIMENTAL ARRANGEMENT AND INSTRUMENTATION

3.1 Experimental Objectives

The experiments were carried out at the T. Blench Hydraulic Laboratory at the University of Alberta. This is an experimental study on the heated water discharges into a lake with weak and moderate cross-currents. Six experiments with different Richardson numbers and cross-current intensities were studied. Besides the measurement of the surface temperature , the temperature field in the vertical plane along the jet axis was also recorded. The objectives of this study are:

(i) to investigate the effect of cross flow on the axis of the jet.

(ii) to determine the centerline temperature decay.

(iii) to determine the similarity of temperature profiles in both the vertical and lateral direction.

(iv) to study whether the present theories on surface buoyant jets without cross flow can apply to the same situation with cross-currents.

3.2 Experimental Equipment

3.2.1. Model Basin and Hot Water Supply System

The model basin is 50' - 00" long, 15' - 00" wide,

and 2' - 00" deep with a horizontal floor. The side walls were constructed with 16" x 6" x 8" hollow concrete blocks. The inside of the walls was painted to prevent water leakage. A general view on the basin is shown in Figure 3.1. At one end of the basin, two identical inlet channels were constructed, 4.7 feet apart from center to center. One channel was built 2.8 feet from one wall to its center and the other was centrally located with respect to the basement. These inlet channels are 5 feet long, 1.4 feet wide and 2.0 feet deep. The thermal effluent was supplied by a water heater which has a burner input of 900,000 BTU and coupled with a pump, has a maximum capacity of 60 gpm at a constant temperature of up to 130°F. (Figure 3.2 shows the water heater). The heated water was discharged into the inlet chamber from the bottom and then passed over a V-notch to the inlet canal before entering the basin. The V-notch was used to measure the flow rate. A 2" diameter telescopic pipe for overflow was fixed in the inlet chamber to maintain a constant head over the V-notch. The invert of the inlet canal was 14" from the floor. The schematic diagram of the whole system is shown in Figure 3.3.

3.2.2 Cross-Flow

The cross flow was created by a series of closely

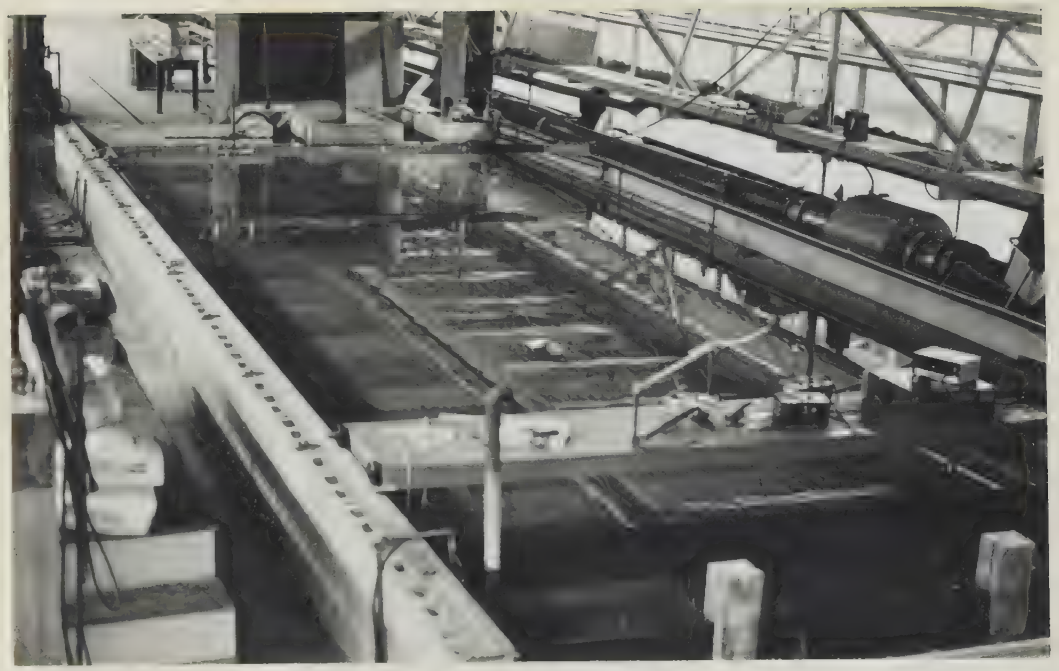

Figure 3.1 General View on the Model Basin

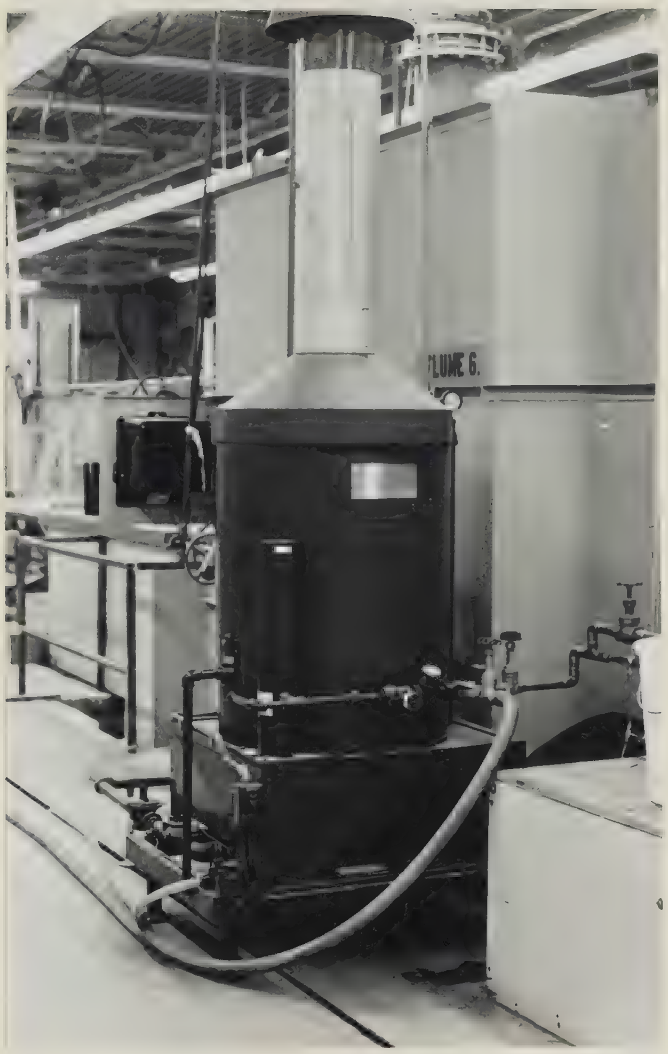

Figure 3.2 Hot Water Supply System

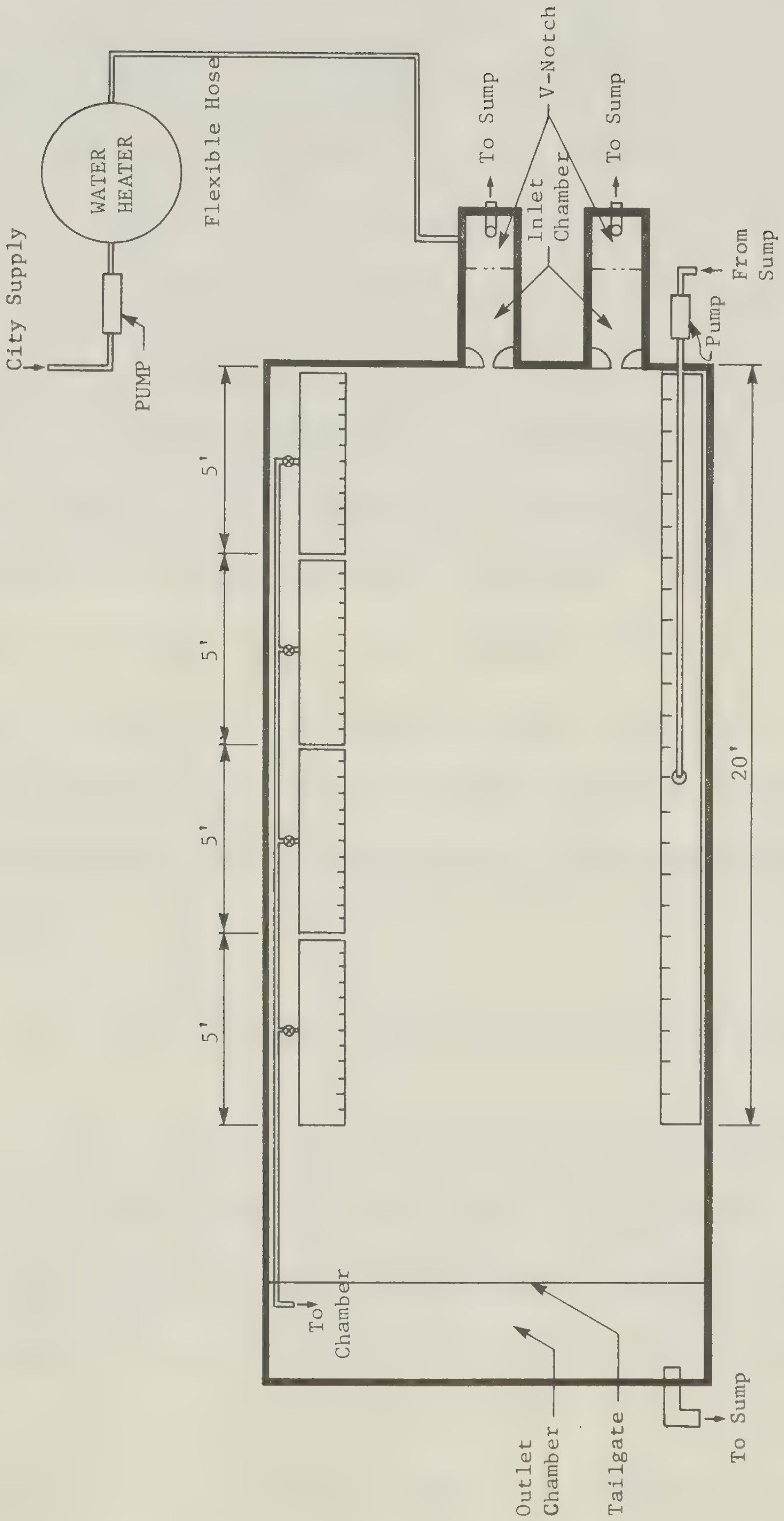
City Supply
PUMP
WATER HEATER
Flexible Hose
To Sump
V-Notch
To Sump
Inlet Chamber
From Sump
Pump
5'
5'
5'
5'
20'
To Chamber
Outlet Chamber
Tailgate
To Sump

FIGURE 3.3 SCHEMATIC DIAGRAM OF THE BASIN (PLAN VIEW)

spaced rectangular jets. This jet effect was created by cutting seventy-nine rectangular slots of 4" x 1/16" on a 5" diameter plastic pipe which was 20 feet long. The spacing between slots was 3" from center to center. Those slots were completely submerged with the top coinciding with the water surface. The axis of the pipe was about 4" away from the inside of the wall and the jets were expected to merge together at a distance of about 10 inches from the points of discharge. The pipe was connected to a pump which was submerged in the sump. The capacity of the pump was 0.1 cubic feet per second. Figure 3.4 shows the cross flow system. In some of the later runs, the pipe from the sump to the cross flow pipe was wrapped with an electric heater wire to increase the temperature of the cross flow.

3.2.3 Outlet Water Collecting System

The outlet water was collected by two separate systems. At the end of the basin, the water flowed over 3' - 7" long and 8" high tailgates into the outlet chamber. The tailgates were constructed from marine plywood and rested on 8" high and 6" wide concrete blocks fixed on the floow. A 6" diameter pipe was fixed at the bottom of the concrete block to drain the basin. Another pipe outlet from the outlet chamber led the water collected to the sump.

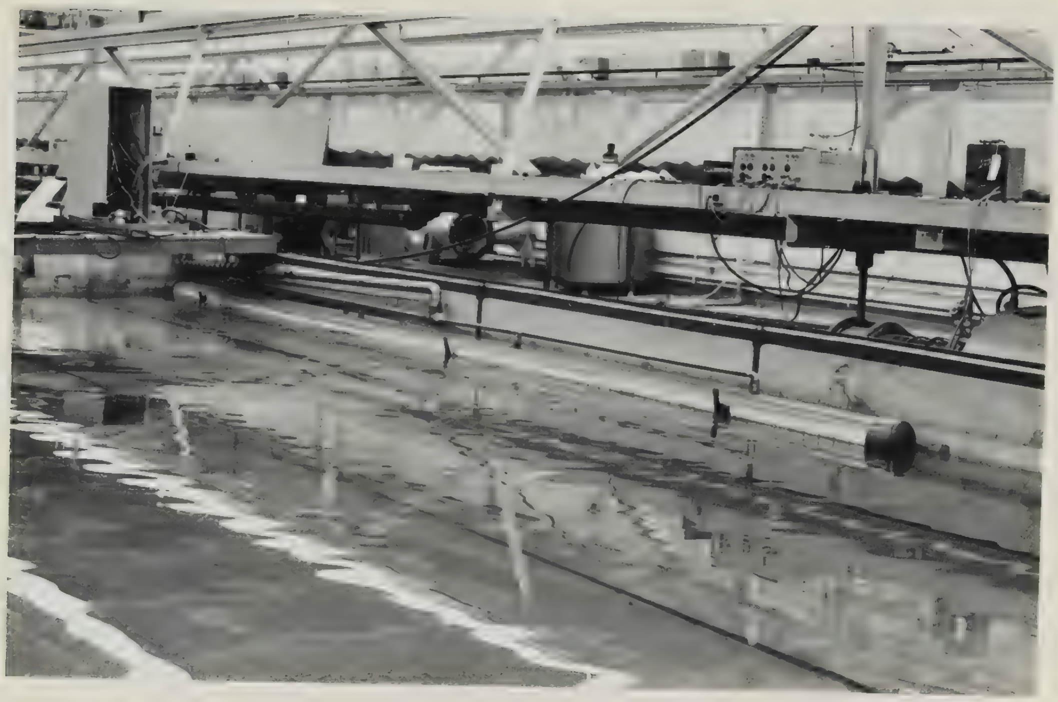

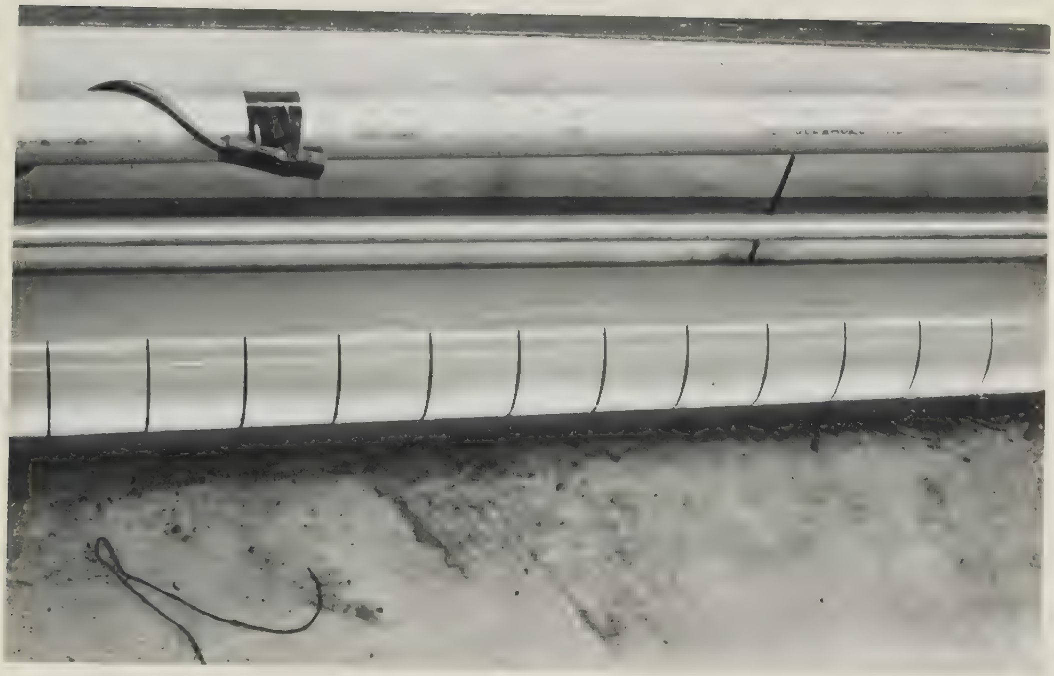

Figure 3.4 Cross flow System

The other collecting system (Figure 3.5) consisted of 4 sections of 5 feet long plastic pipes. Nineteen slots 4" x 1/16" were cut on each section and the spacing between slots was 3" from center to center. These pipes were fixed at such a height that the slots were completely submerged. These four sections of pipes were jointed by one brass pipe which extended to the outlet chamber, but each section had its own valve to control the amount of outflow. Those pipes were fixed on the side of the basin opposite to the pipe that generated the cross-current. The purpose of this system was to collect the extra discharge from the cross-current to maintain a cross-flow.

3.3 Instrumentation for Thermal Measurements

3.3.1 Thermistor Probes

Thermistor probes were used to measure the temperature of the heated water in the basin. Thermistors are resistors with a high negative temperature coefficient of resistance. As the temperature increases, the resistance goes down and vice versa. They are semi-conductors of ceramic material made by sintering mixtures of metallic oxides such as manganese, nickel, cobalt, copper, iron and uramium. Their electrical characteristics can be controlled by varying the type of oxide used and the physical

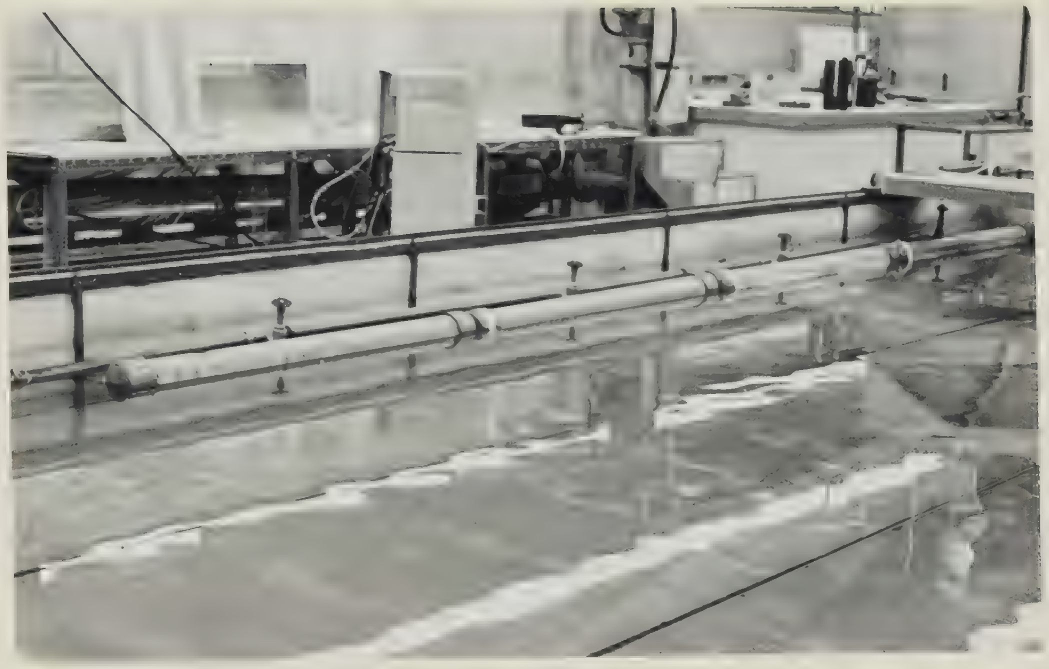

Figure 3.5 Water Collecting System

size and configuration of the thermistor.

The thermistors used in these measurements were glass-covered probes (code number GB 32P2) supplied by Fenwal Electronics, Framingham, Massachusetts. They are 2 inches in length, 0.012 inches in diameter and the lead material is Dumet. They can be used satisfactorily up to 1000°F, but the manufacturer suggests that for maximum stability, operating temperature should not exceed 600°F which well covered the temperature range in our experiments.

3.3.2 Probe Calibration

The calibration of the probes was done in a water bath. Thermistors were submerged in water and the water temperature was measured by a quartz-thermometer (model HP-2801A). Such a thermometer monitors the frequency changes of quartz crystal oscillation. Because the quartz thermometer converts temperature into frequency rather than into resistance or voltage, it is free of the problem of lead resistance and noise pickup inherent in other types of temperature measuring systems. The temperature of the water was varied and the response of the thermistors was read from the digital voltmeter (model HP-3480B). Non-linear least square technique was adopted to fit an equation, which converted the voltage reading into temperature.

A typical calibration curve for the themistor is given in Figure 3.6. The calibration equations are given in appendix.

3.3.3 Location of themistor probes

Eighteen probes were positioned at different locations to measure the temperature. Sixteen of them were mounted on a rake trolley (Figure 3.7) but the first and the last probes were not connected to the data acqisition system. The rake trolley was powered by an electric motor to move in the vertical and lateral directions. Safety limit switches were installed in both directions to avoid any possible damage to the system. The glass probes were mounted on brass tubes, 1.5 feet long, spaced 3 inches from center to center. Two 1.6 feet long solid brass tubes were also mounted on the same rake to avoid damage to the probes due to accidental impact on the bottom of the basin. In order to locate the probe system along the jet, the rake trolley was mounted on another trolley that could be moved manually in the longitudinal direction. One probe was mounted at the inlet and the other was positioned by the side wall, and they were used to measure the inlet and cross flow temperatures respectively. The location of the rake was sensed electronically and the coordinates were punched on the paper tape along with thermistor probe readings.

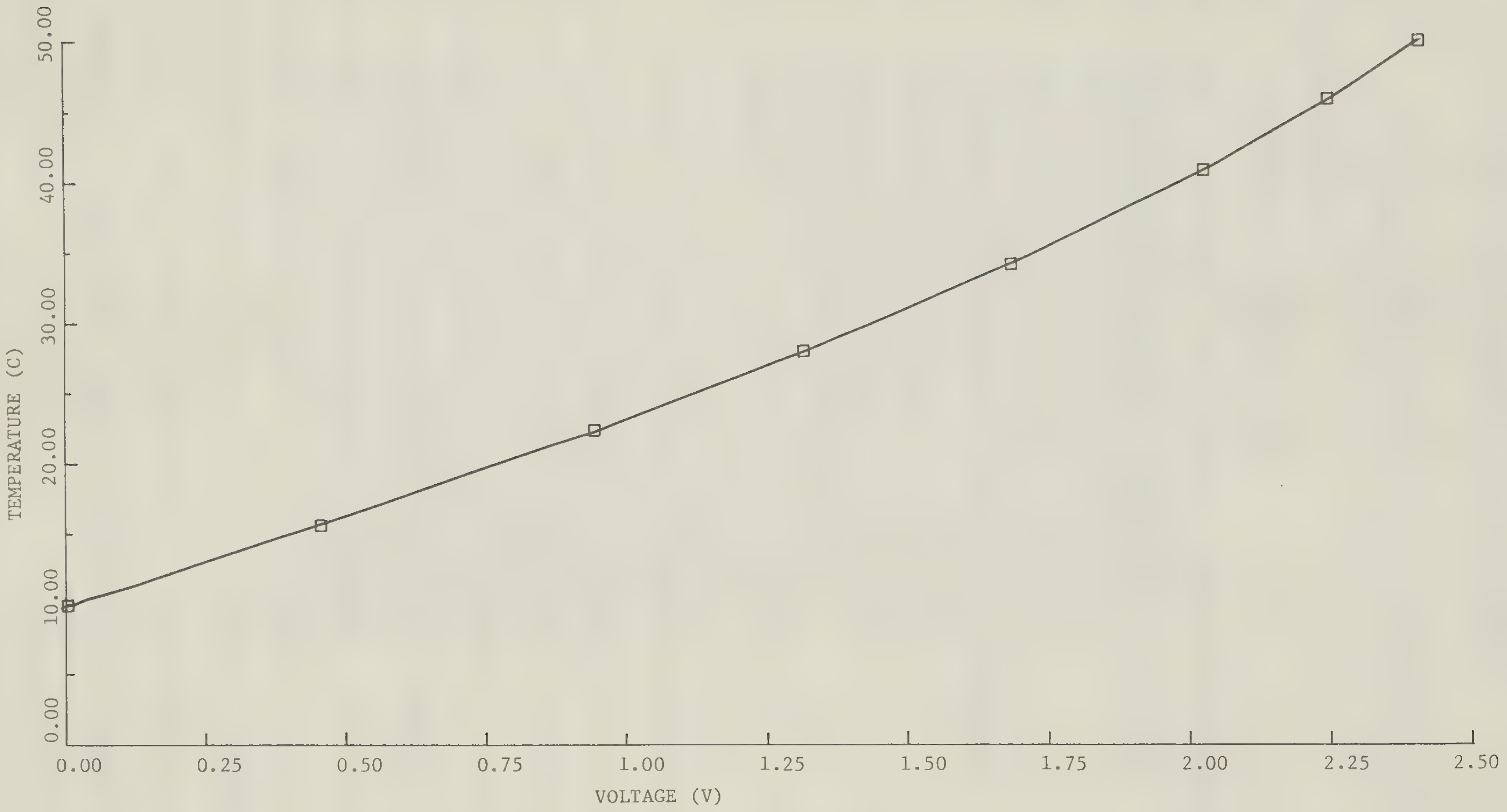

FIGURE 3.6 TYPICAL CALIBRATION CURVE FOR THERMISTOR PROBES

3.3.4 Data Acquisition System

The Data Acquisition System consisted of the following elements:

(1) Co-ordinate positioner

(2) 8000 A Digital Multimeter (John Fluke MFG. Co)

(3) 100 channel scanner - Digitec model 635
(United Systems Corporation)

(4) Scan counter

(5) HP-3480 B Integrating Digital Voltmeter

(6) HP-3482 A D.C. Range unit

(7) Model 623 Punch Controller
(United Systems Corporation)

(8) Papertape punch (Franklin electronics, inc.)

Figure 3.8 shows a general view of the system. Each thermistor was assigned to a specified channel scanner in addition to the X, Y and Z co-ordinates. Change in temperature would result in the change of the resistance of the thermistor probes and eventually change the voltages which were fed into the channel scanner. The scanner then routed the analogue signals to a converter where the signals were digitized and converted to binary coded decimal (BCD) form. The punch controller received the BCD signals and converted them into ASC11 code before routing it to the papertape punch. The papertape was read by the 1145 FEBD processor tape reader where the ASC11 code was automatically

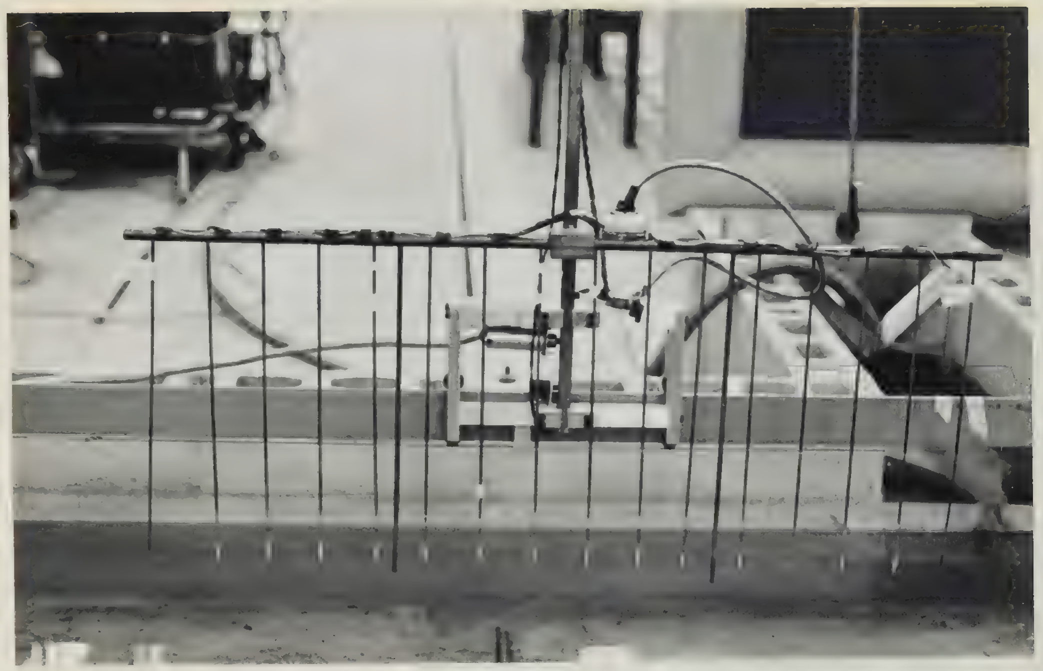

Figure 3.7 Thermistor Probes

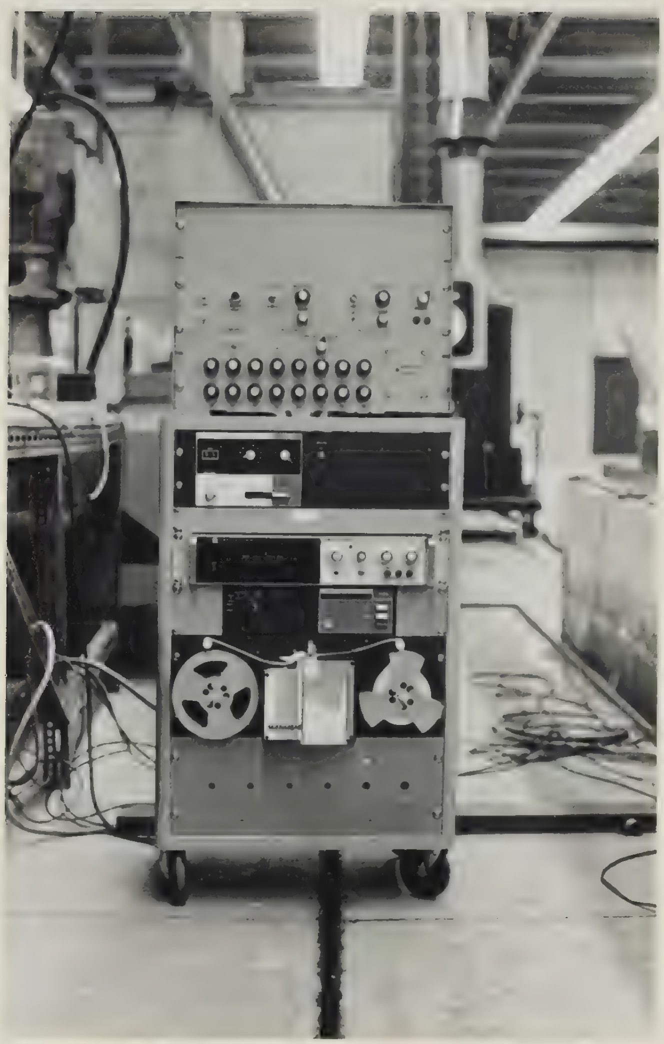

Figure 3.8 Data Acquisition System

translated to EBCDIC code, the code used by the IBM 360 computer, and stored in the computer files. A prewritten program was then used to calculate the temperature from the input file and printed out along with their average value. Figure 3.9 is a flow chart of the Data Acquisition and processing systems.

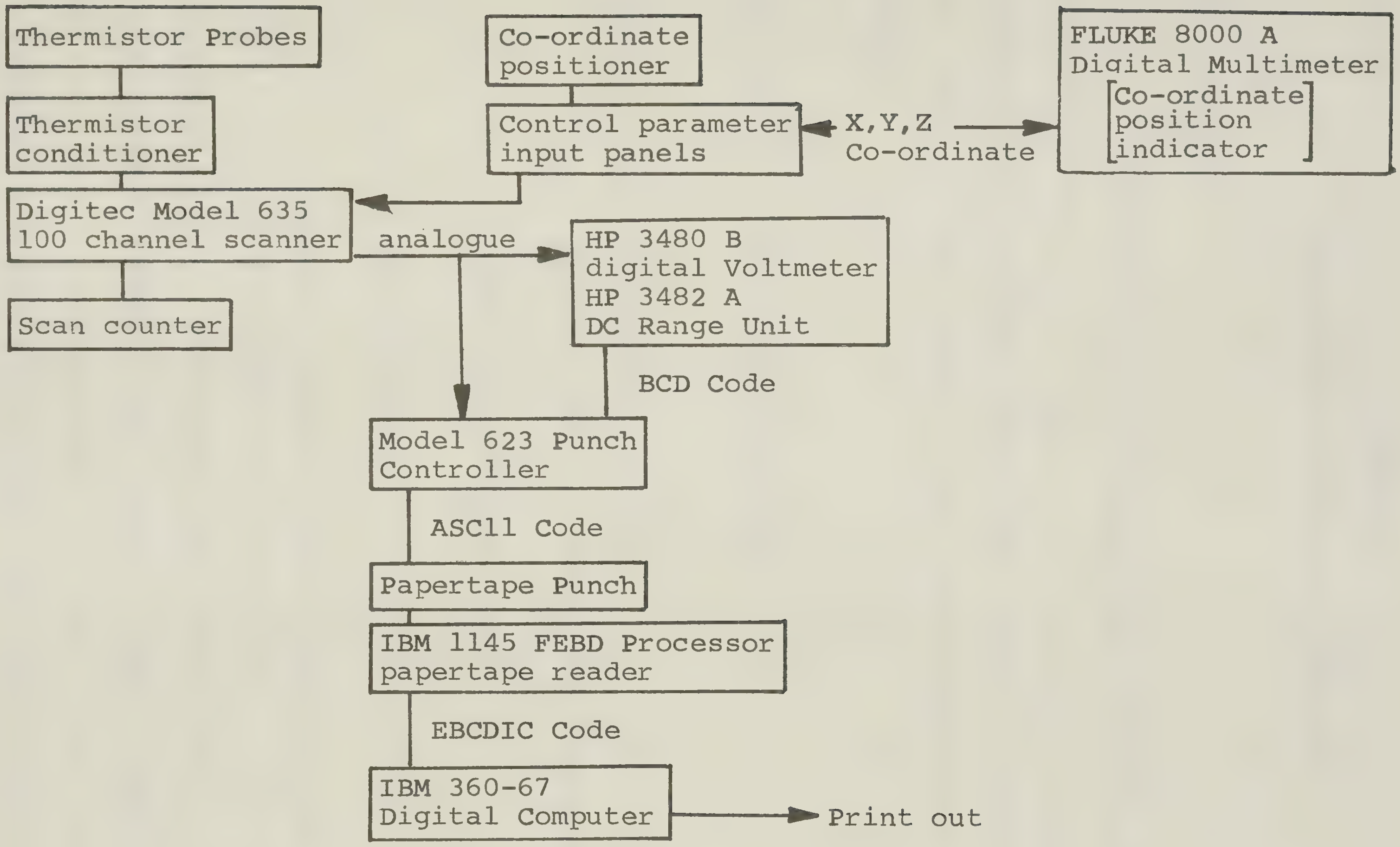
Thermistor Probes
Thermistor conditioner
Digitec Model 635 100 channel scanner
Scan counter
Co-ordinate positioner
Control parameter input panels
X,Y,Z Co-ordinate
FLUKE 8000 A Digital Multimeter [Co-ordinate position indicator]
analogue
HP 3480 B digital Voltmeter HP 3482 A DC Range Unit
BCD Code
Model 623 Punch Controller
ASC11 Code
Papertape Punch
IBM 1145 FEBD Processor papertape reader
EBCDIC Code
IBM 360-67 Digital Computer
Print out

Figure 3.9 Data Acquisition and Processing Systems

CHAPTER 4

EXPERIMENTAL RESULTS AND ANALYSIS

4.1 General

In this study, six experiments with Richardson numbers of 0.035, 0.1, 0.29, 0.56, 0.75 and 1.14 were carried out. The source Richardson number is defined as the inverse of the square of the source densimetric Froude number:

$$R_{io} = \frac{1}{(F_o)^2} = \frac{((\rho_a - \rho_o)/\rho_a)\, gh_o}{U_o^2}$$

where h_o jet depth at outfall

ρ_a water density at cross flow temperature

ρ_o water density at the outfall

U_o jet velocity

A previous study by Pande indicated that the behavior of surface discharge is governed strongly by the Richardson number. Though the exact values that divide the Richardson numbers into groups of large, moderate or small R_{io} are not well defined, 0.1 and 0.7 are believed to separate low Richardson number from the moderate, and

the moderate from the large Richardson numbers respectively. The rate of expansion of the surface discharge in any one Richardson number group is very different from that in any other group. Pande found that the rates of spreading and decay of excess temperature for surface discharges without cross flow as follows:

a. Small Richardson number

$$U_m \propto \frac{1}{x} \qquad T_m \propto \frac{1}{x} \qquad b \propto x \qquad h \propto x$$

b. large Richardson number (assuming $h \propto x^0$)

$$U_m \propto \frac{1}{x^{1/3}} \qquad T_m \propto \frac{1}{x^{2/3}} \qquad b \propto x$$

c. moderate Richardson number (assuming $h \propto x^C$)

$$C = 0 \qquad U_m \propto \frac{1}{x^{2/3}} \qquad T_m \propto \frac{1}{x^{2/3}} \qquad b \propto x^{4/3} \qquad h \propto x^0$$

$$C = 1 \qquad U_m \propto \frac{1}{x^{5/3}} \qquad T_m \propto \frac{1}{x^{5/3}} \qquad b \propto x^{7/3} \qquad h \propto x$$

where	U_m	centerline velocity
	ΔT_m	centerline excess temperature
	b	lateral distance from centerline where $\Delta T = \frac{1}{2} \Delta T_m$
	x	longitudinal distance measured from inlet
	h	distance measured downward from surface where $\Delta T = \frac{1}{2} \Delta T_s$

This study presents an investigation on the effect of cross-current on the surface jet behavior. The Reynold number was varied from 2840 to 14100 and the surface discharges were turbulent in nature. The details of initial conditions for all experiments are given in table 4.1.

4.2 Temperature Field

The temperature was measured by the thermistor probes as described in chapter 3. Experiments with Richardson numbers of 0.75, 0.1, 0.035 were run using the inlet 2.8' away from the side wall. The inlet had a b_o/h_o ratio of 1.19. In these three runs, the measurements started at a distance 0.5' from the inlet and the subsequent sections were 0.5 feet apart from each other. Other experiments with Richardson numbers of 0.29, 0.58, 1.14 were run using the centrally located inlet which had a b_o/h_o ratio of 1.13. The subsequent cross-sections were spaced 0.25 feet apart. In each experiment, a preliminary analysis on the surface temperature distribution was carried out to determine the jet axis, and then the temperature profiles on the vertical plane along the axis were measured at an interval of one foot. The reliability of the temperature readings was checked by calibrating the thermistor probes after the experiments and the agreement

EXPERIMENT	1	2	3	4	5	6
Richardson number	0.75	0.10	0.035	0.29	1.14	0.56
Reynold's number	5539	9234	14100	6300	2840	4554
Temperature difference (°C)	22.80	15.00	12.60	15.30	14.00	16.00
Inlet temperature (°C)	39.30	31.00	30.00	32.60	31.00	32.60
Crossflow temperature (°C)	16.50	16.00	17.40	17.30	17.00	16.60
Velocity ratio (U_o/U_1)	2.388	3.798	6.894	16.194	7.533	11.667
Inlet velocity (fps)	0.191	0.376	0.586	0.243	0.113	0.175
Crossflow velocity (fps)	0.080	0.099	0.085	0.015	0.015	0.015
Inlet discharge (cfs)	0.0045	0.0088	0.0136	0.0060	0.0028	0.0043
Inlet width (ft)	0.167	0.167	0.167	0.167	0.167	0.167
Inlet depth (ft)	0.140	0.140	0.140	0.148	0.148	0.148
Inlet area (sq. ft)	0.0233	0.0233	0.0233	0.0247	0.0247	0.0247

TABLE 4.1 EXPERIMENTAL DETAILS

was found within 0.2 degree centigrade of the initial readings.

4.3 Cross-flow Velocity Profiles

The velocity structure of the cross-flow (Figure 4.1, 4.2) was measured by Mr. Brent Berry using the Hydrogen-Bubble technique. Because the velocity was not uniformly distributed in all regions, average value was used when relating the parameters within that particular region.

4.4 Excess Temperature Profiles

The excess temperature ($\Delta T = T - T_a$) profiles measured on the surface yield a jet-like behavior with maximum excess temperature at the axis of the jet and decreasing towards the edges. The profiles also indicate clearly that the excess temperature profiles are not symmetrical about its axis due to the pressure and shear drags created by the cross-current. A typical set of cross-section profiles is shown in Figure 4.3 for $R_{io} = 0.035$. The excess temperature profiles for cross-sections perpendicular to the jet axis for the same Richardson number are shown in Figure 4.4. Measurements along the axis in the vertical plane show the maximum excess temperature is at the surface and ΔT decreases towards the bottom. These

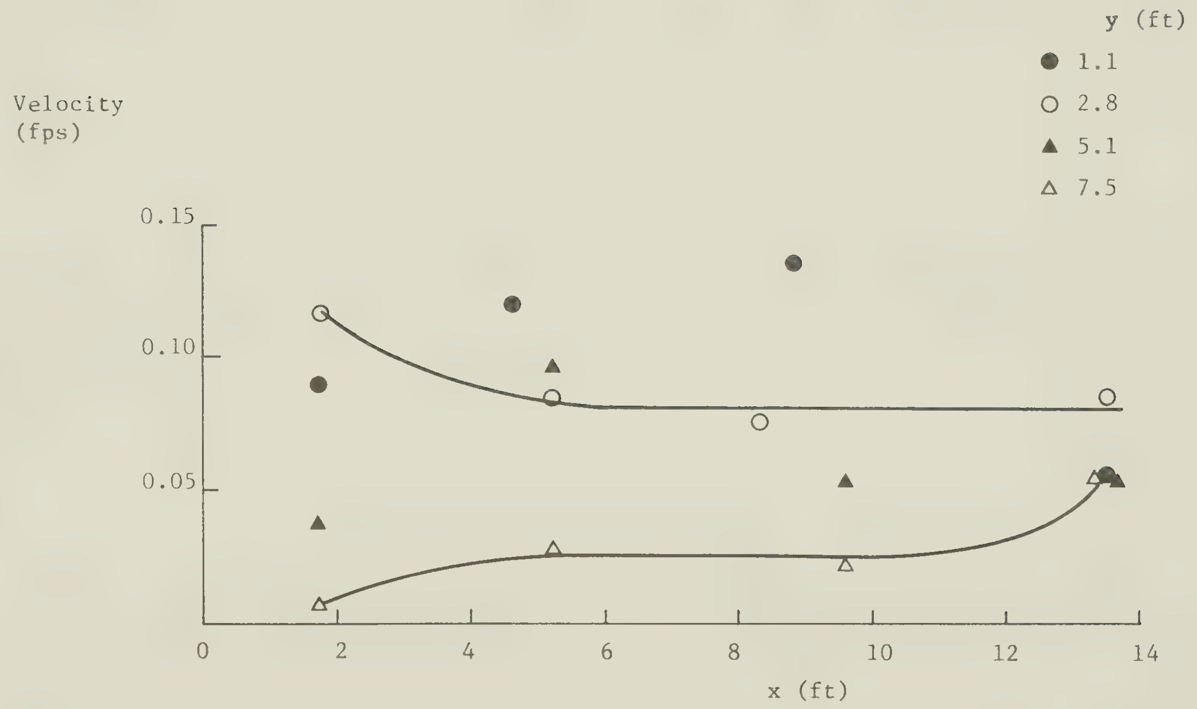

FIGURE 4.1 SURFACE VELOCITY STRUCTURE OF THE AMBIENT CURRENT

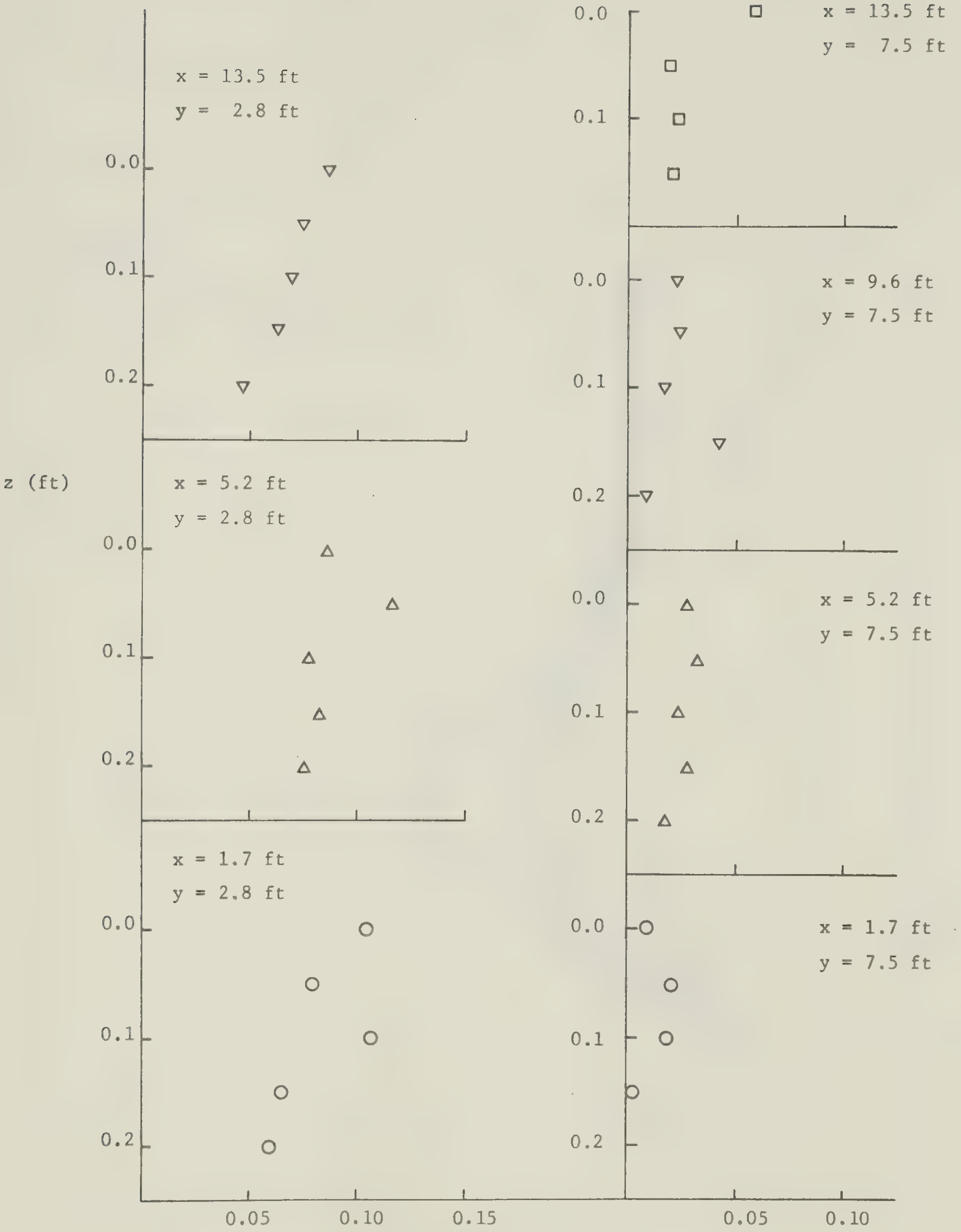

VELOCITY (fps)

FIGURE 4.2 FLOW STRUCTURE OF THE AMBIENT CURRENT

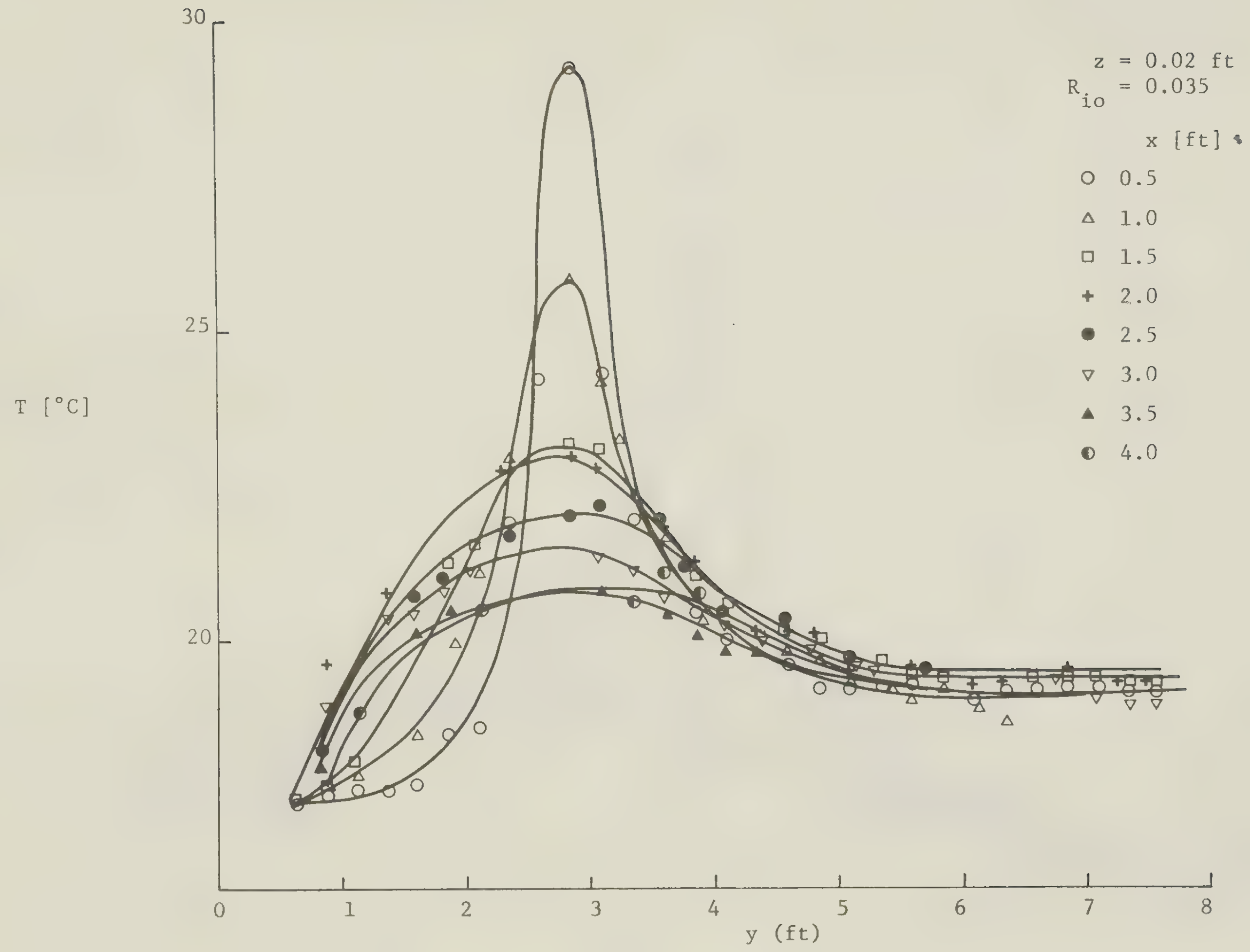

FIGURE 4.3 MEASURED TEMPERATURE DISTRIBUTION ON SURFACE FOR R_{io} = 0.035

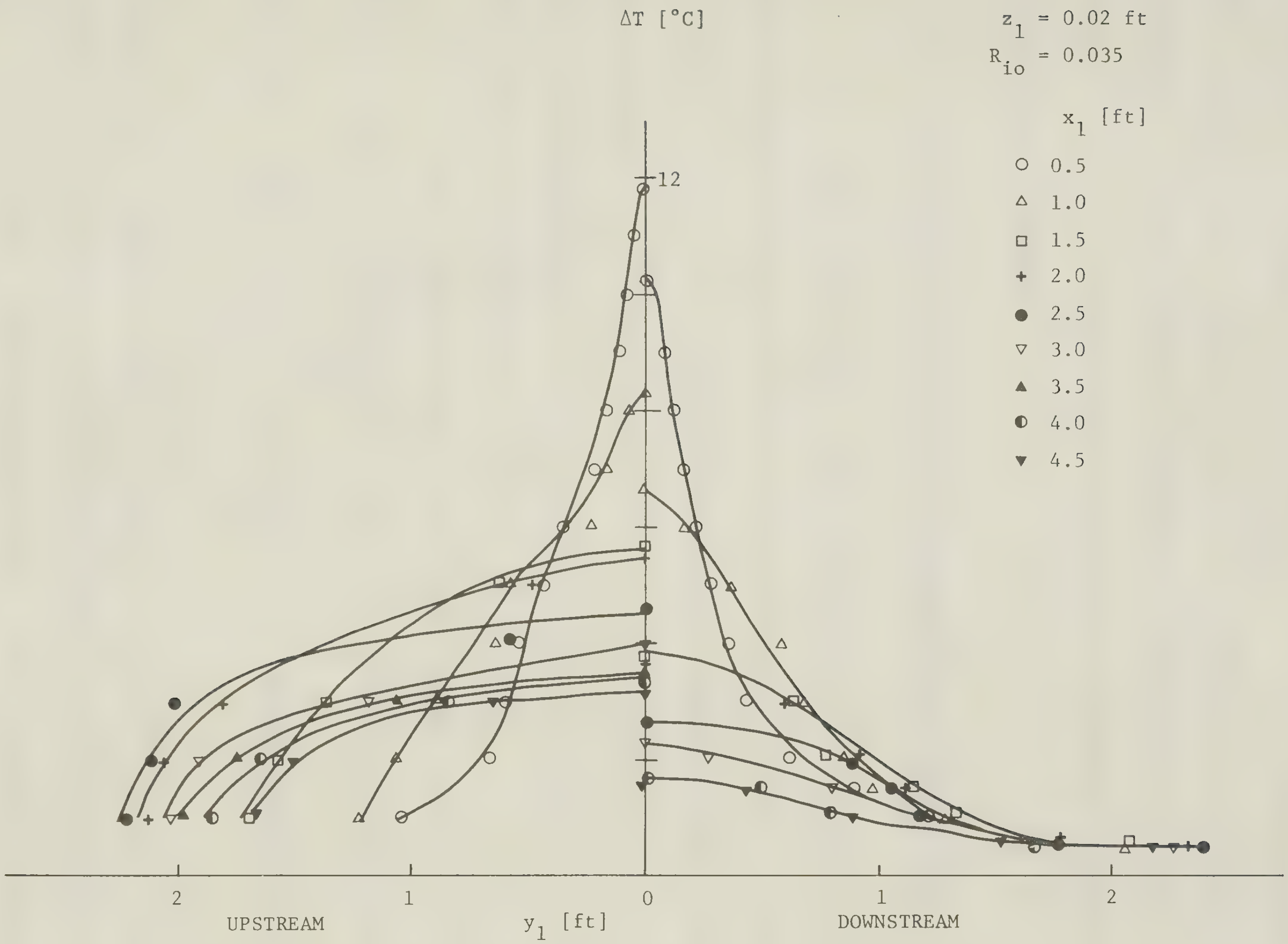

FIGURE 4.4 EXCESS TEMPERATURE PROFILES ON SURFACE ALONG JET AXIS FOR R_{io} = 0.035

profiles for all cross-sections are similar along the jet axis. Typical set of vertical excess temperature profiles is shown in Figure 4.5 for $R_{io} \doteq 0.75$. The presence of the cross flow does not seem to affect the shape of the profiles. The excess temperature profiles in the vertical direction of all runs show the same pattern regardless the Richardson number.

4.5 Similarity of Surface Temperature Profiles

For all runs, the temperature excess profiles were checked for similarity by plotting $(T - T_a)/(T_m - T_a)$ versus y_1/b_T for the upstream and downstream sides separately. The profiles have been found to be similar and described by the Gaussian Curve. A typical profile is shown in Figure 4.6 for $R_{io} = 1.14$.

The exponential (or Gaussian) curve $\frac{\Delta T}{\Delta T_m} = \exp\left(-0.693\left(\frac{y_1}{b_T}\right)^2\right)$, and the Schlichting-type distribution $\frac{\Delta T}{\Delta T_m} = \left(1 + 0.41\left(\frac{y_1}{b_T}\right)^2\right)^{-2}$ are plotted on the same figure for comparision. Both the exponential curve and Schlichting-type distribution agree well with the data up to $\eta = 1.0$; but the exponential curve gives values slightly below those obtained from measurements after $\eta = 1.0$. It seems the best fit to the data is the Schlichting-type

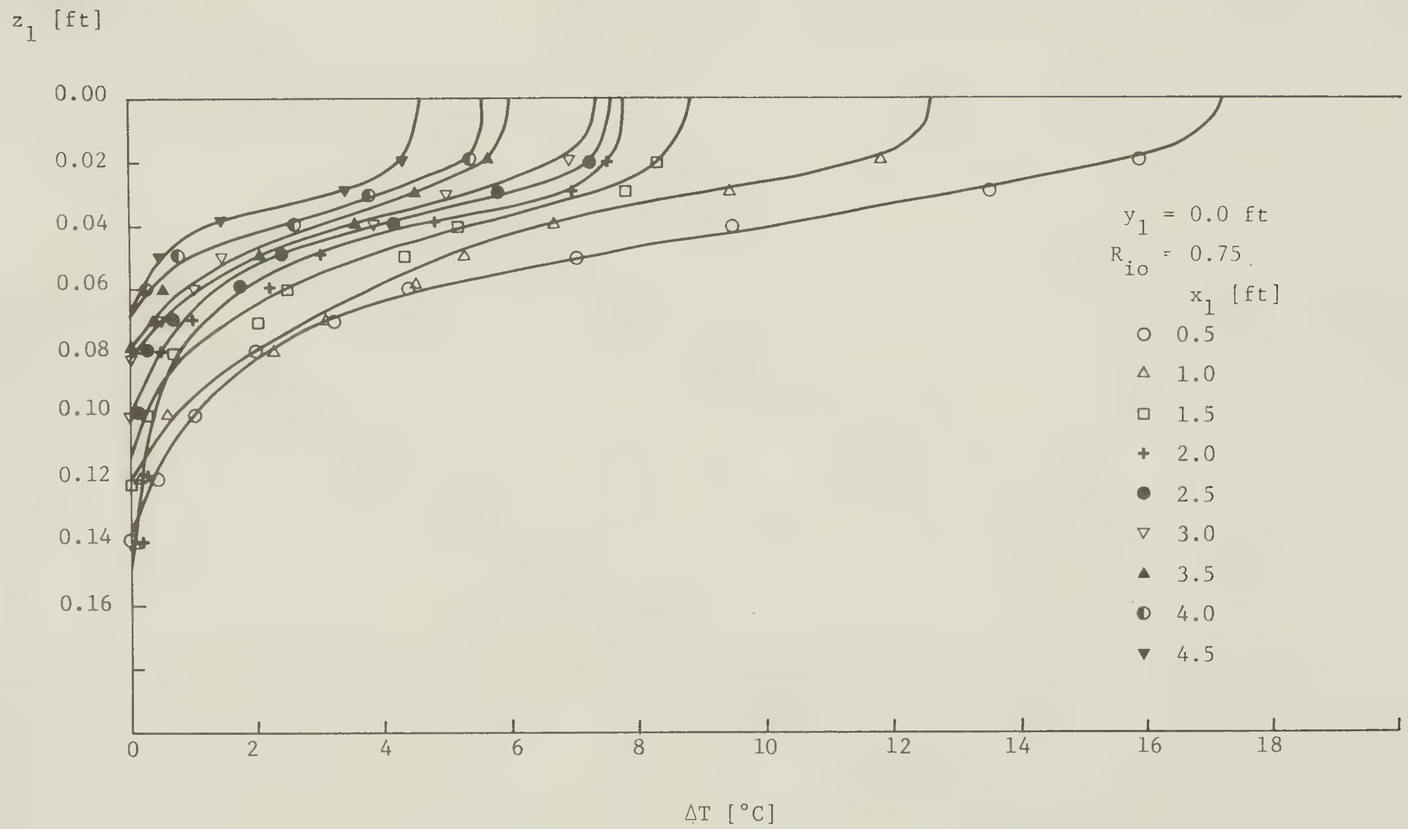

FIGURE 4.5 EXCESS TEMPERATURE PROFILES ON THE VERTICAL PLANE ALONG THE JET AXIS FOR R_{io} = 0.75

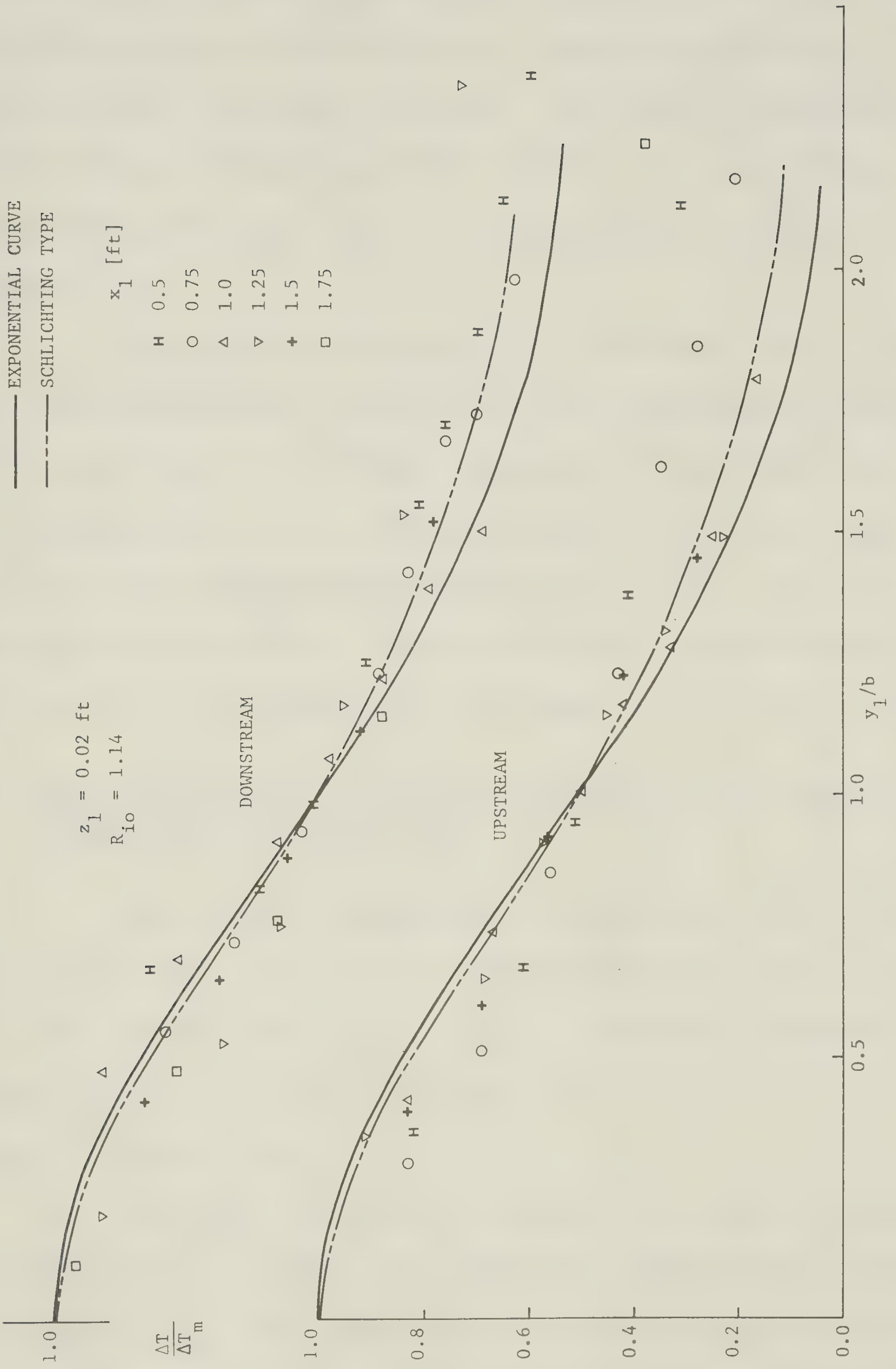

FIGURE 4.6 NON-DIMENSIONAL TEMPERATURE PROFILE ON SURFACE FOR R_{io} = 1.14

distribution but the exponential curve has the advantage of being simple to work with in integral operations. The existence of the cross flow does not affect the similarity of the excess temperature distribution on the surface. The similarity plots for other runs are given in Figure 4.7 to Figure 4.11.

Though the assumption of similarity still held for each experiment, the shape of the similarity profiles on the upstream is affected strongly by the cross flow, the exponential curve being obviously a very poor approximation in the chosed neighbourhood of $\eta \simeq 1.0$. The downstream profiles are not affected by the cross-current at all and can be treated as in the case of zero cross flow.

4.6 Similarity of Temperature Profiles on the Vertical Plane along Axis of Jet

The excess temperature profiles on the vertical plane were also found to be similar for all sections along the axis of the jet for all runs. A typical non-dimensional plot of $\Delta T/\Delta T_m$ versus Z_1/h for $R_{io} = 0.035$ is shown in Figure 4.12

The Schlichting type distribution fits the data best for $Z_1/h < 1.0$ but lies above all experimental data for $Z_1/h > 1.0$. The exponential curve describes the data reasonably well. In the case of no cross-current, Pande

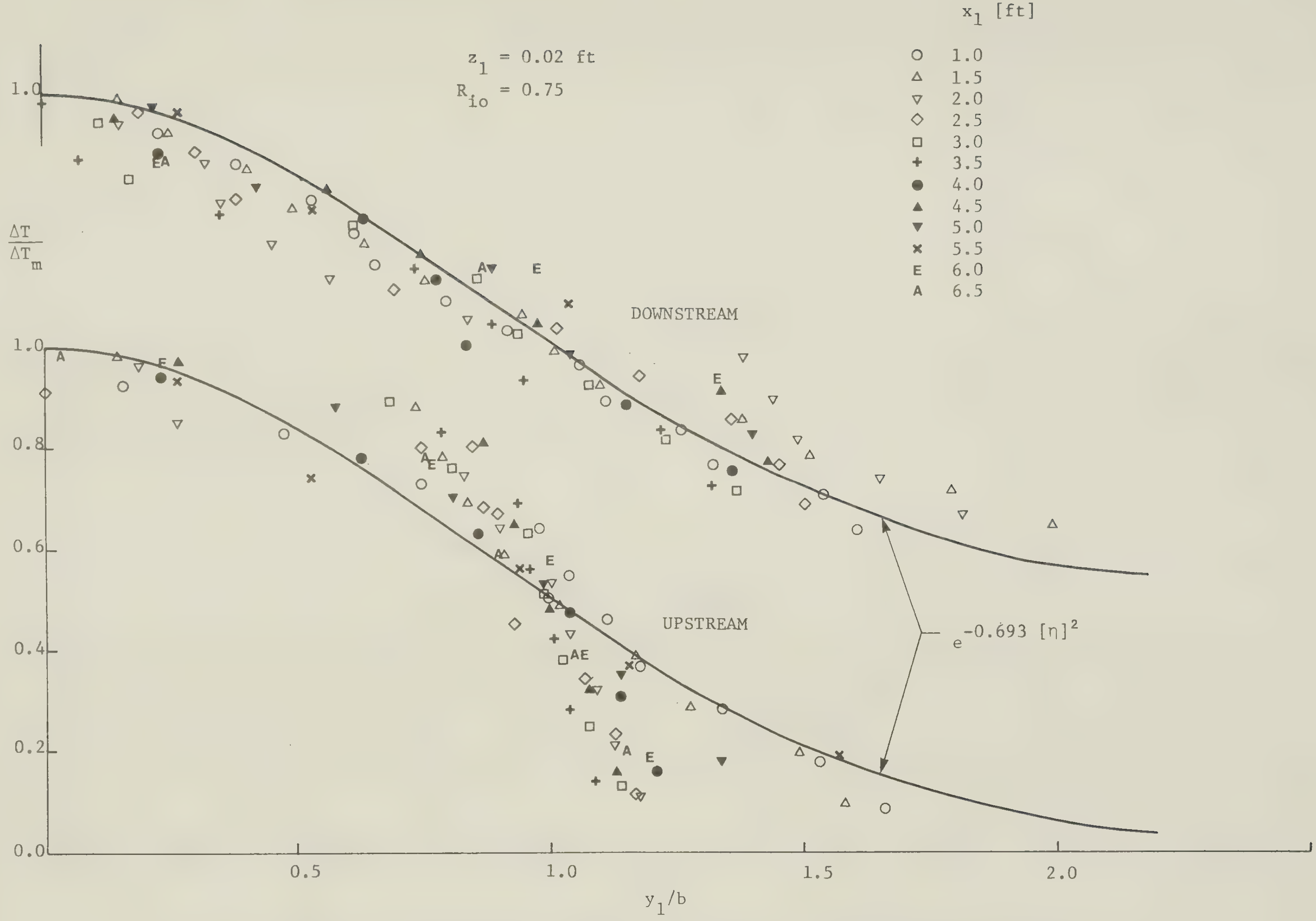

FIGURE 4.7 NON-DIMENSIONAL TEMPERATURE PROFILE ON SURFACE FOR R_{io} = 0.75

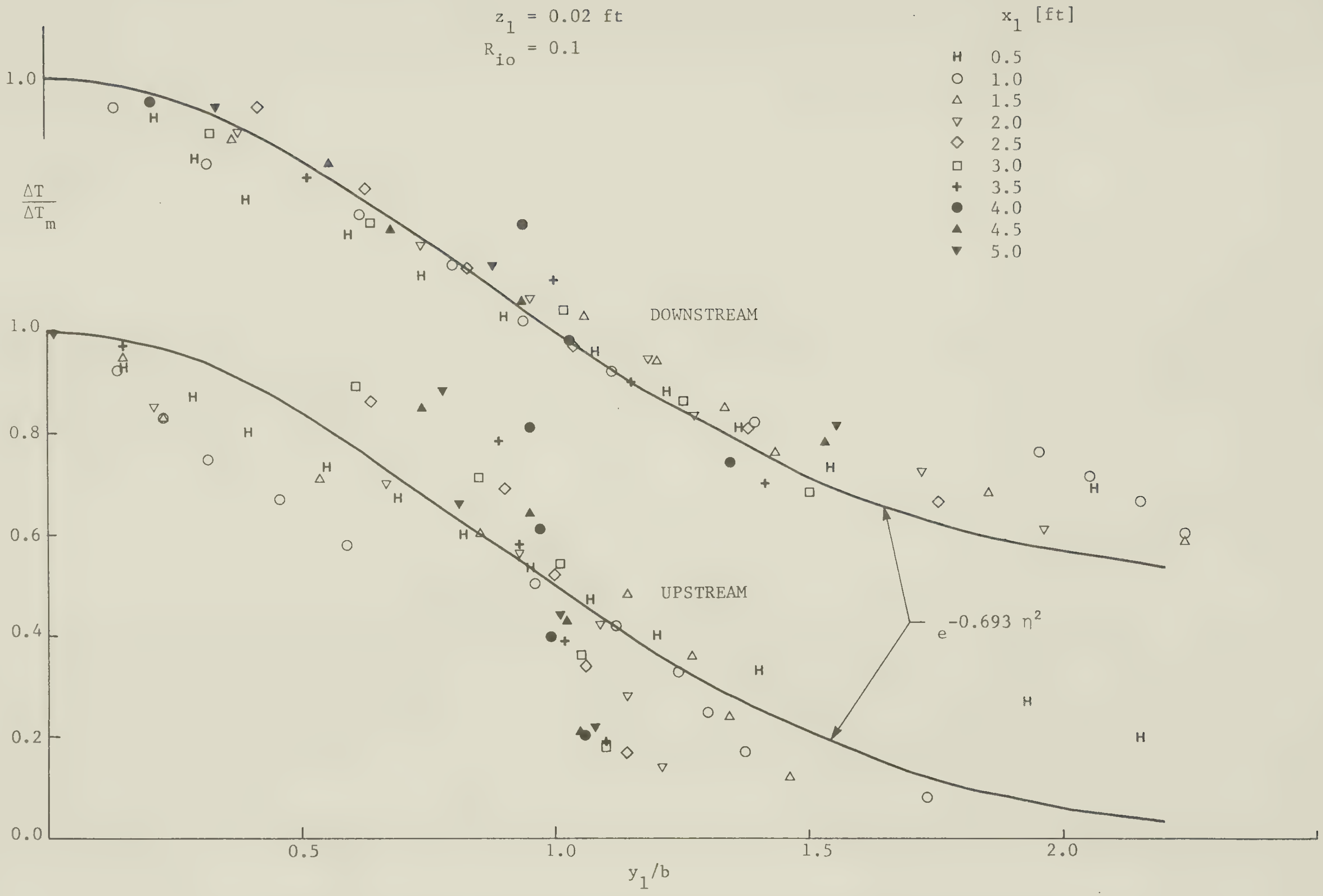

FIGURE 4.8 NON-DIMENSIONAL TEMPERATURE PROFILE ON SURFACE FOR $R_{io} = 0.1$

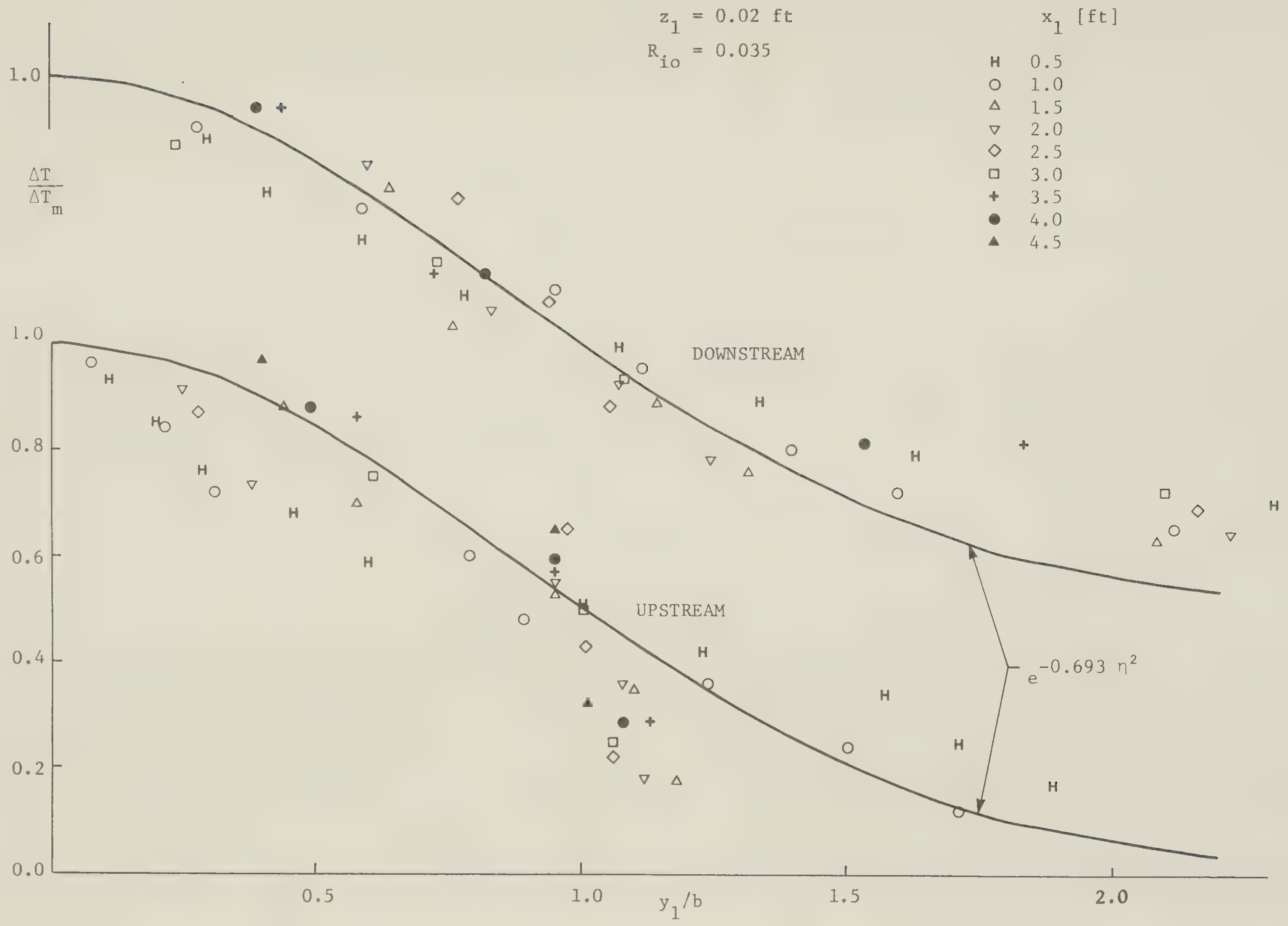

FIGURE 4.9 NON-DIMENSIONAL TEMPERATURE PROFILE ON SURFACE FOR R_{io} = 0.035

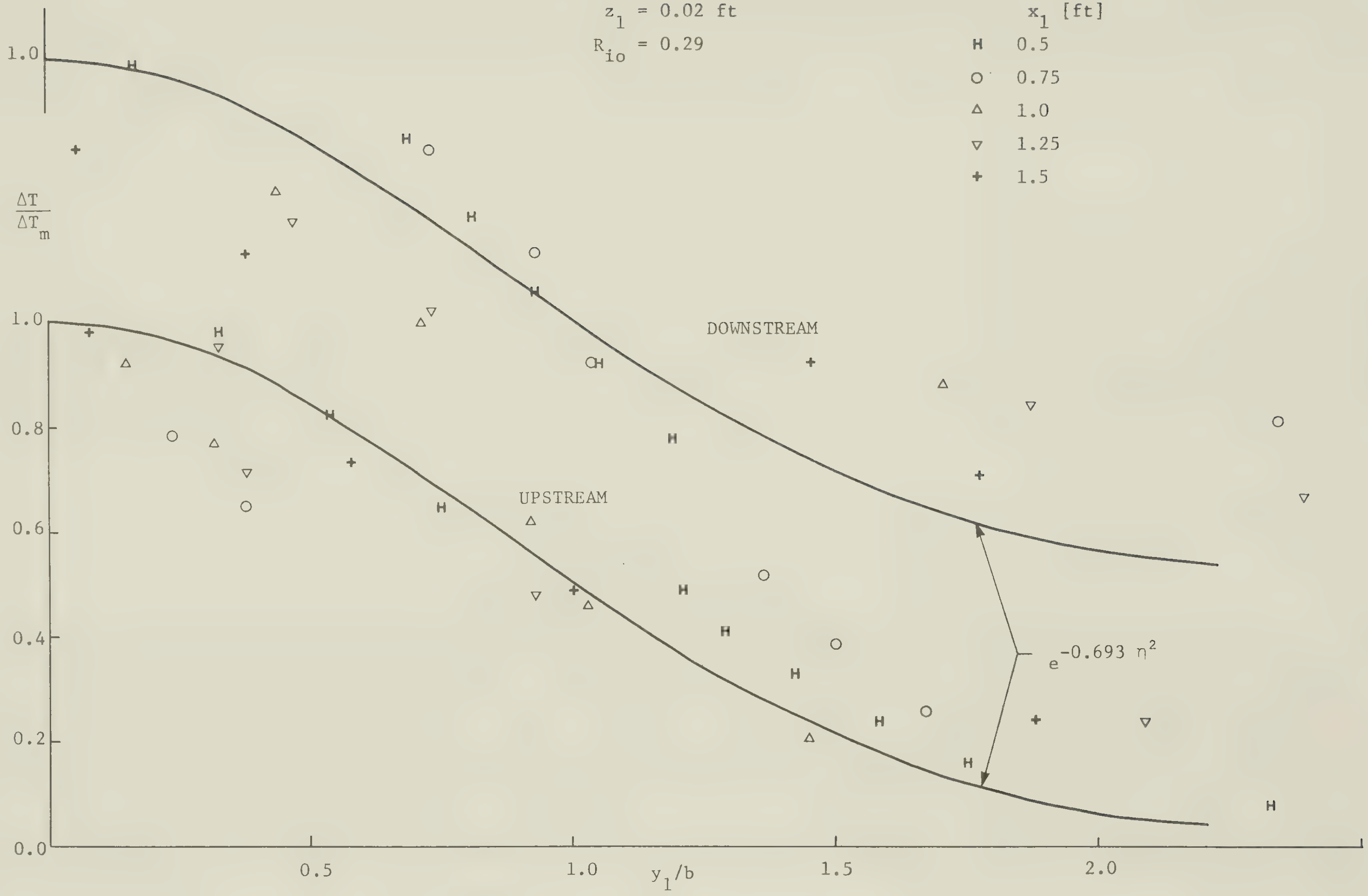

FIGURE 4.10 NON-DIMENSIONAL TEMPERATURE PROFILE ON SURFACE FOR R_{io} = 0.29

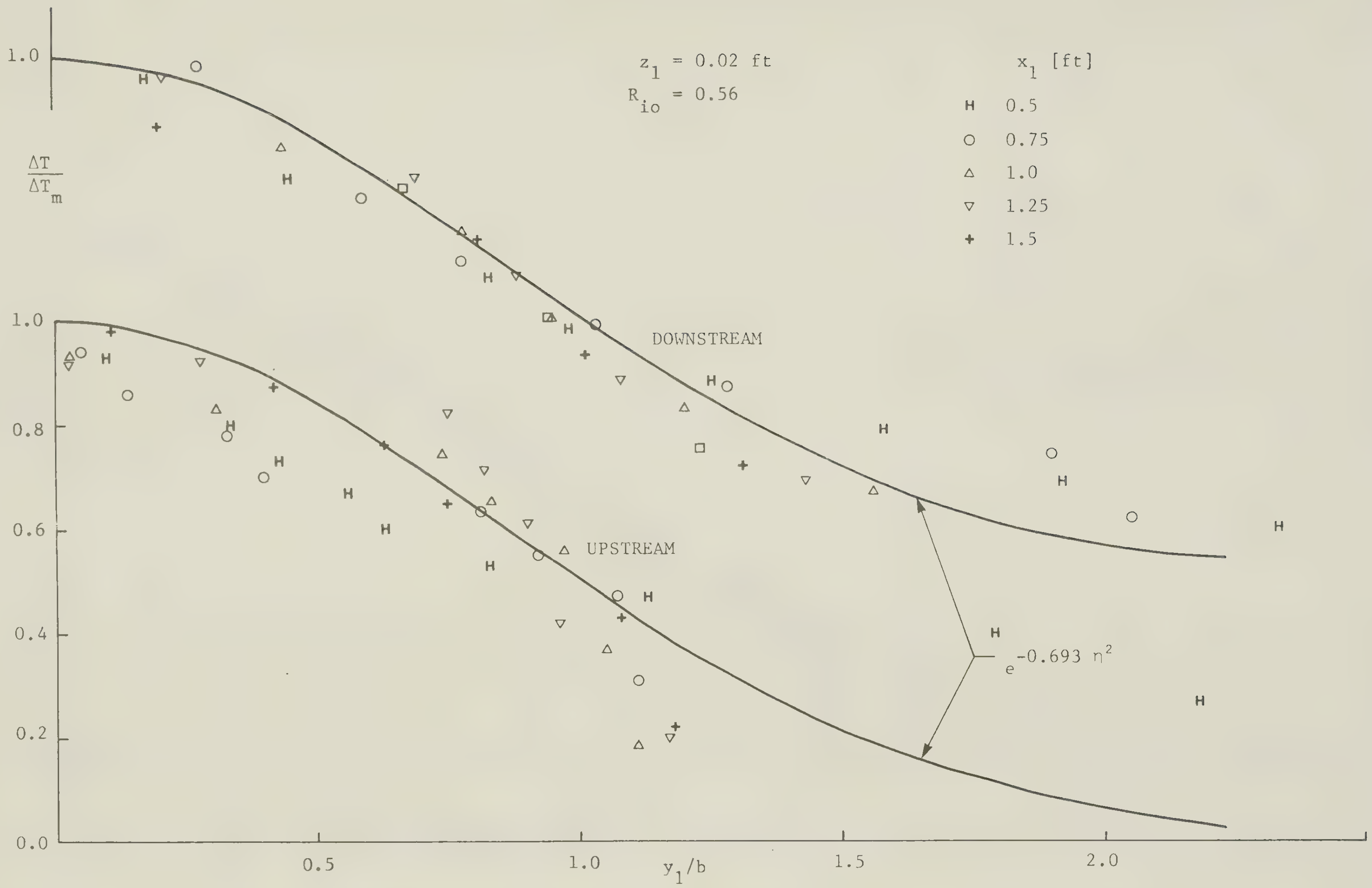

FIGURE 4.11 NON-DIMENSIONAL TEMPERATURE PROFILE ON SURFACE FOR $R_{io} = 0.56$

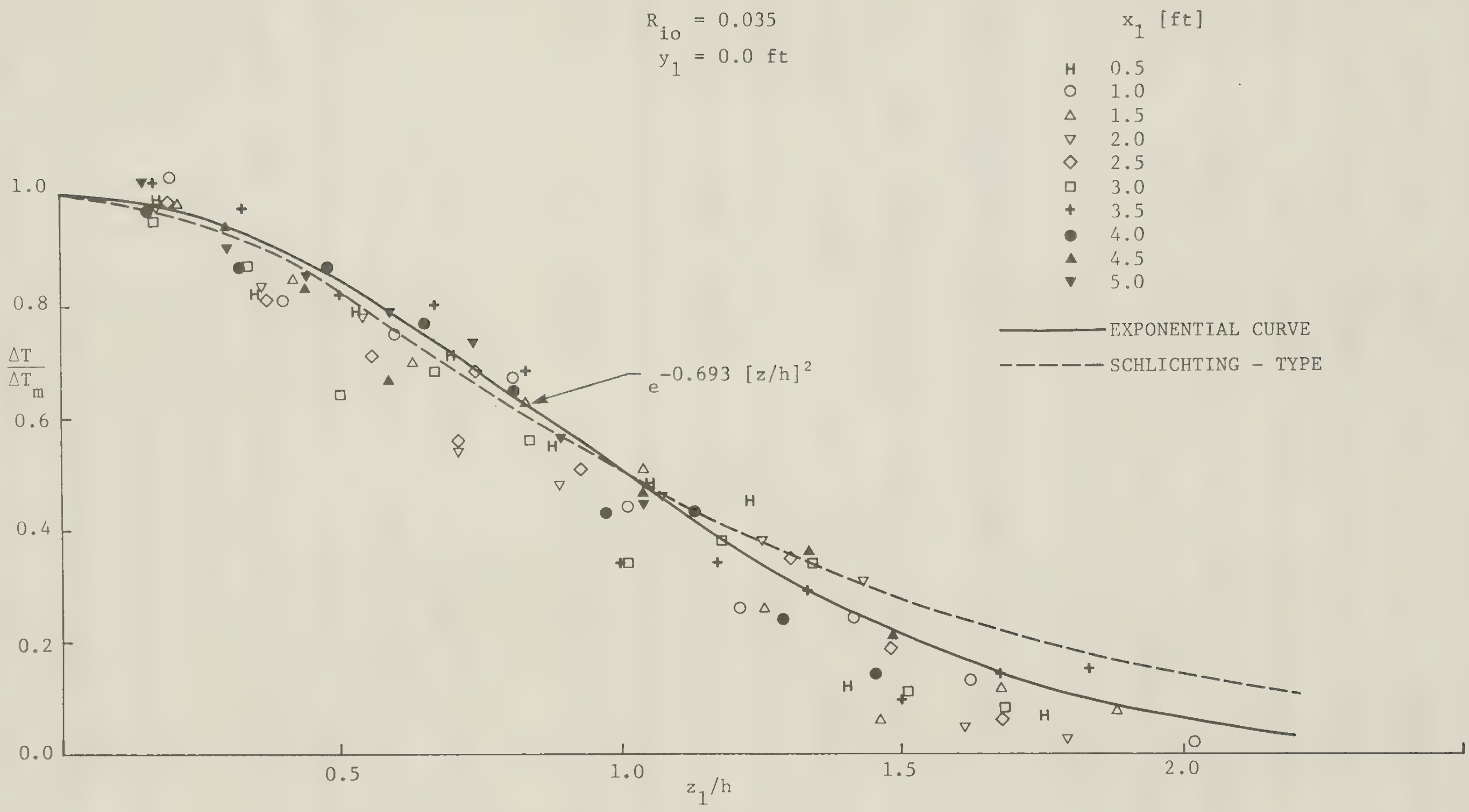

FIGURE 4.12 NON-DIMENSIONAL TEMPERATURE PROFILE ALONG THE JET AXIS FOR R_{io} = 0.035

found the Schlichting type distribution, which predicts higher values than the exponential curve towards the bottom, agrees well with his data. Comparison of these two cases indicates that the excess temperature decays much faster towards the bottom in cross flow than in the case of zero cross flow. The similarity plots for other Richardson number are given in Figure 4.13 and Figure 4.14.

4.7 Excess Temperature Decay along the Axis

The decay of the excess temperature for all runs is plotted in Figure 4.15 and 4.16. The decay of the excess temperature is not linear but decrease sharply at the beginning and then more gradually along the axis. The relatively distinct locations of the data indicate the influence of other factors such as Richardson number and aspect ratio.

A dimensionless plot of $\Delta T_{ma}/\Delta T_o$ against $x_1/\sqrt{A_o}$, where ΔT_{ma} is the average of the upstream and downstream excess temperature, is shown in Figure 4.17. The length scale has been chosen as $\sqrt{A_o}$ following the work of Pani (1972) on bluff wall jets.

In Figure 4.17, the data obviously can be divided into two groups with one located above the other. The upper group contains the data obtained by using the side inlet and has a smaller velocity ratio. The lower group

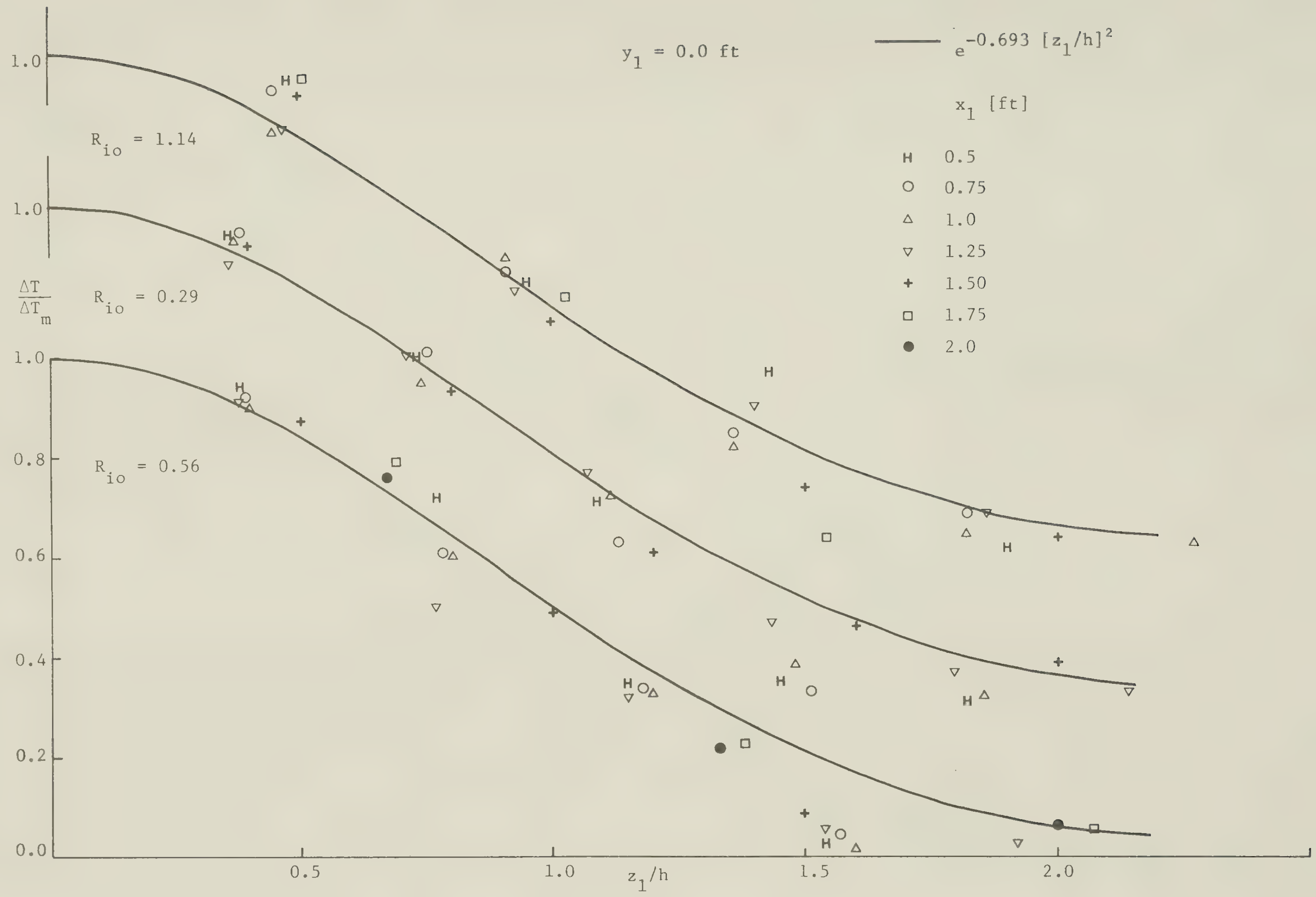

FIGURE 4.13 NON-DIMENSIONAL TEMPERATURE PROFILE ALONG THE JET AXIS

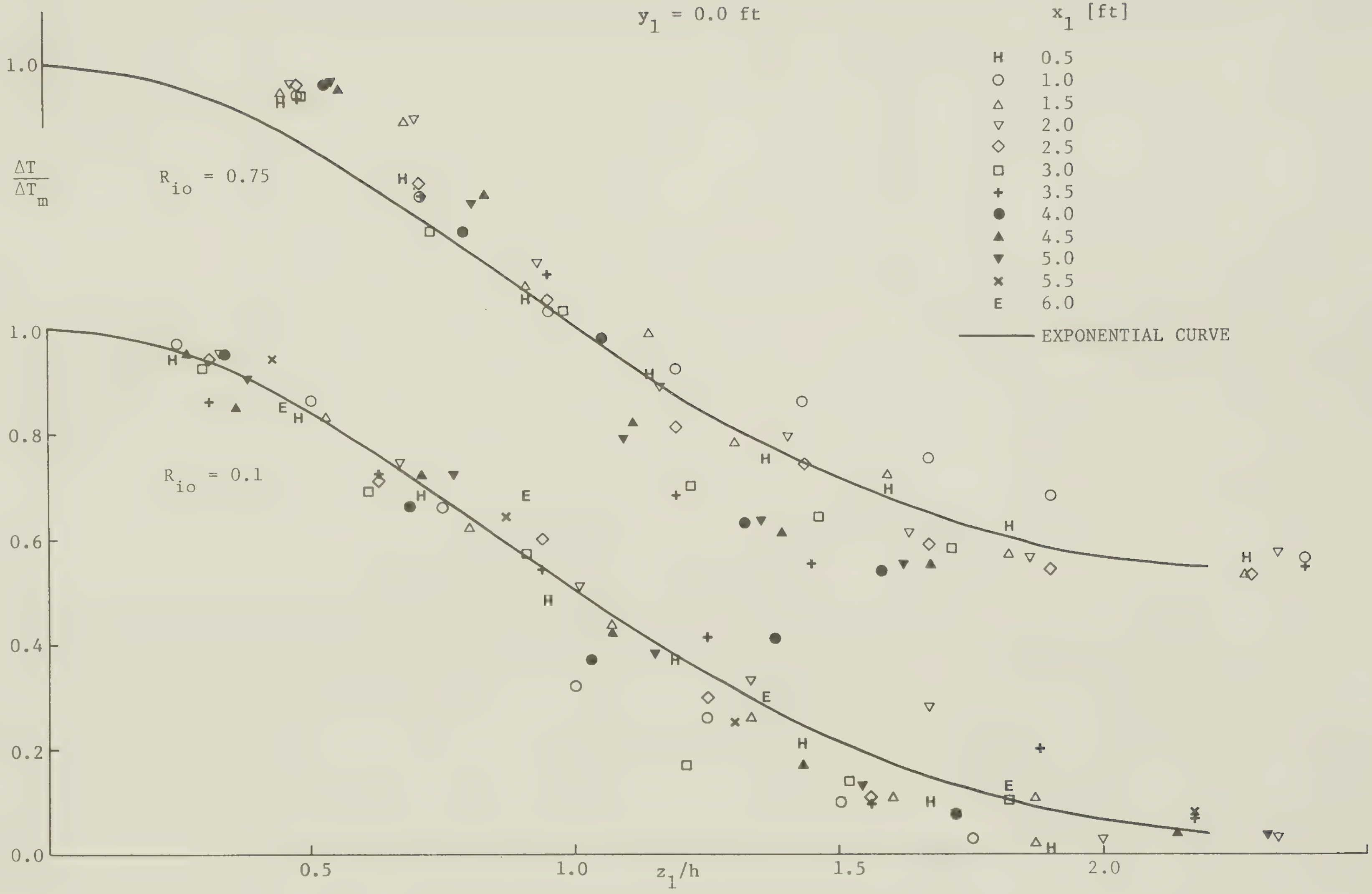

FIGURE 4.14 NON-DIMENSIONAL TEMPERATURE PROFILES ALONG THE JET AXIS

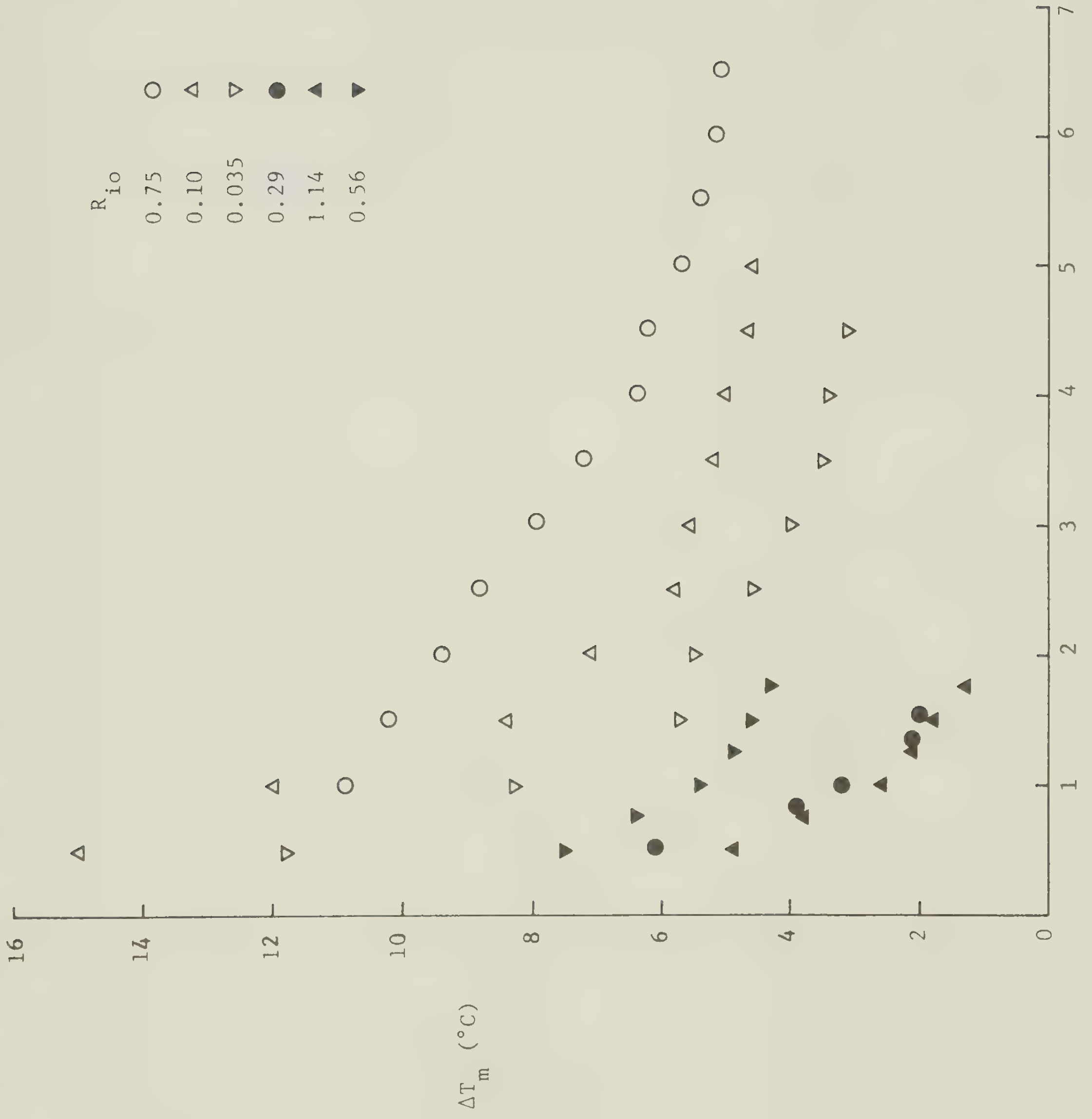

FIGURE 4.15 UPSTREAM EXCESS TEMPERATURE DECAY ALONG JET AXIS ON SURFACE

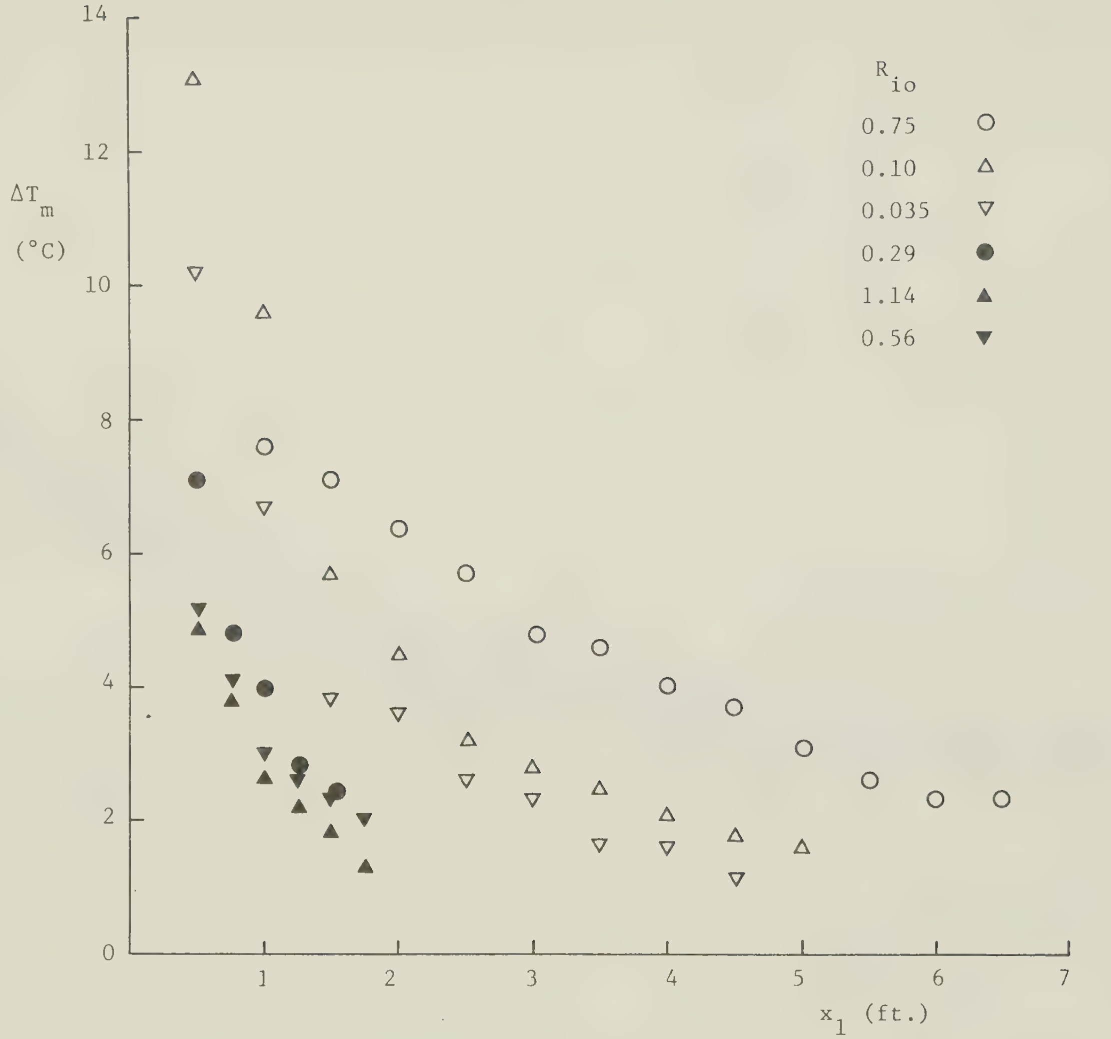

FIGURE 4.16 DOWNSTREAM EXCESS TEMPERATURE DECAY ALONG JET AXIS ON SURFACE

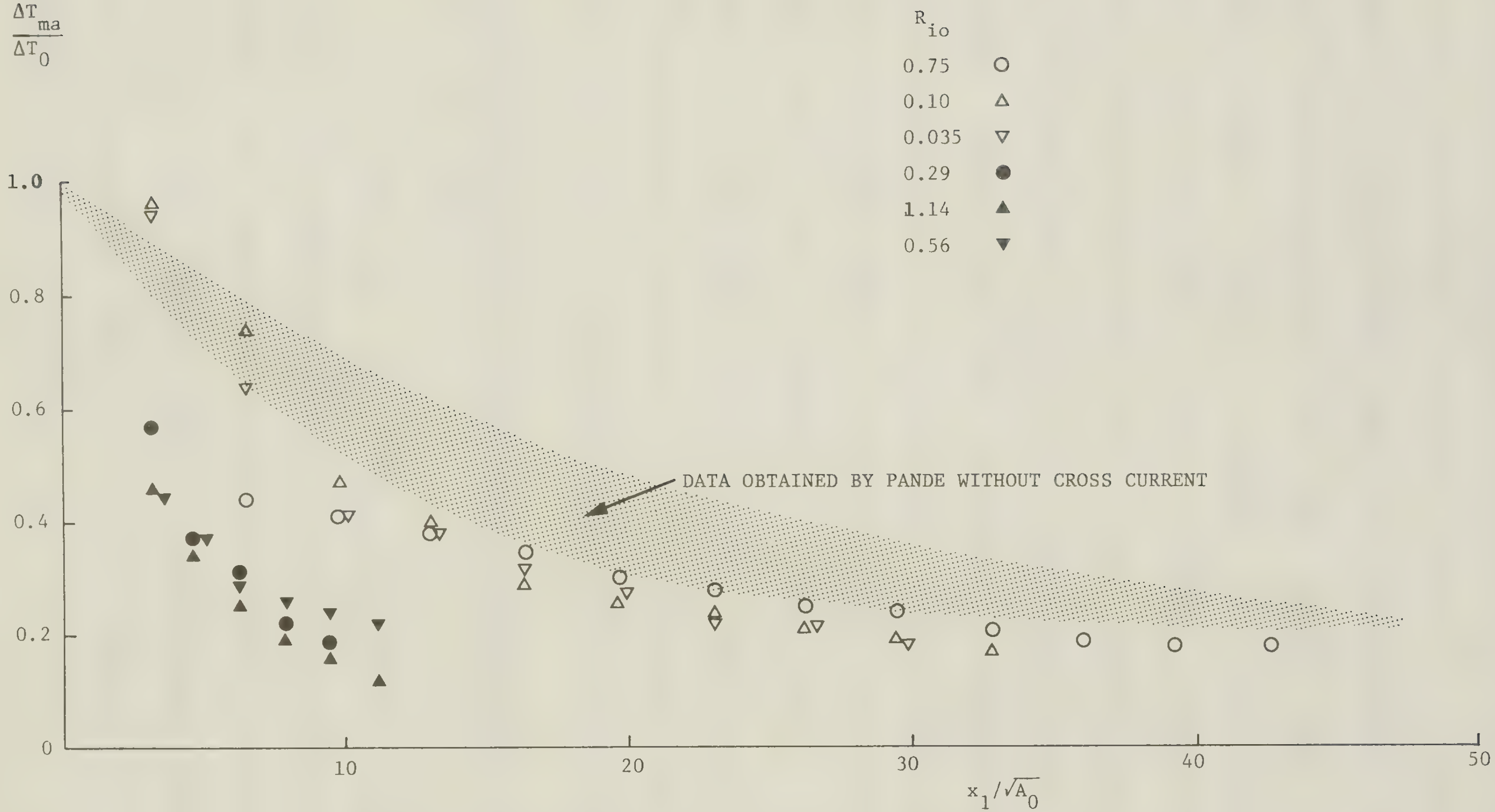

FIGURE 4.17 NON-DIMENSIONAL PLOT OF TEMPERATURE DECAY ON SURFACE

of data points are collected using the centrally located inlet and a much higher velocity ratio. It is difficult to explain the phenomenon that the measurements with a stronger cross-current do not decay faster than those with a weaker current. Also, it appears not very logical that the data with stronger current is closer to the data obtained by Pande without cross flow. Though Carter's laboratory experiments have shown that the center line temperature decay has a form apparently independent of the velocity ratio, we believe that the increasing amount of entrained fluid due to a stronger current should increase the dilution. Figure 4.17 also shows that all the data lie below the data of Pande. The faster decay rate is due to the existence of the cross-current which increases the rate of entrainment and dilution considerably.

4.8 Correlation of the Temperature Coefficient with the Velocity Ratio

For each run, $\Delta T_o / \Delta T_{ma}$ is plotted against $x_1 / \sqrt{A_o}$ and the equation that fits the data best is determined. The equation assumes that ΔT_{ma} is a function of ΔT_o, x_1, $\sqrt{A_o}$ and R_{io}; and all the other variables are included in a coefficient C_t. C_t is then plotted against the velocity ratio $\alpha = U_o/U_1$.

Large Richardson Number

Previous study by Pande indicates that the excess temperature on the axis varies as the -2/3 power of the distance along the axis, and can be written as:

$$\frac{\Delta T_{ma}}{\Delta T_o} = C_t\,(R_{io})^{-1/3}\left(\frac{x_1}{\sqrt{A_o}} + C_2\right)^{-2/3}$$

Pande evaluated this equation using his experimental data and gave:

$$\frac{\Delta T_{ma}}{\Delta T_o} = 3.1664\,(R_{io})^{-1/3}\left(\frac{x_1}{\sqrt{A_o}} + 1.795\right)^{-2/3} \qquad (4.8.1)$$

The plots of $(\Delta T_o / \Delta T_{ma})^{3/2}$ versus $x_1 / \sqrt{A_o}$ for $R_{io} = 0.75$ and 1.14 are given in Figure 4.18. Table 4.2 A gives the summary of the calculations.

The best fit equations determined from the data are:

for $R_{io} = 0.75$

$$\frac{\Delta T_{ma}}{\Delta T_o} = 2.027\,(R_{io})^{-1/3}\left(\frac{x_1}{\sqrt{A_o}} + 1.2\right)^{-2/3} \qquad (4.8.2)$$

for $R_{io} = 1.14$

$$\frac{\Delta T_{ma}}{\Delta T_o} = 0.684\,(R_{io})^{-1/3}\left(\frac{x_1}{\sqrt{A_o}} - 1.75\right)^{-2/3} \qquad (4.8.3)$$

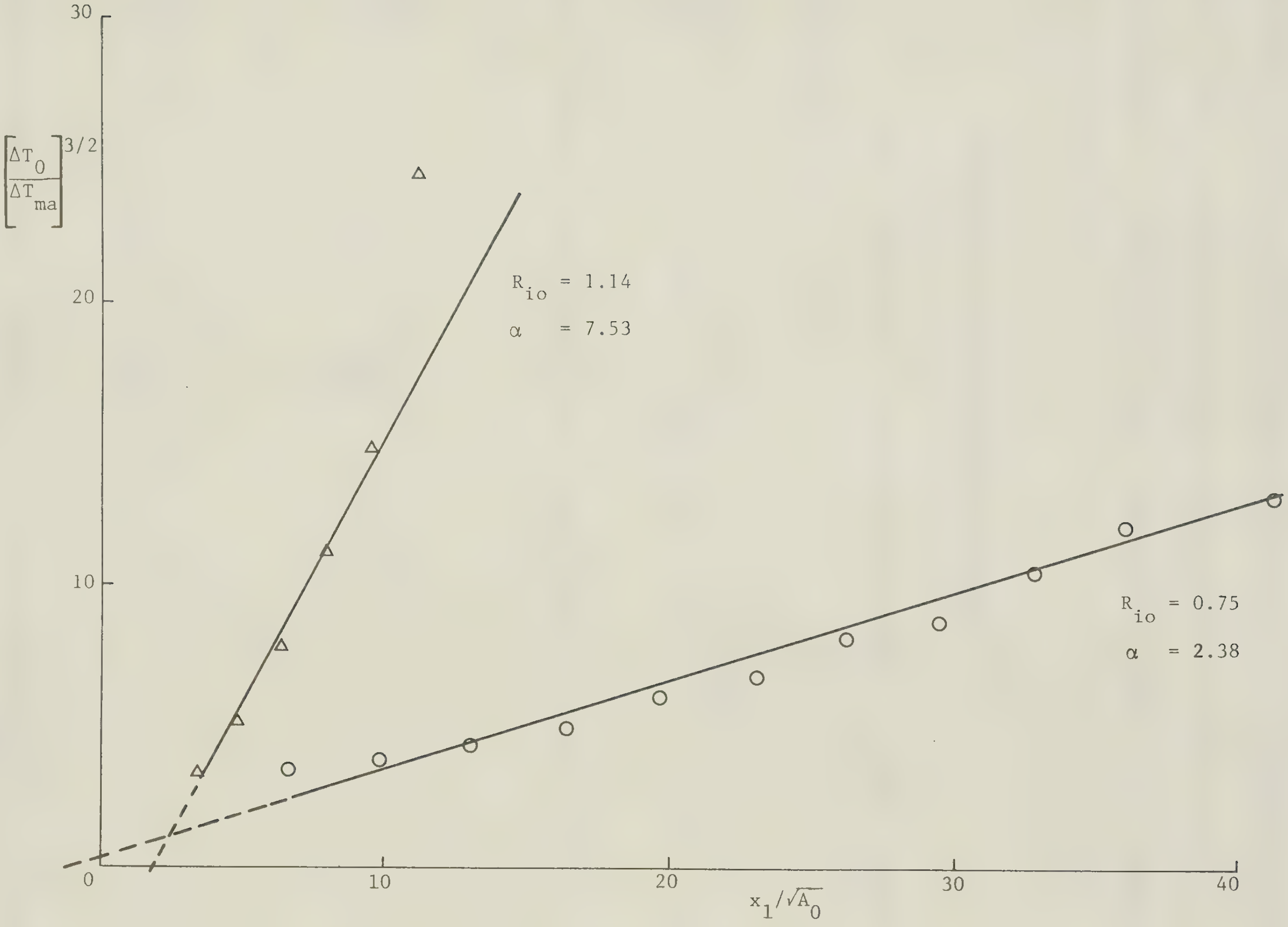

FIGURE 4.18 $[\Delta T_0/\Delta T_{ma}]^{3/2}$ VS. $x_1/\sqrt{A_0}$ FOR LARGE R_{io}

Figure 4.21 A is the plot of C_t against $1/\alpha$ for large Richardson numbers. Because of the limited data available, no equation can be written. It only shows the trend that C_t decreases to a minimum as the velocity ratio approaches an optimum value and after that, C_t increases with decreasing α .

Moderate Richardson Number

For moderate Richardson number, Pande found the equation:

$$\frac{\Delta T_{ma}}{\Delta T_o} = 4.42\ (R_{io})^{1/3} \left(\frac{x_1}{\sqrt{A_o}} + 1.795 \right)^{-2/3} \qquad (4.8.4)$$

In our study, the equations are found to be:

for $R_{io} = 0.29$

$$\frac{\Delta T_{ma}}{\Delta T_o} = 1.13\ (R_{io})^{1/3} \left(\frac{x_1}{\sqrt{A_o}} - 1.7 \right)^{-2/3} \qquad (4.8.5)$$

for $R_{io} = 0.56$

$$\frac{\Delta T_{ma}}{\Delta T_o} = 1.35\ (R_{io})^{1/3} \left(\frac{x_1}{\sqrt{A_o}} + 0.5 \right)^{-2/3} \qquad (4.8.6)$$

respectively. The summary of the calculation is given in Table 4.2 B and the plots of $(\Delta T_o/\Delta T_{ma})^{3/2}$ versus $x_1/\sqrt{A_o}$ for the two Richardson numbers are given in

Figure 4.19. From Figure 4.21 B, the temperature coefficient C_t shows the same trend as in the large Richardson number, but the optimum value for α is different.

Small Richardson Number

For small Richardson number, Tamai, Weigel and Tornberg give the equation

$$\frac{\Delta T_{ma}}{\Delta T_o} = 7.0 \left(\frac{x}{D_o} \right)^{-1} \qquad (4.8.7)$$

for temperature excess decay for a circular jet without cross flow. (D_o in Equation 4.8.7 is the diameter of jet outlet and x is the longitudinal distance). Our experiments yield the equations

for $R_{io} = 0.1$

$$\frac{\Delta T_{ma}}{\Delta T_o} = 5.89 \left(\frac{x_1}{\sqrt{A_o}} + 1.9 \right)^{-1} \qquad (4.8.8)$$

for $R_{io} = 0.035$

$$\frac{\Delta T_{ma}}{\Delta T_o} = 5.61 \left(\frac{x_1}{\sqrt{A_o}} + 1.9 \right)^{-1} \qquad (4.8.9)$$

It seems that in the small Richardson number group, the Richardson number has no effect on determining the temperature decay. The two equations determined from

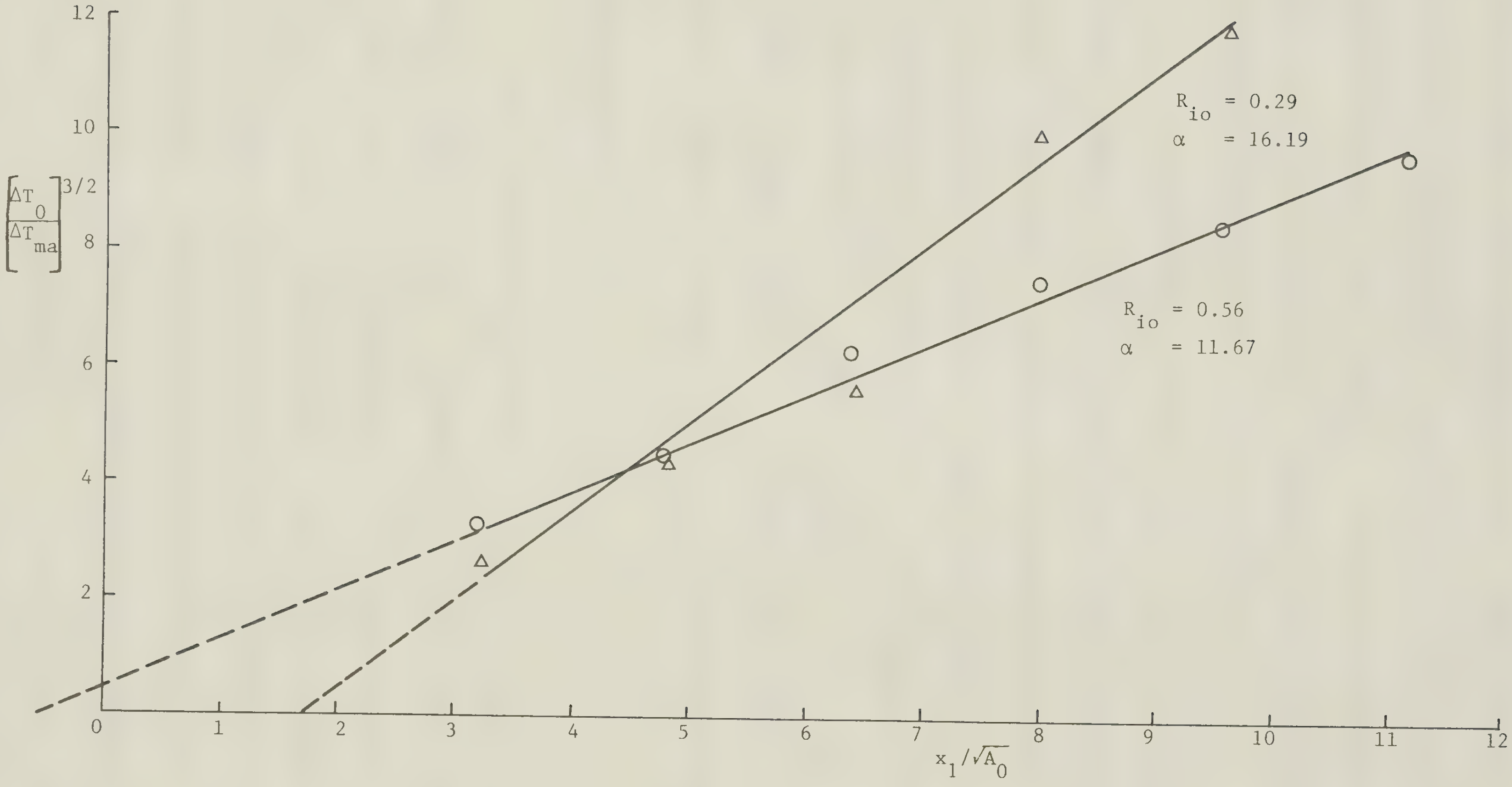

FIGURE 4.19 $[\Delta T_0/\Delta T_{ma}]^{3/2}$ VS. $x_1/\sqrt{A_0}$ FOR MODERATE R_{io}

our data differ only slightly from each other in the temperature coefficient. Table 4.2 C is the summary of the calculation. $\Delta T_o / \Delta T_{ma}$ is plotted against $x_1/\sqrt{A_o}$ in Figure 4.20 for $R_{io} = 0.1$ and 0.035 respectively, and C_t is plotted against $1/\alpha$ in Figure 4.21 C.

A comparison on the plots for different Richardson number groups shows that the temperature coefficients for small Richardson number are much greater than the other two groups. The data show the same trend as C_t decreases to a minimum for an optimum value α and then increases as α is decreasing. The rate of change of C_t with respect ot $1/\alpha$ is different for different Richardson number groups and so is the magnitude of C_t.

4.9 Isotherms

The surface isotherms for all experiments are plotted in Figure 4.22. Observation of the isotherms shows that for $R_{io} = 0.29$ and 0.75, the surface jets spread more on the downstream than on the upstream. This behavior is expected because of the additional pressure drag exerted on the upstream by the cross flow. For $R_{io} = 0.035$, the width on both sides are approximately equal; but for runs with $R_{io} = 1.14$, 0.1 and 0.56, we find that the jets spread more on the upstream than the

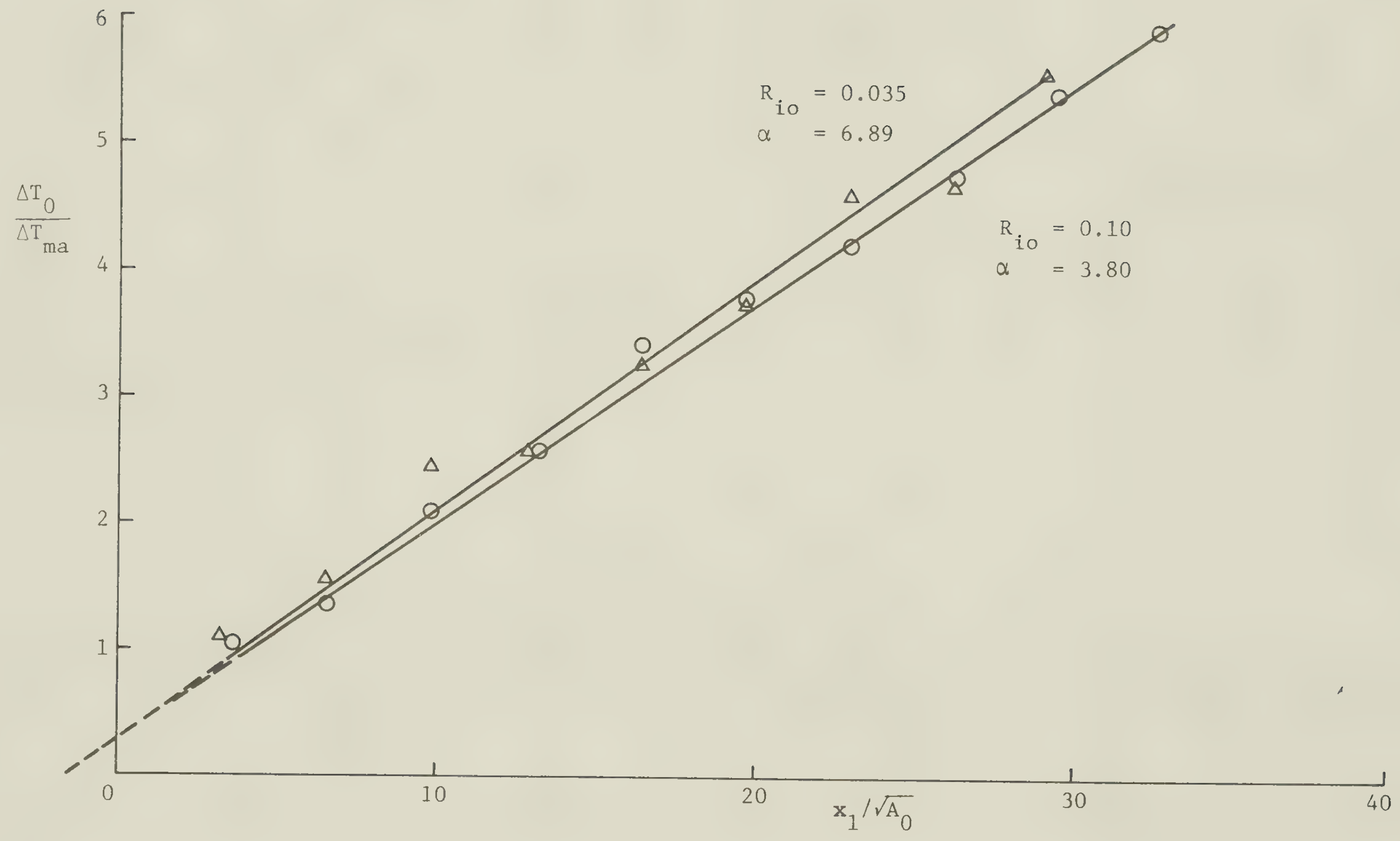

FIGURE 4.20 $[\Delta T_0/\Delta T_{ma}]$ VS. $x_1/\sqrt{A_0}$ FOR SMALL R_{io}

LARGE R_{io}

EXP NO	R_{io}	$1/\alpha$	C_t
PANDE		0	3.17
1	0.75	0.42	2.03
5	1.14	0.13	0.68

MODERATE R_{io}

EXP NO	R_{io}	$1/\alpha$	C_t
PANDE		0	4.42
4	0.29	0.06	1.13
6	0.56	0.09	1.35

SMALL R_{io}

EXP NO	R_{io}	$1/\alpha$	C_t
TAMAI, WEIGEL		0	7.0
2	0.10	0.26	5.89
3	0.035	0.15	5.61

Table 4.2 Values of Temperature Coefficient

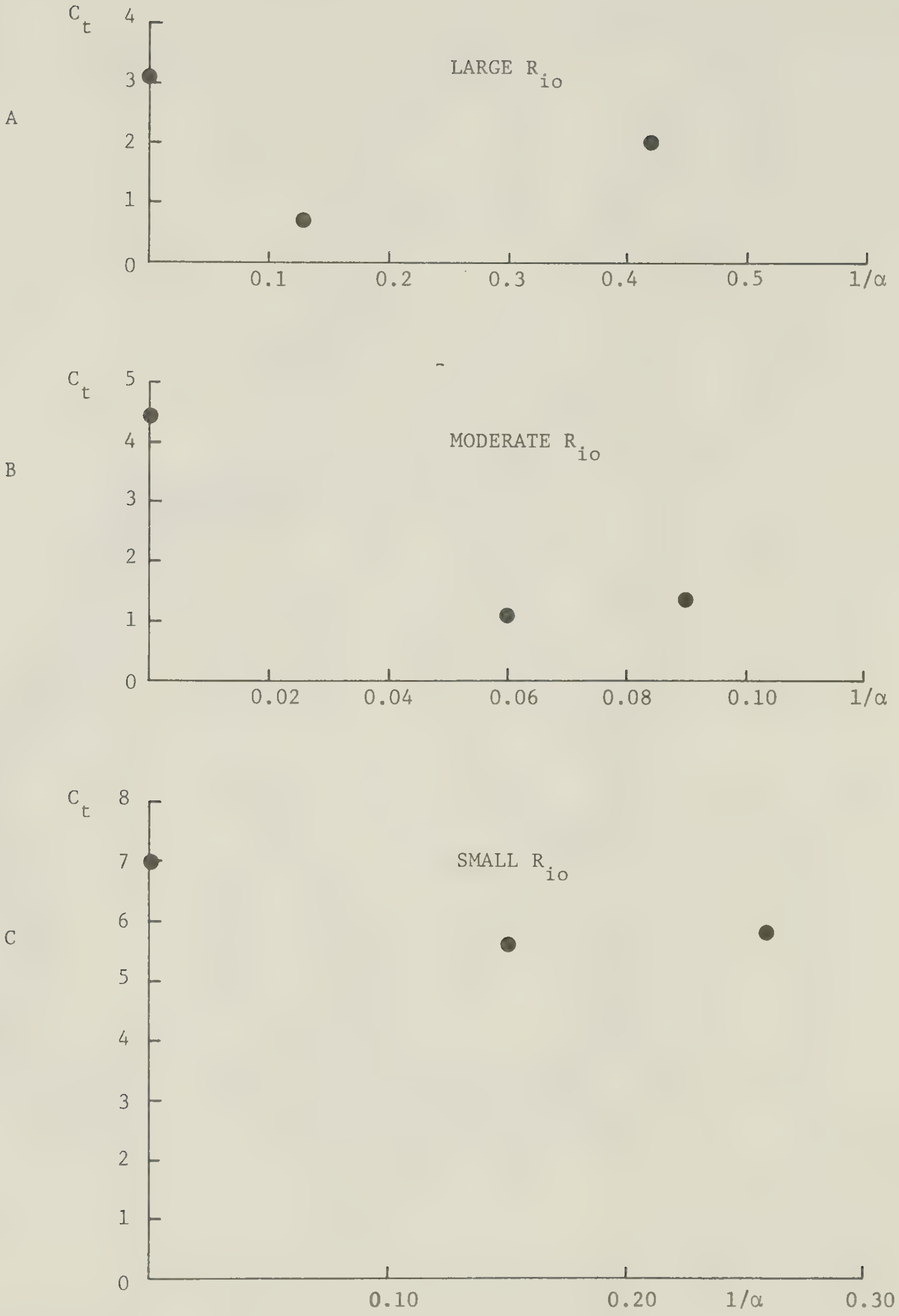

FIGURE 4.21 VARIATION OF TEMPERATURE COEFFICIENTS WITH VELOCITY RATIO

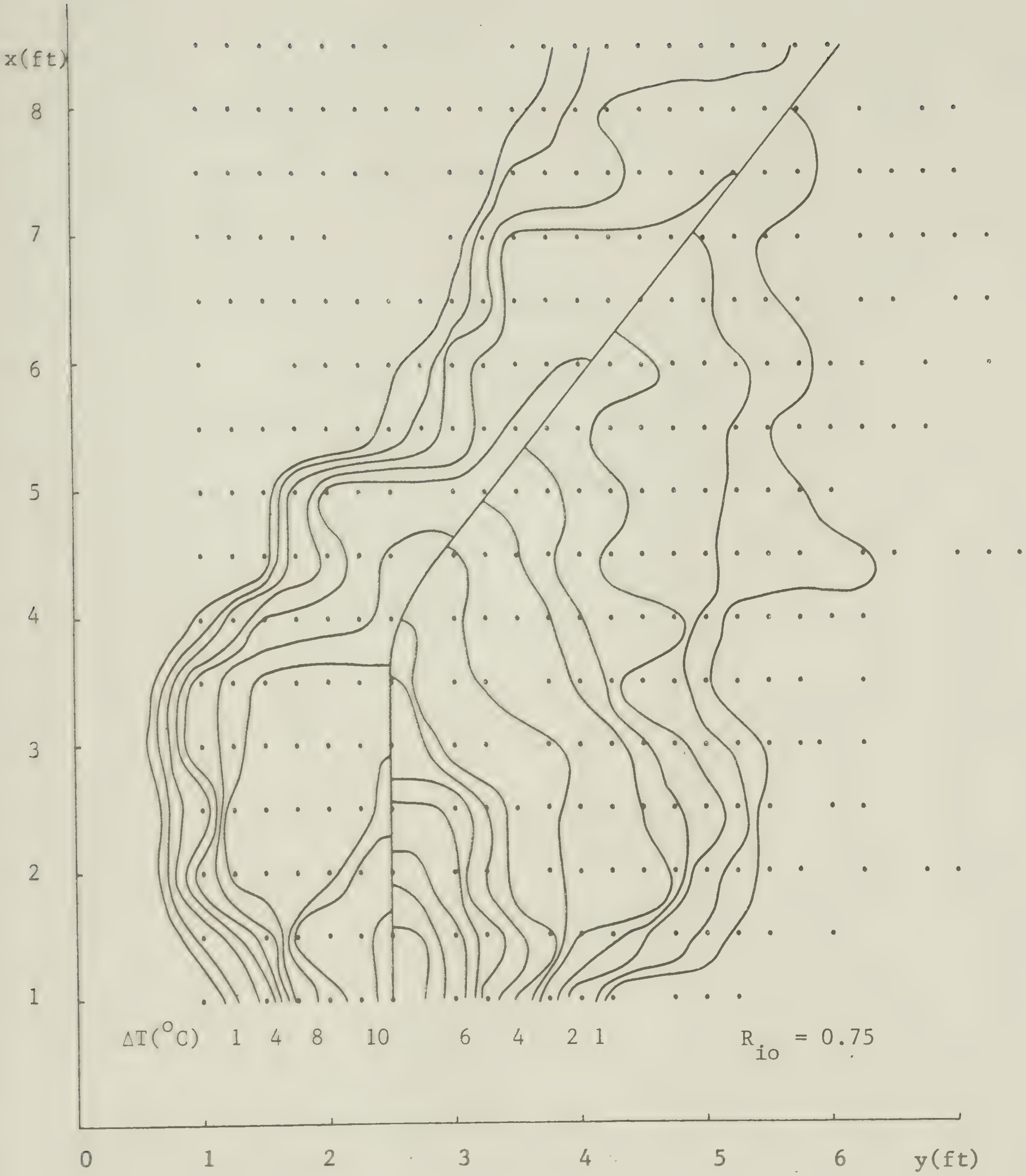

FIGURE 4.22 SURFACE ISOTHERM

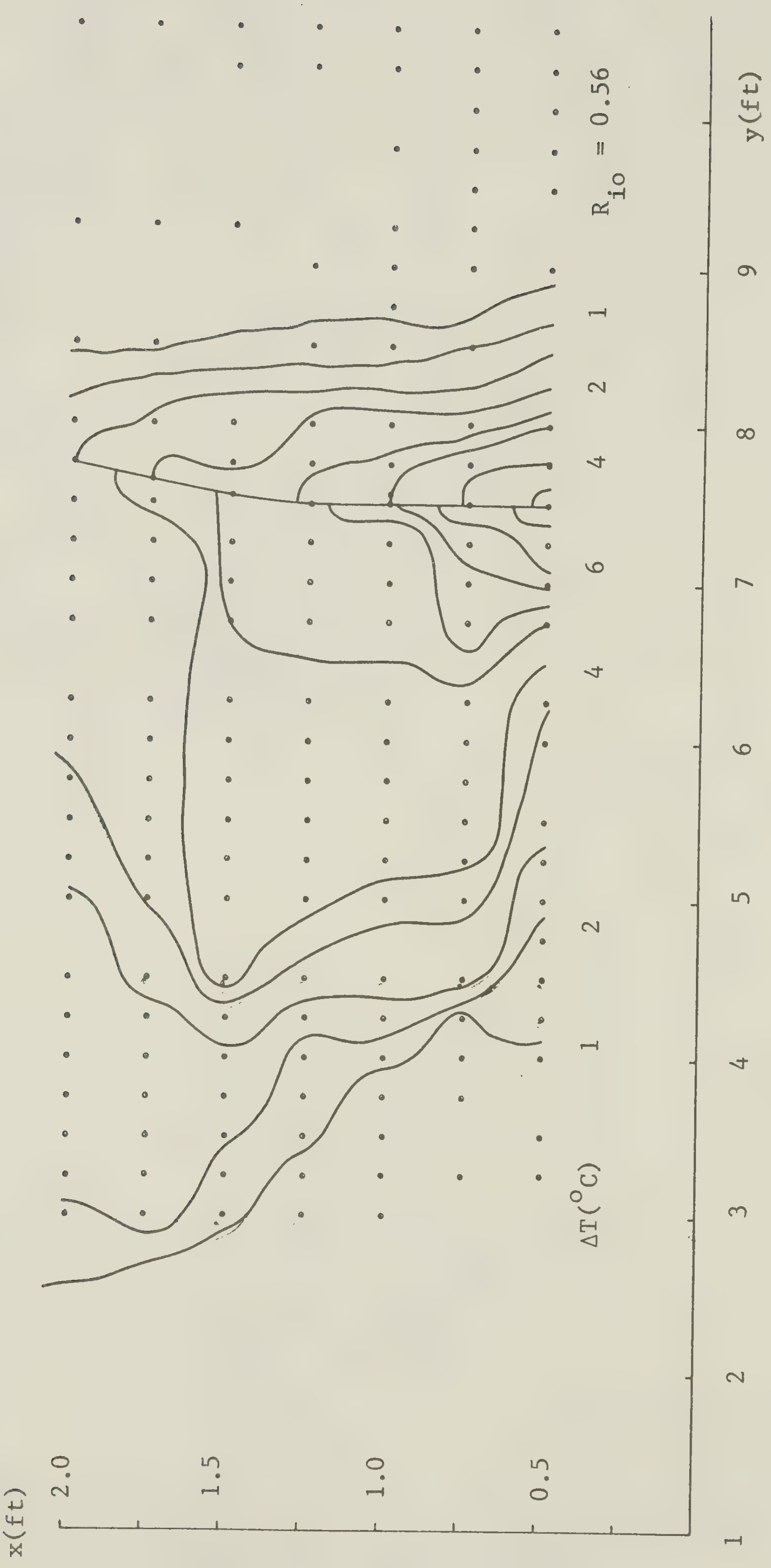

FIGURE 4.22 SURFACE ISOTHERM

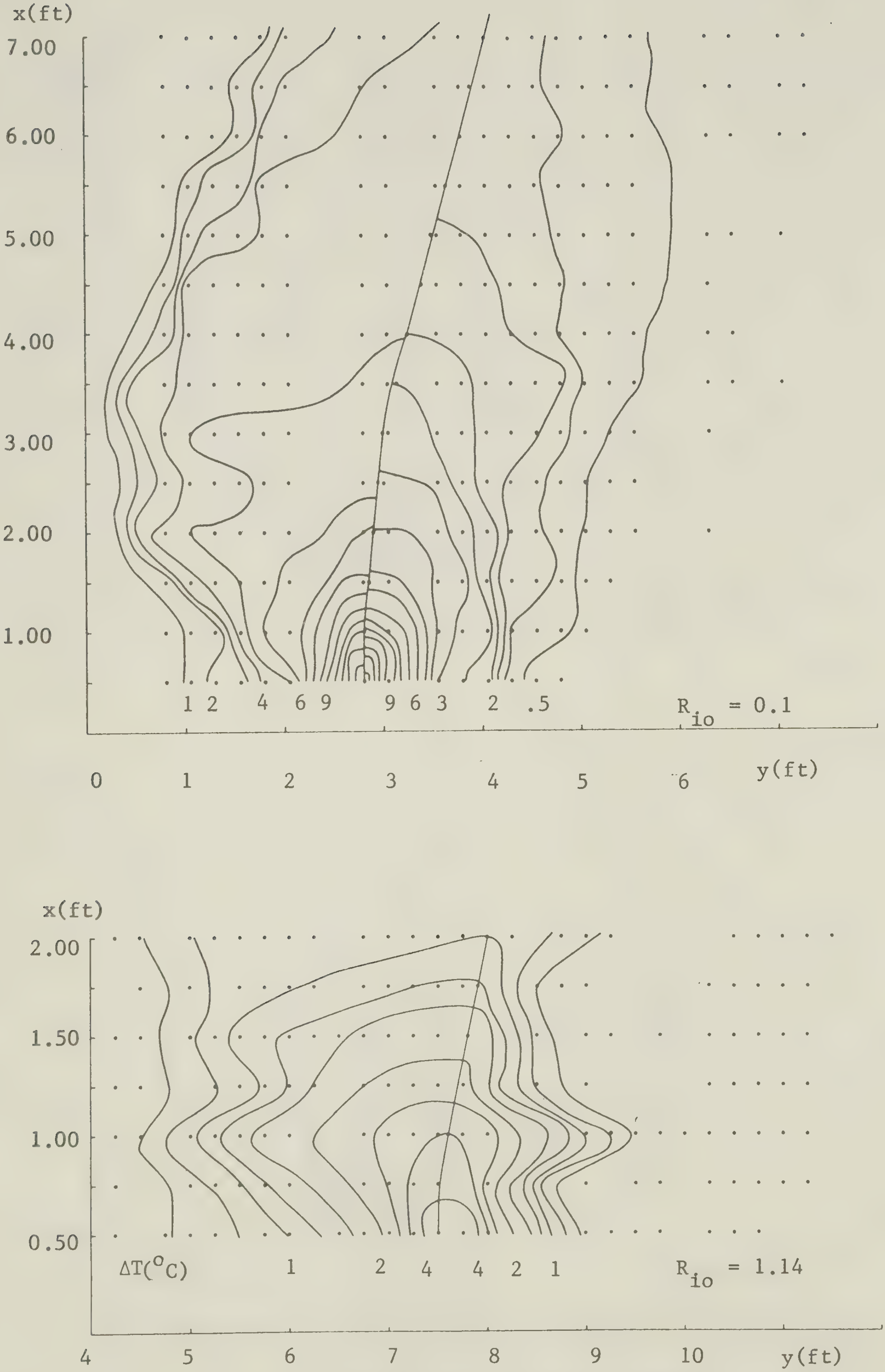

FIGURE 4.22 SURFACE ISOTHERM

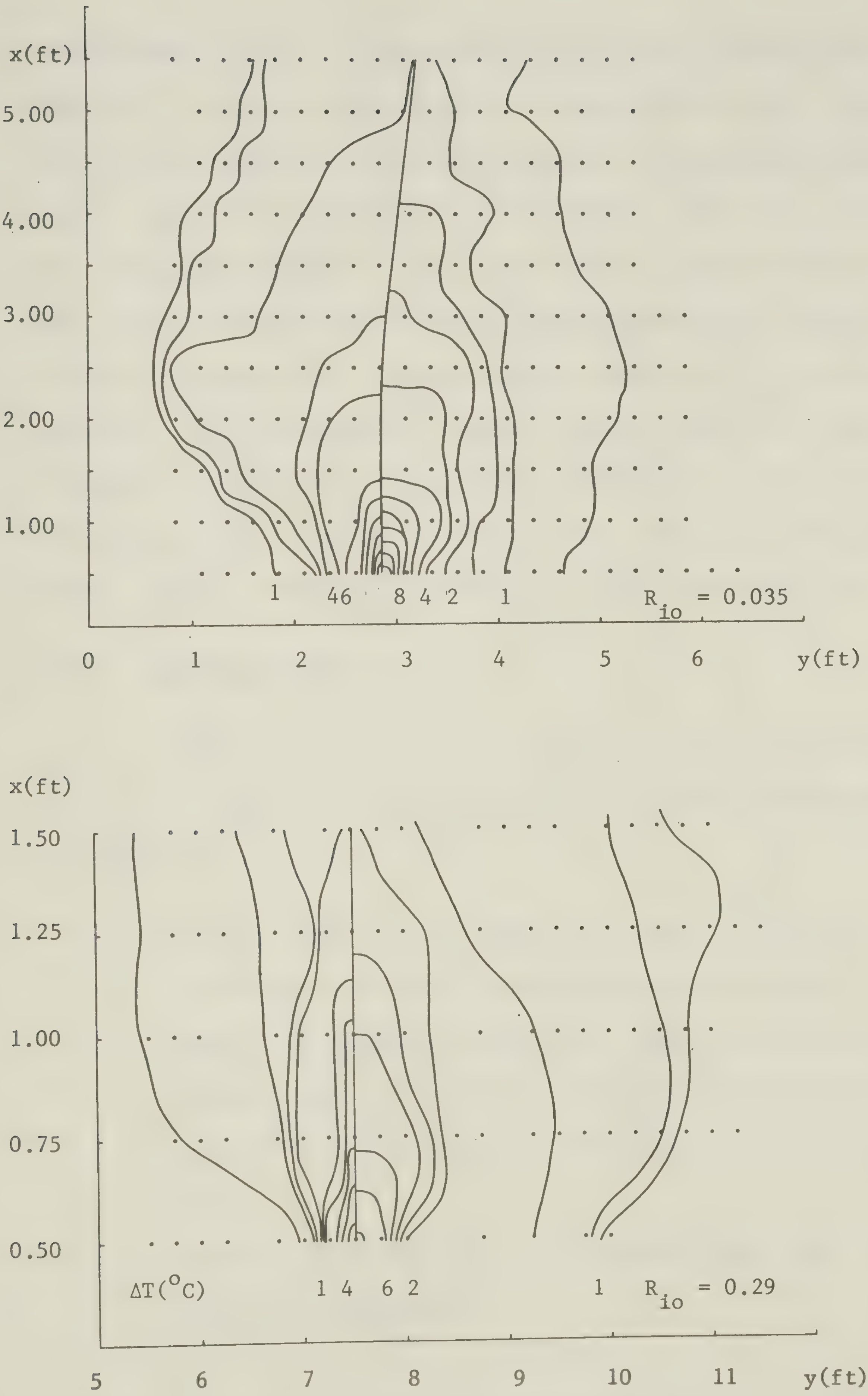

FIGURE 4.22 SURFACE ISOTHERM

downstream side. Hoopes et al. did not observe such behavior in their experiments. Policastro et al. stated that large eddies on the down-current side should cause more extensive spreading on that side. The exact reason for this phenomenon is not known but we believe that when the cooler cross flow reaches the front of the surface jet, it dives underneath the jet simply because of its heavier density. As the ambient current passes under the jet, the motion creates a shear force between the two layers and eventually sets up a circulation within the jet which might cause a greater spreading on the upstream side.

4.10 Jet Trajectory

The jet trajectories for all experiments are shown in Figure 4.23 and Figure 4.24. Three regions can be observed:

1. Undeflected region where the axis of the jet coincides with the centerline of the inlet.
2. Region of maximum deflection where the cross flow affects the jet to the maximum and deflects the axis of the jet towards downstream at a very sharp rate.
3. Region where the jet is directed along the already deflected direction.

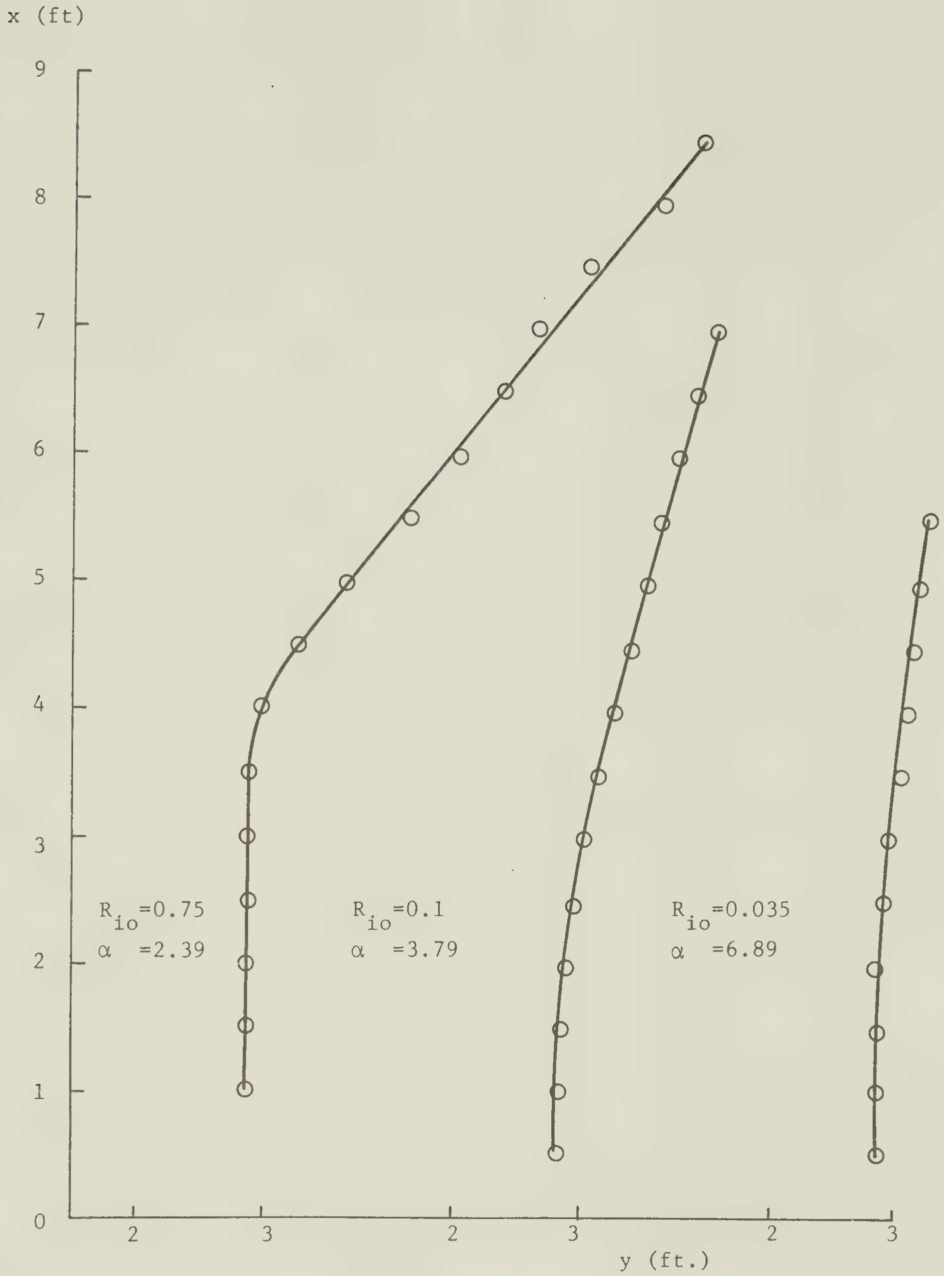

FIGURE 4.23 JET TRAJECTORIES ON SURFACE

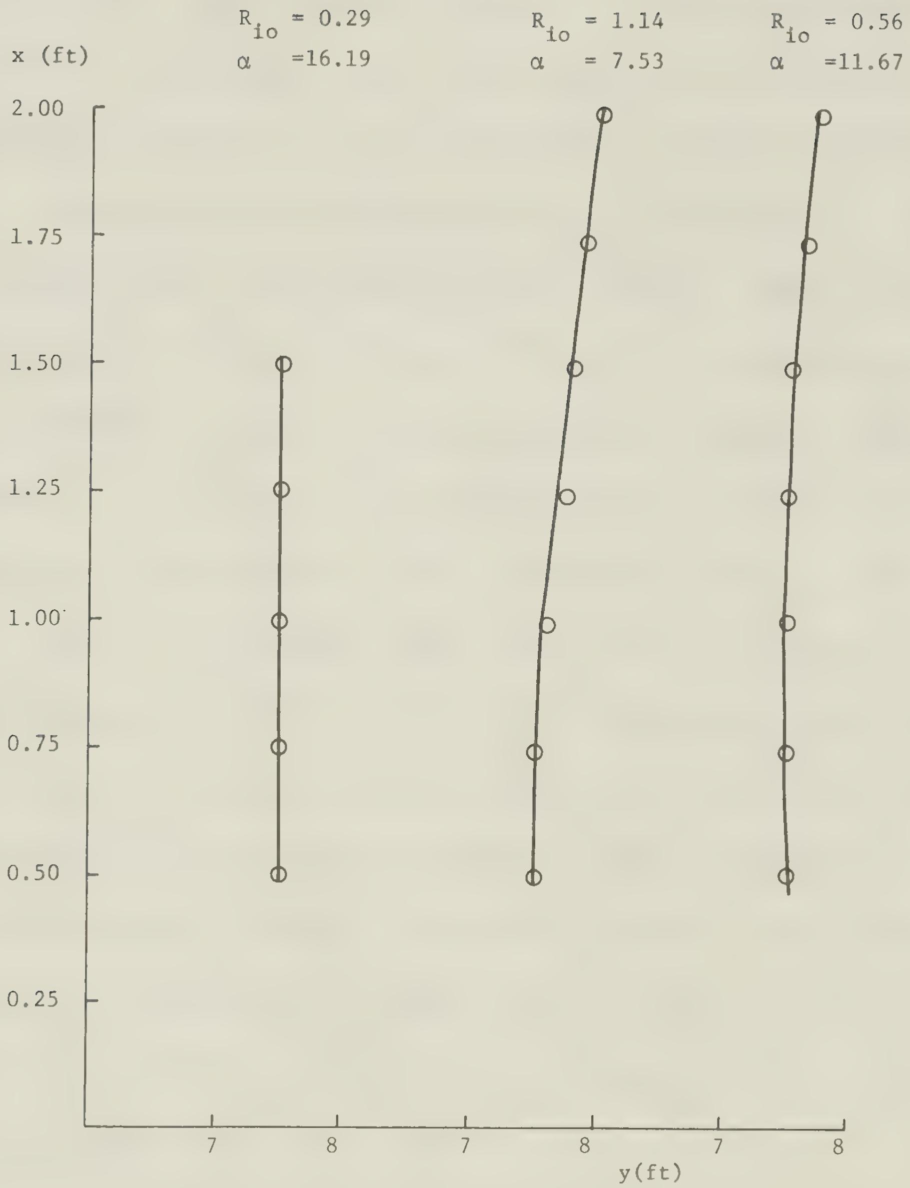

FIGURE 4.24 JET TRAJECTORIES ON SURFACE

These three regions are shown clearly for all runs except for the run with $R_{io} = 0.29$. In that particular run, the strength of the cross flow is so small as compared to the jet velocity that it does not affect the axis at all. In other runs, the degree of bending of the axis depends strongly on the strength of the cross-current.

The angle of deflection θ is defined as the angle between the inlet centerline and the axis of the deflected jet. Values of tan θ for all experiments are given in Table 4.3 and are also plotted against the velocity ratio α in Figure 4.25 along with the data from Motz and Benedict. Though the data scatters quite a lot, a general trend is noticed. The same data is again plotted on a log paper in Figure 4.26. In this plot, the angle of deflection is normalized by the angle of discharge. With the additional data from Motz and Benedict, a straight line can be drawn through the data points. To observe the effect of Richardson number on the angle of deflection, we plot tan θ $(R_{io})^k$ against α in Figure 4.27. A straight line having the form

$$\text{Tan}\ \theta = (R_{io})^{-k}\ (0.741 - 0.045\alpha) \tag{4.10.1}$$

can be drawn through the data. k is an exponent that has to be determined by a trial and error procedure; and is found equal to -1/3 for small Richardson number and 3/4

EXP No	α	R_{io}	TAN θ	θ (DEGREE)	TAN θ $(R_{io})^k$
1	2.39	0.75	0.80	38.66	0.64
2	3.80	0.10	0.24	13.50	0.52
3	6.89	0.035	0.14	7.97	0.43
4	16.20	0.29	0.00	0.00	0.00
5	7.53	1.14	0.40	21.80	0.44
6	11.67	0.56	0.34	18.78	0.22

NOTE: for small R_{io} $k = -1/3$

for moderate & large R_{io} $k = 3/4$

Table 4.3 Analysis of Jet Trajectory

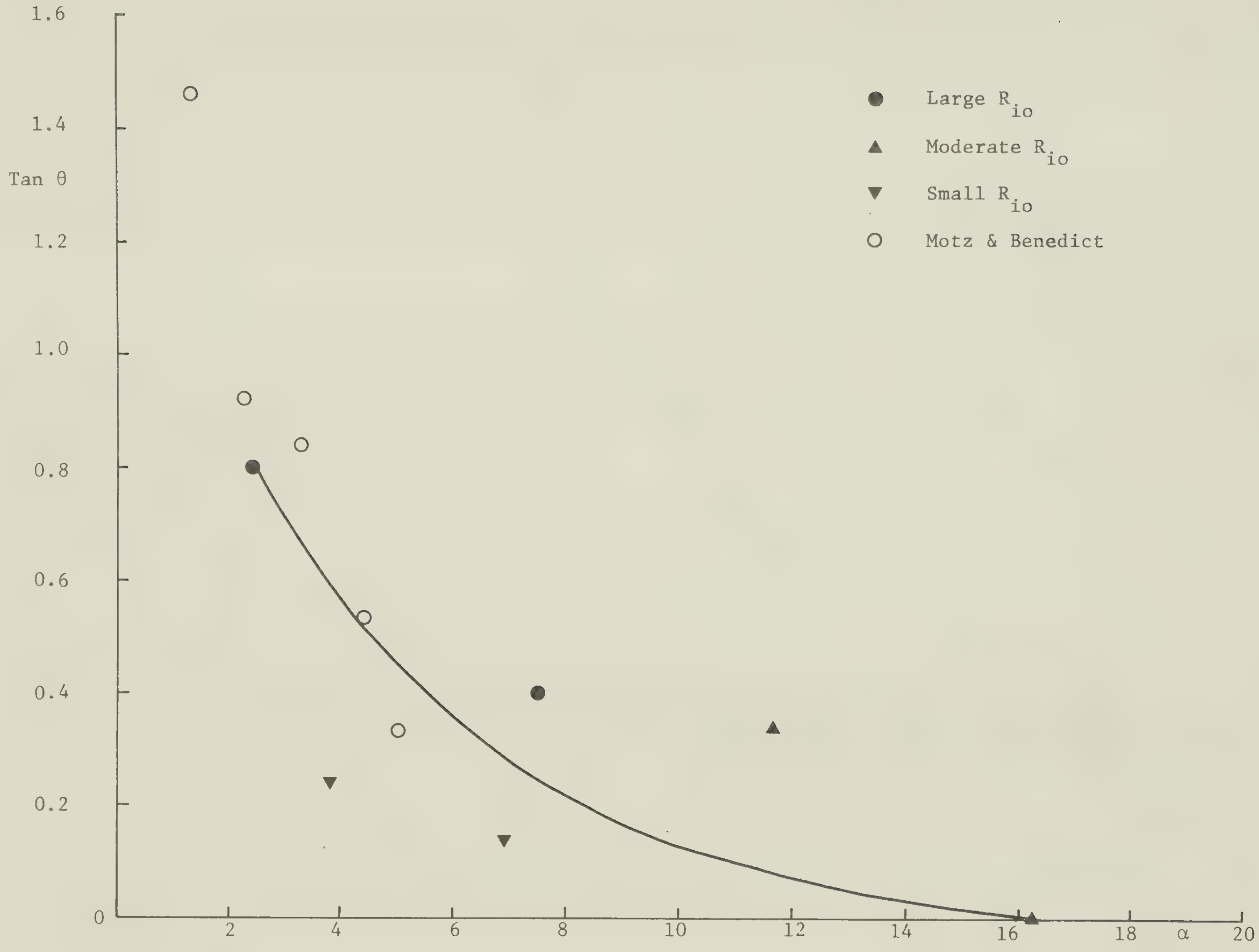

FIGURE 4.25 VARIATION OF ANGLES OF DEFLECTION WITH VELOCITY RATIO

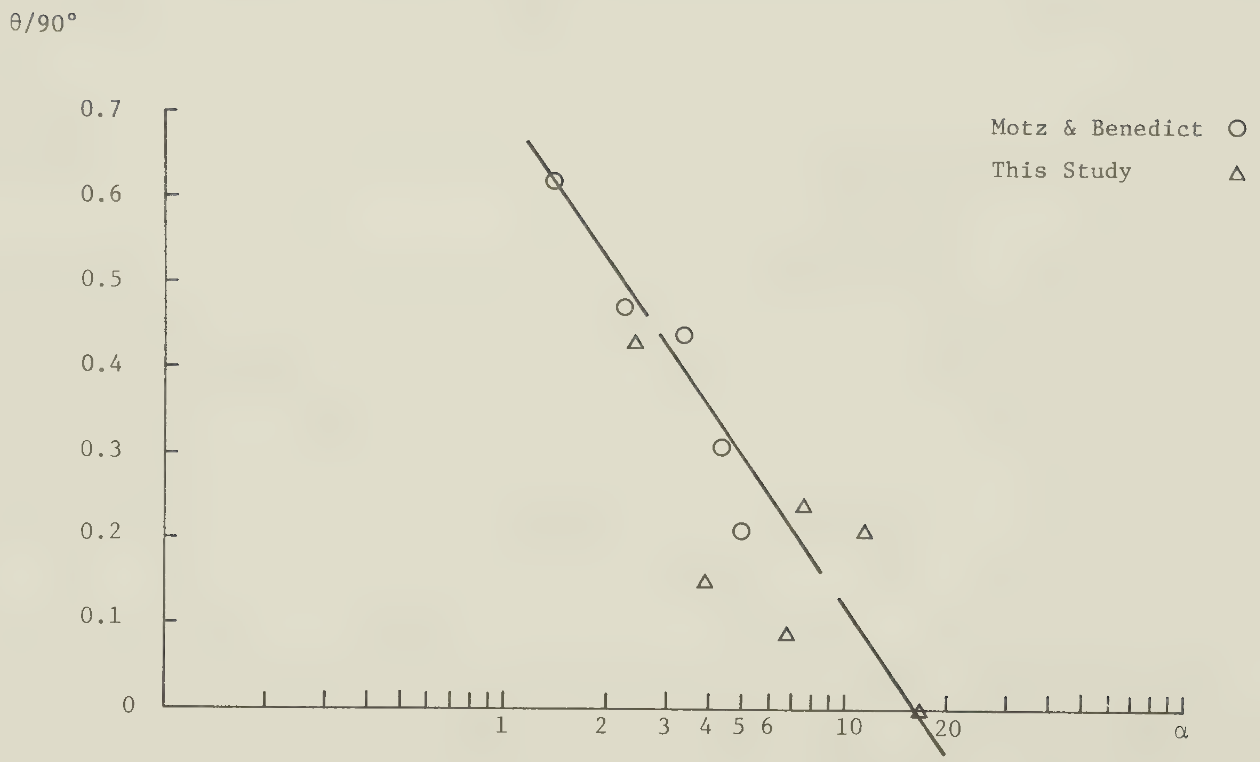

FIGURE 4.26 NON-DIMENSIONAL PLOT OF ANGLE OF DEFLECTION AGAINST VELOCITY RATIO

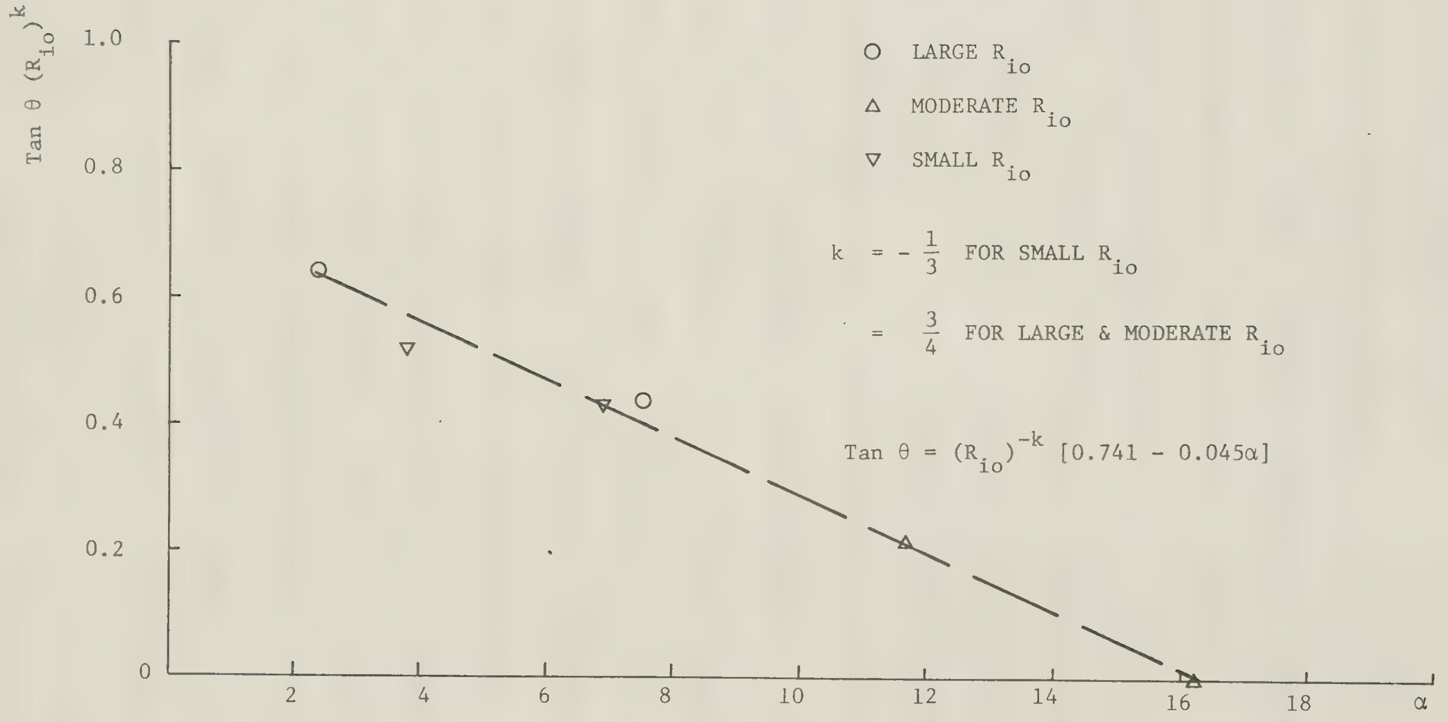

FIGURE 4.27 CORRELATION OF RICHARDSON NUMBER AND ANGLE OF DEFLECTION WITH THE VELOCITY RATIO

for both the moderate and large Richardson numbers.

4.11 Variation of Half-Width

The surface temperature half-width b is defined as the distance on the surface measured perpendicular to the jet axis where the temperature excess $(T - T_a)$ is half the axis temperature excess $(T_m - T_a)$. A dimensionless plot of b/b_o vs. x_1/b_o is shown in Figure 4.28. The data points fall within a kidney-shape area except the upstream half-width for $R_{io} = 0.56$. In that particular run, the upstream half-width grows very rapidly and has a magnitude much greater than the other measurements. The half-width for upstream and downstream are plotted separately for all experiments in Figure 4.29 and Figure 4.30. For large and small Richardson numbers, the half-width grows linearly with x_1; but for moderate Richardson number, it varies as $x_1^{4/3}$. This behavior is consistent with previous study by Pande without ambient current. At some distance from the inlet, the half-width drops off which indicates that the ambient current comes into effect therein and restricts the spreading of the jet towards the upstream. The upstream half-width of run with $R_{io} = 0.75$ shows a very irregular pattern and no reasonable explanation is found.

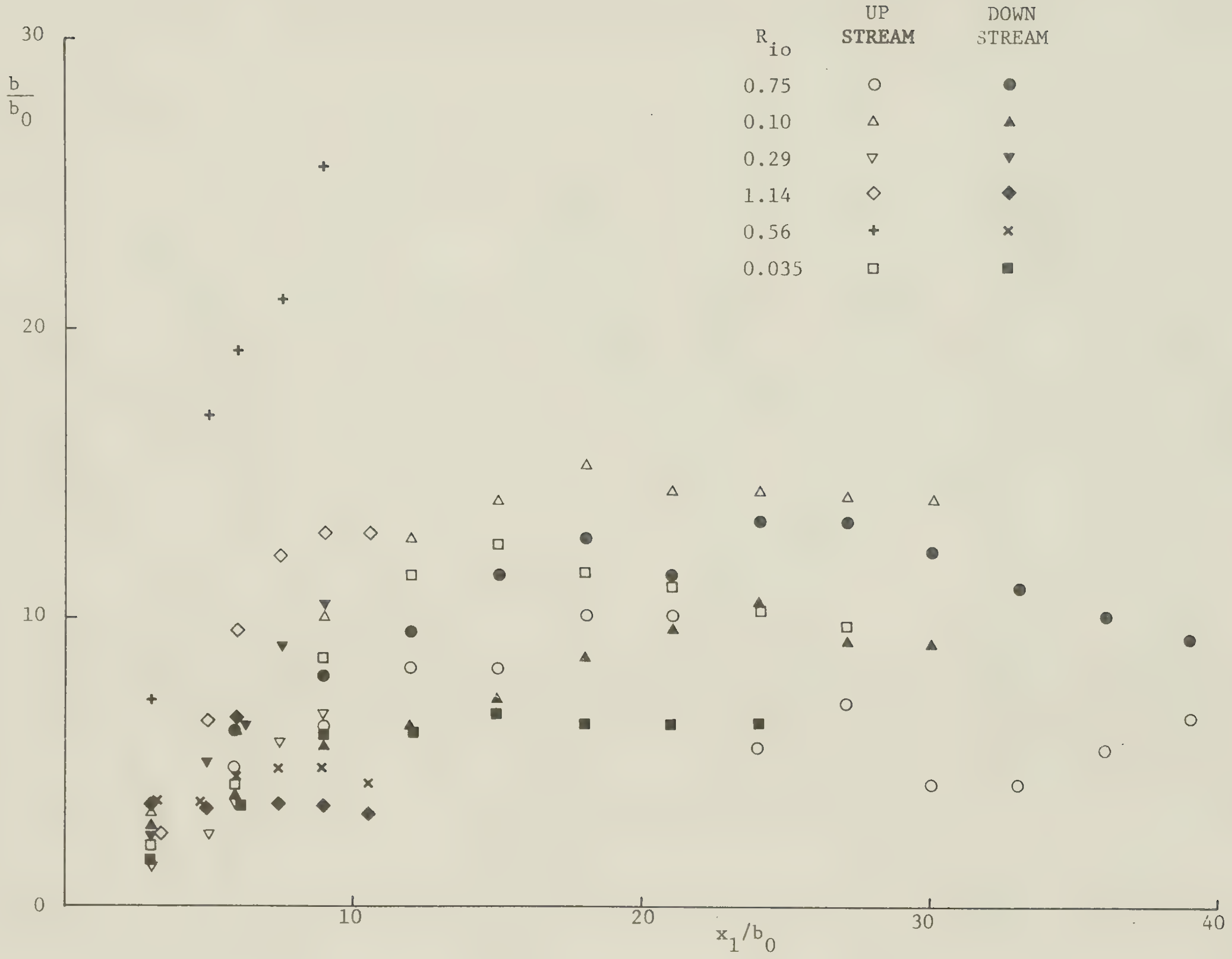

FIGURE 4.28 NON-DIMENSIONAL PLOT OF HALF-WIDTH

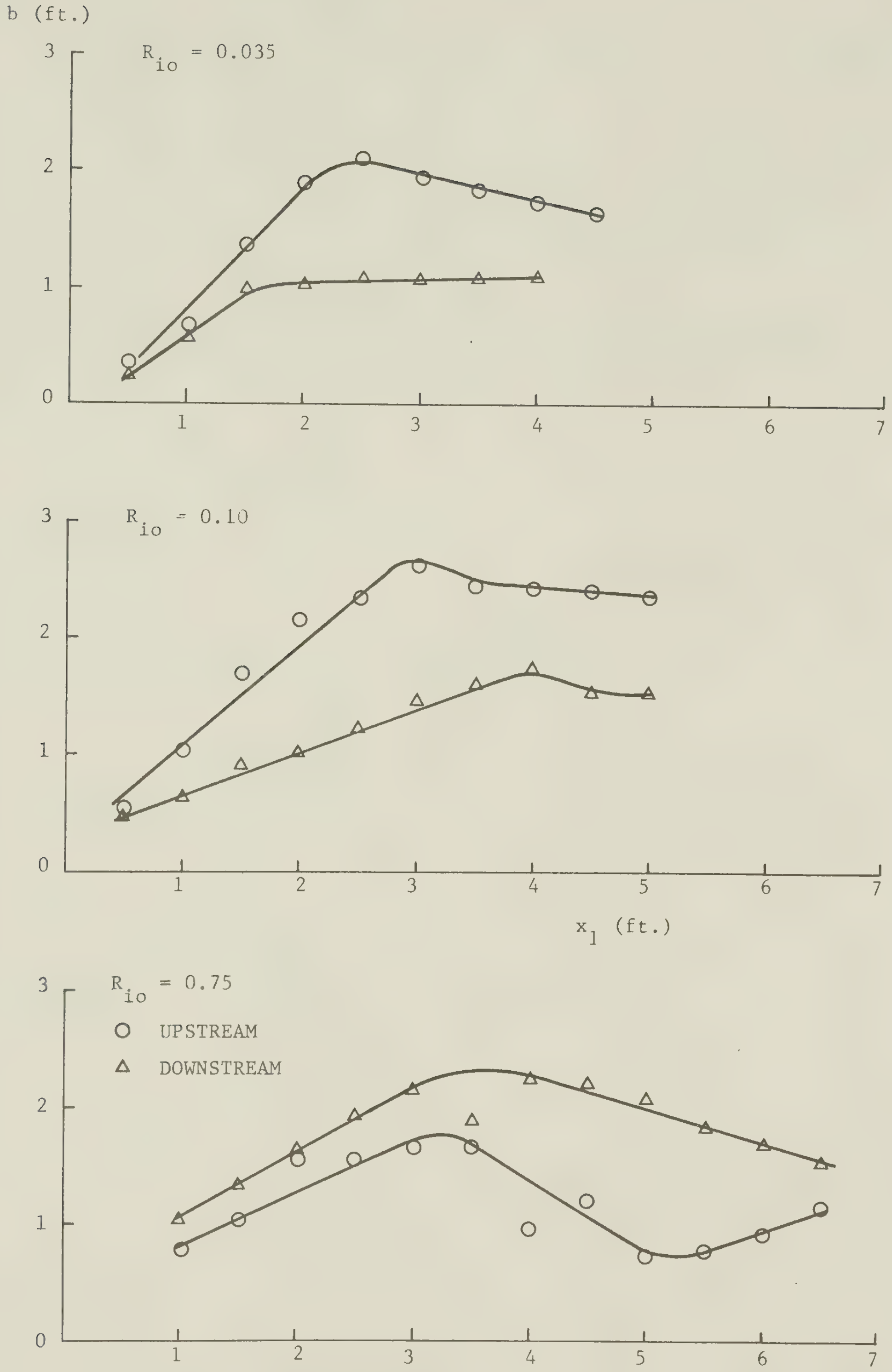

FIGURE 4.29 VARIATION OF HALF-WIDTH WITH DISTANCE ALONG JET AXIS

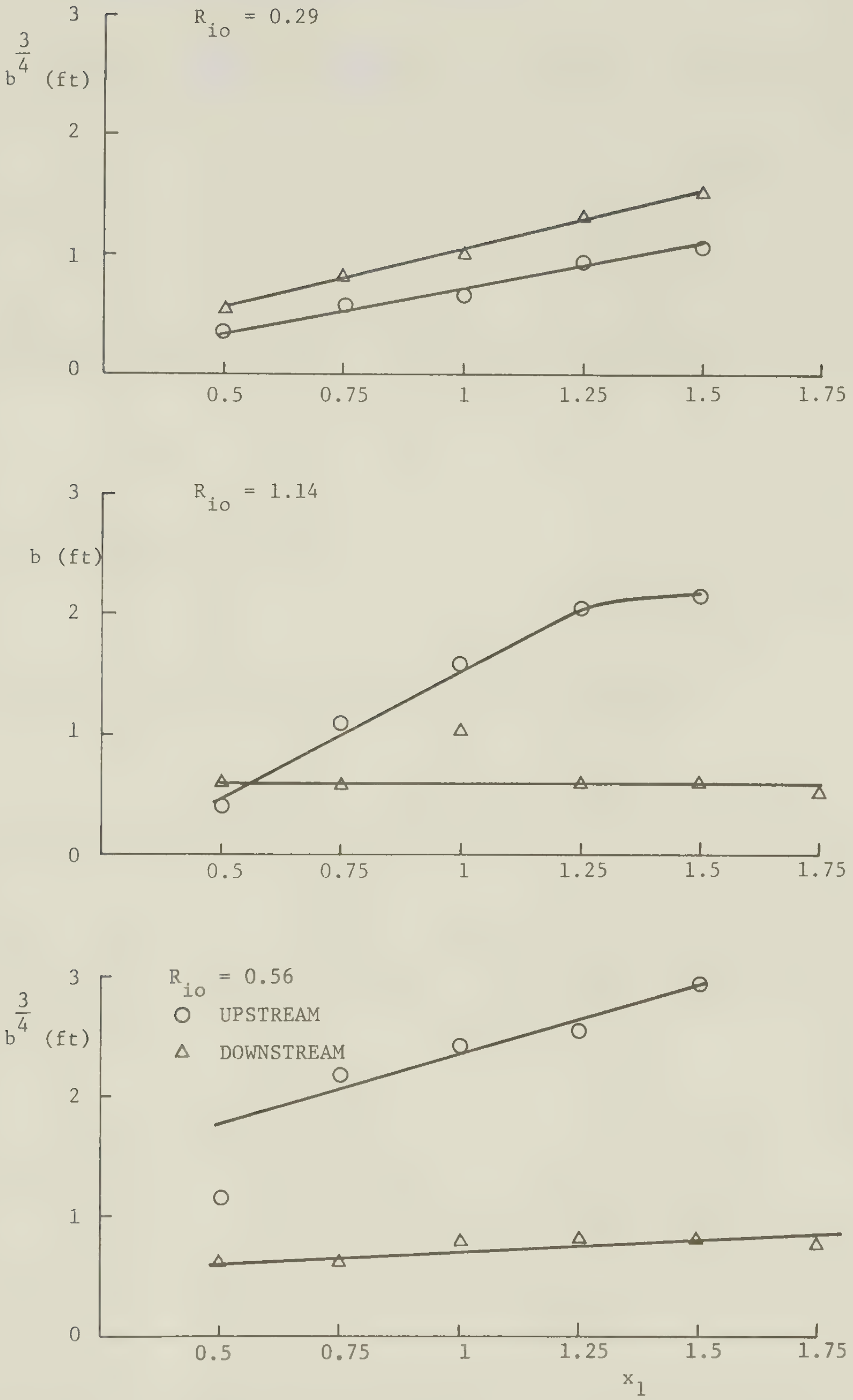

FIGURE 4.30 VARIATION OF HALF-WIDTH WITH DISTANCE ALONG JET AXIS

Large Richardson Number

For large Richardson number, the half-width varies as x_1. A non-dimensional plot of b_a/b_o against x_1/b_o for $R_{io} = 0.75$ and 1.14 is shown in Figure 4.31 where b_a is the average of the upstream and downstream half-widths. Pande gave the following equation in his study.

$$\frac{2b}{b_o} = 1.83\ (R_{io})^{1/8} \left(\frac{x_1}{b_o} + 1 \right) \qquad (4.11.1)$$

A half-width coefficient C_b is defined as:

$$\frac{2b_a}{b} = C_b\ (R_{io})^{1/8} \left(\frac{x_1}{b_o} + C_2 \right)$$

In Figure 4.31, the straight lines have the equations:

for $R_{io} = 0.75$

$$\frac{2b_a}{b} = 1.01\ (R_{io})^{1/8} \left(\frac{x_1}{b_o} + 6 \right) \qquad (4.11.2)$$

for $R_{io} = 1.14$

$$\frac{2b_a}{b} = 2.09\ (R_{io})^{1/8} \left(\frac{x_1}{b_o} \right) \qquad (4.11.3)$$

The tabulated values for C_b and α are given in Table 4.4

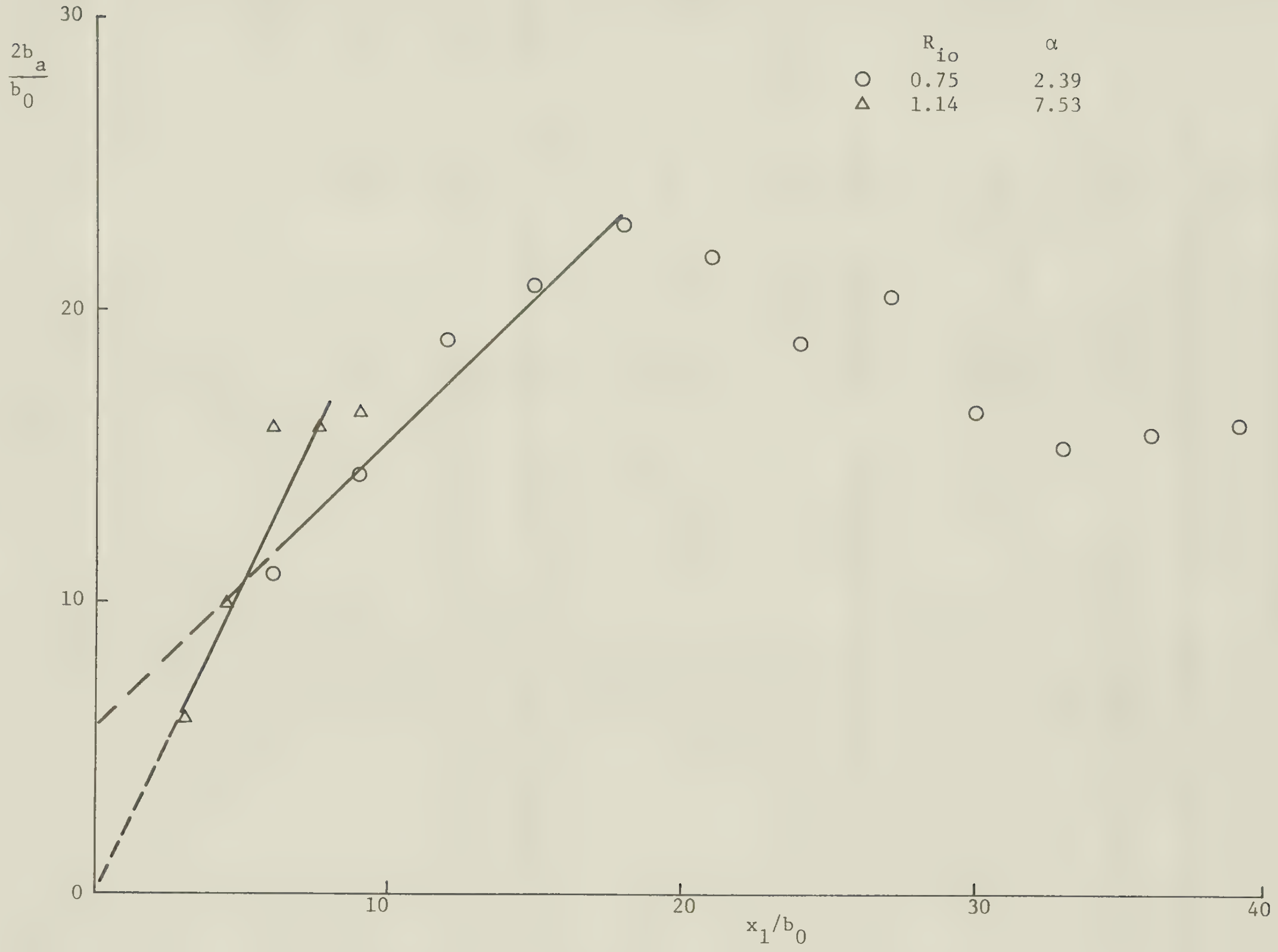

FIGURE 4.31 NON-DIMENSIONAL PLOT OF HALF-WIDTH FOR LARGE R_{io}

and the plot of C_b against $1/\alpha$ is shown in Figure 4.34.

Moderate Richardson Number

For moderate Richardson number, the half-width coefficient C_b is defined by the following equation:

$$\frac{2b_a}{b_o} = C_b \; (R_{io})^{1/6} \; \left(\frac{x_1}{b_o} + C_2\right)^{4/3}$$

Pande found the following equation fit his experimental data well:

$$\frac{2b}{b_o} = 0.81 \; (R_{io})^{1/6} \; \left(\frac{x_1}{b_o} + 2\right)^{4/3} \qquad (4.11.4)$$

$(2b_a/b_o)^{3/4}$ is plotted against x_1/b_o in Figure 4.32 for $R_{io} = 0.29$ and 0.56. The equations that fit the data are:

for $R_{io} = 0.29$

$$\left(\frac{2b_a}{b_o}\right) = 1.13 \; (R_{io})^{1/6} \; \left(\frac{x_1}{b_o}\right)^{4/3} \qquad (4.11.5)$$

and for $R_{io} = 0.56$

$$\left(\frac{2b_a}{b_o}\right) = 1.36 \; (R_{io})^{1/6} \; \left(\frac{x_1}{b_o} + 2.5\right)^{4/3} \qquad (4.11.6)$$

The parameter C_2 is determined from the experimental data.

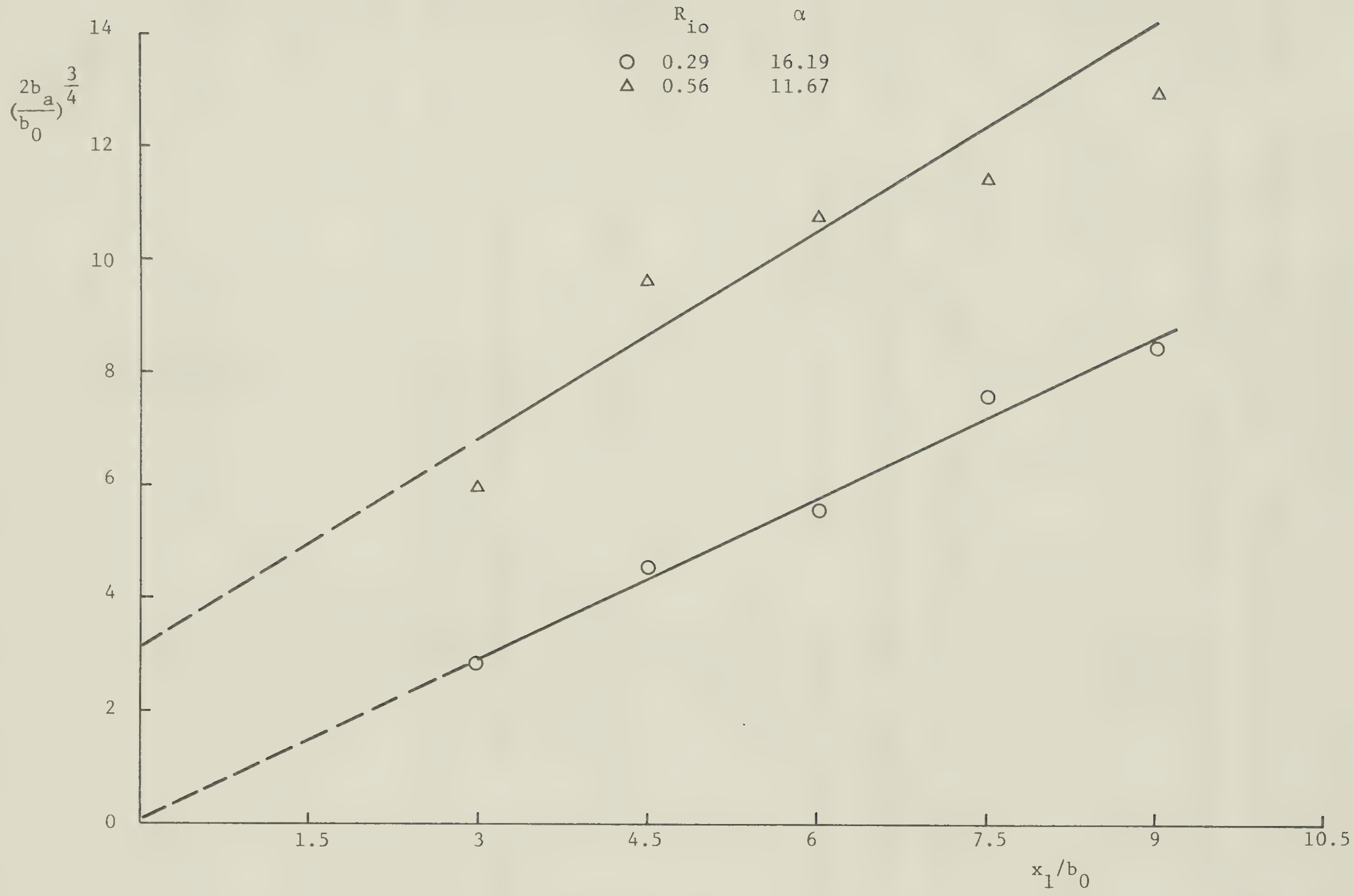

FIGURE 4.32 NON-DIMENSIONAL PLOT OF HALF-WIDTH FOR MODERATE R_{io}

Small Richardson Number

For small Richardson number, the half-width is directly proportion to x_1. Pande has no data for small R_{io}; but we define the half-width coefficient as:

$$\frac{2b_a}{b_o} = C_b \, (R_{io})^{1/8} \left(\frac{x_1}{b_o} + C_2\right)$$

Wiegel and his associates related the half-width of the jet to the Richardson number and longitudinal distance for a circular surface jet. Their findings give the equation:

$$\frac{2b_a}{b_o} = 1.14 \, (R_{io})^{1/8} \, \frac{x_1}{b_o} \qquad (4.11.7)$$

The non-dimensional plots for small Richardson number are given in Figure 4.33. The forms of the equations we found are:

for $R_{io} = 0.1$

$$\frac{2b_a}{b_o} = 1.68 \, (R_{io})^{1/8} \left(\frac{x_1}{b_o} + 2.4\right) \qquad (4.11.8)$$

and for $R_{io} = 0.035$

$$\frac{2b_a}{b_o} = 2.31 \, (R_{io})^{1/8} \left(\frac{x_1}{b_o} - 0.8\right) \qquad (4.11.9)$$

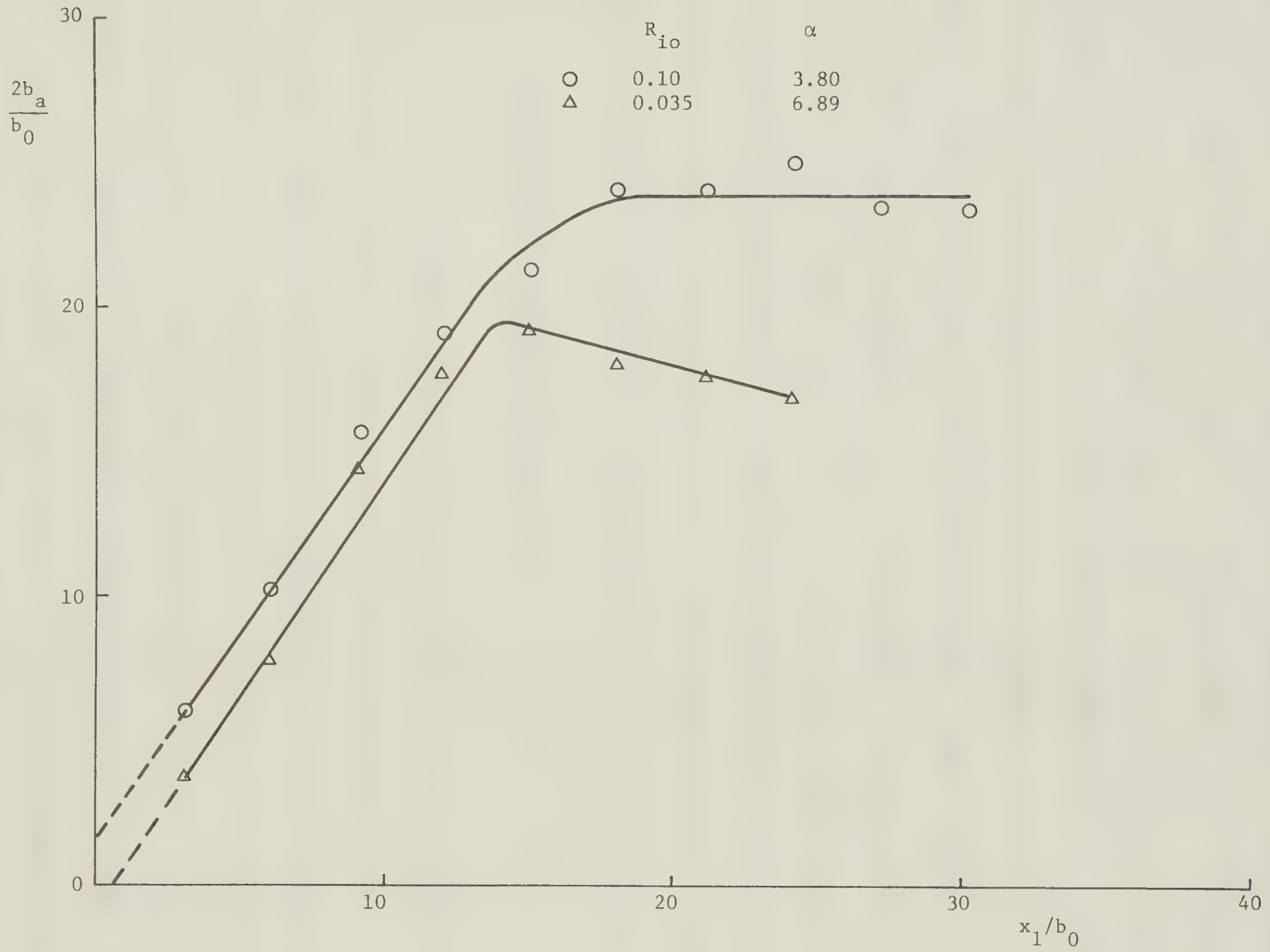

FIGURE 4.33 NON-DIMENSIONAL PLOT OF HALF-WIDTH FOR SMALL R_{io}

The values of C_b for all experiments are tabulated in Table 4.5 and then plotted against $1/\alpha$ in Figure 4.34. We find that C_b increases to a maximum value with α approaching an optimum value and then further decrease in α results in decreasing values of C_b. The optimum value for α and the maximum value for C_b are different for different Richardson number groups. The ratio of the upstream (and downstream) half-width to the total half-width against x_1 is plotted in Figure 4.35. The plot shows that the ratio of upstream (and downstream) half-width to the total width is a constant regardless the distance along the jet axis for all experiments. This ratio is plotted against the velocity ratio in Figure 4.36.

4.12 Variation of Half-Depth

The experimental results on the half-depth for all runs are shown in Figure 4.37 and Figure 4.38. For large and moderate Richardson numbers, the half-depths are practically invariant with the axial distance as predicted by Pande. For small Richardson number, the theory predicts a linearly increasing half-depth. In the run with $R_{io} = 0.1$, we observe a decreasing in half-depth along the axis; in other words, the jet is getting thinner and thinner. The reason for this abnormal behavior is not well understood but we believe that the buoyancy plays an

EXP NO	$R_{i\theta}$	$\frac{b_u}{b_u + b_d} \times 100\%$	$\frac{b_d}{b_u + b_d} \times 100\%$
1	0.75	42	58
2	0.10	62	38
3	0.035	62	38
4	0.29	37	63
5	1.14	70	30
6	0.56	82	18

Table 4.4 Values of Spreading Ratios

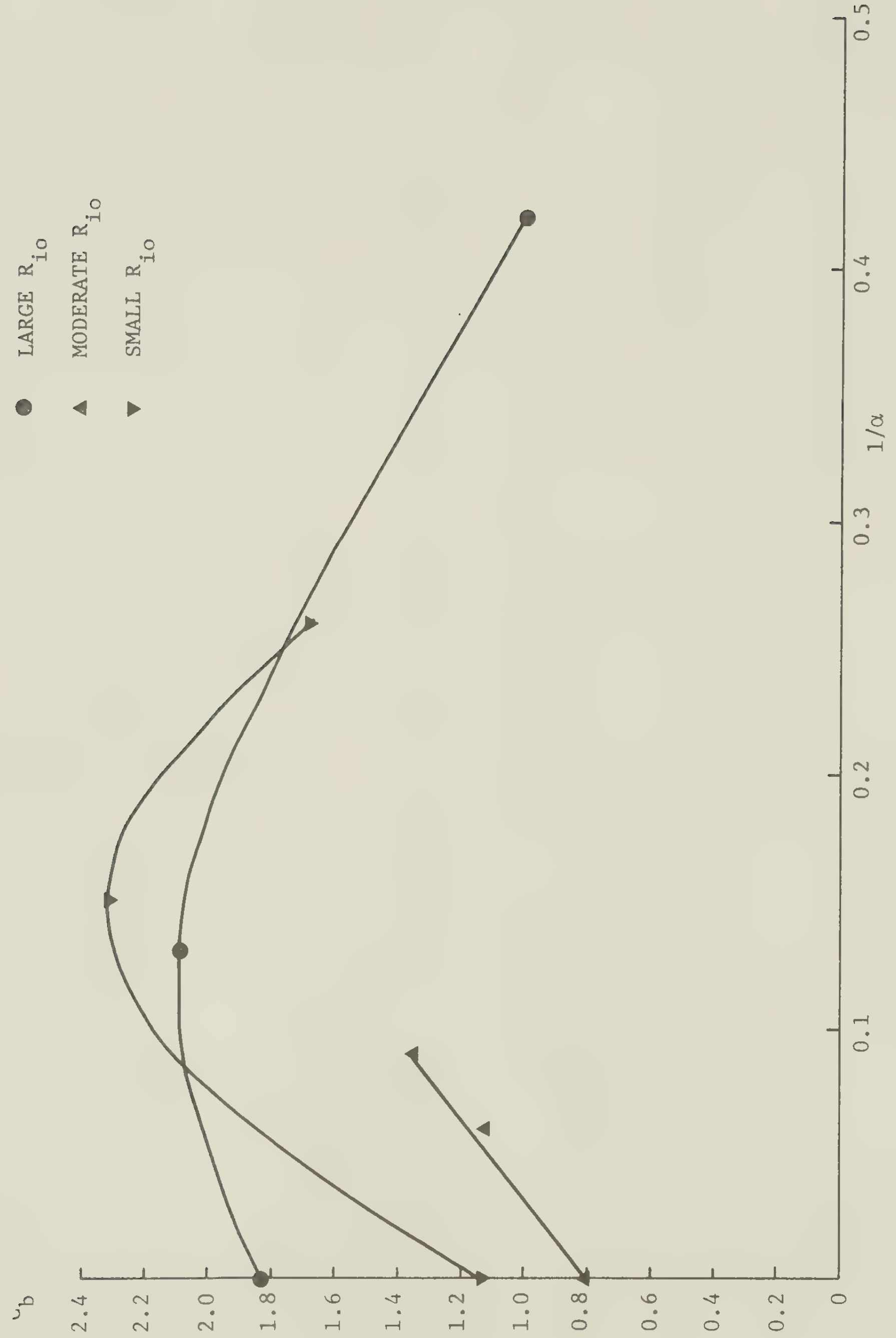

FIGURE 4.34 CORRELATION OF HALF-WIDTH COEFFICIENT WITH THE VELOCITY RATIO

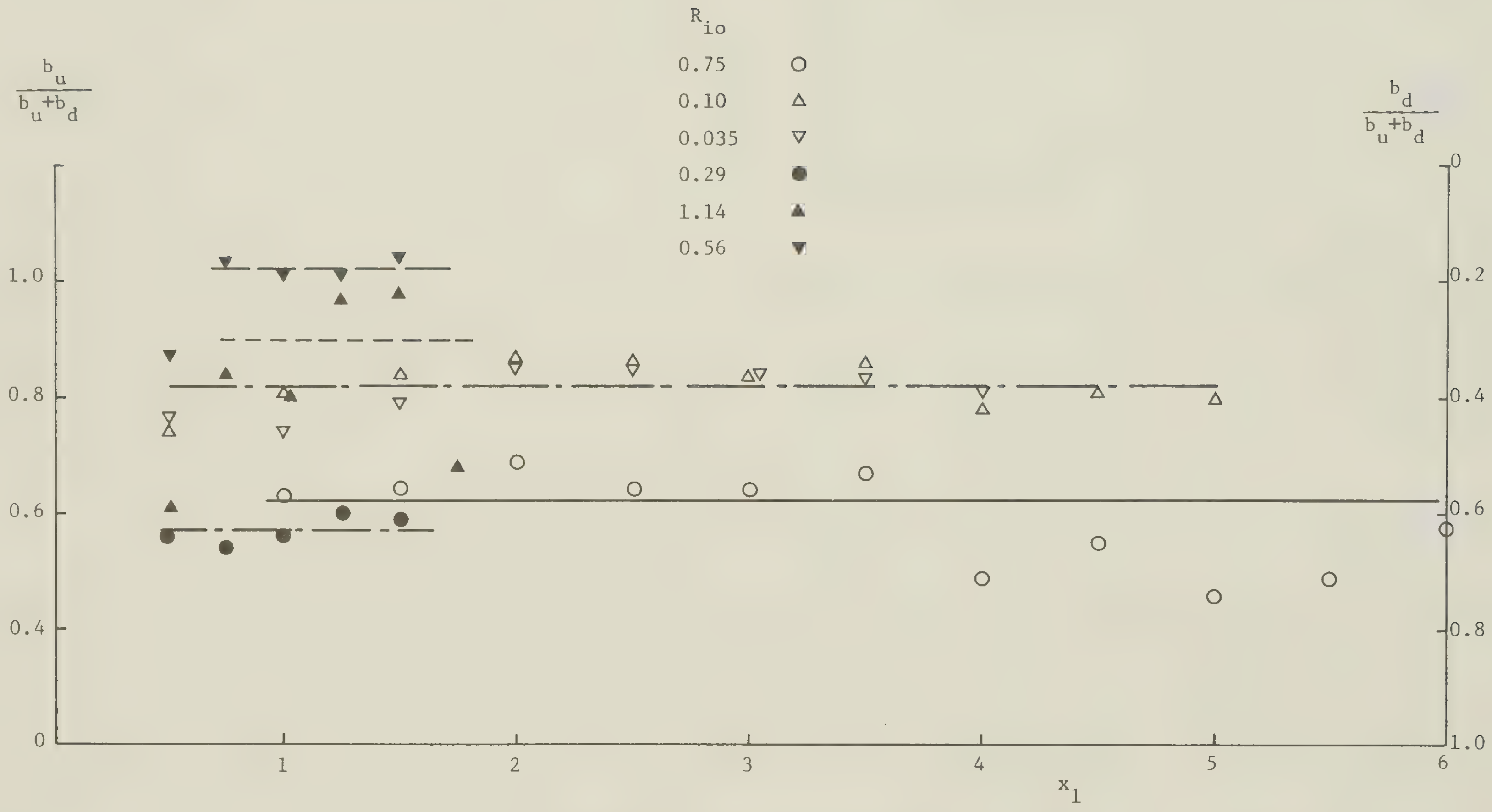

FIGURE 4.35 JET EXPANSION RATIO

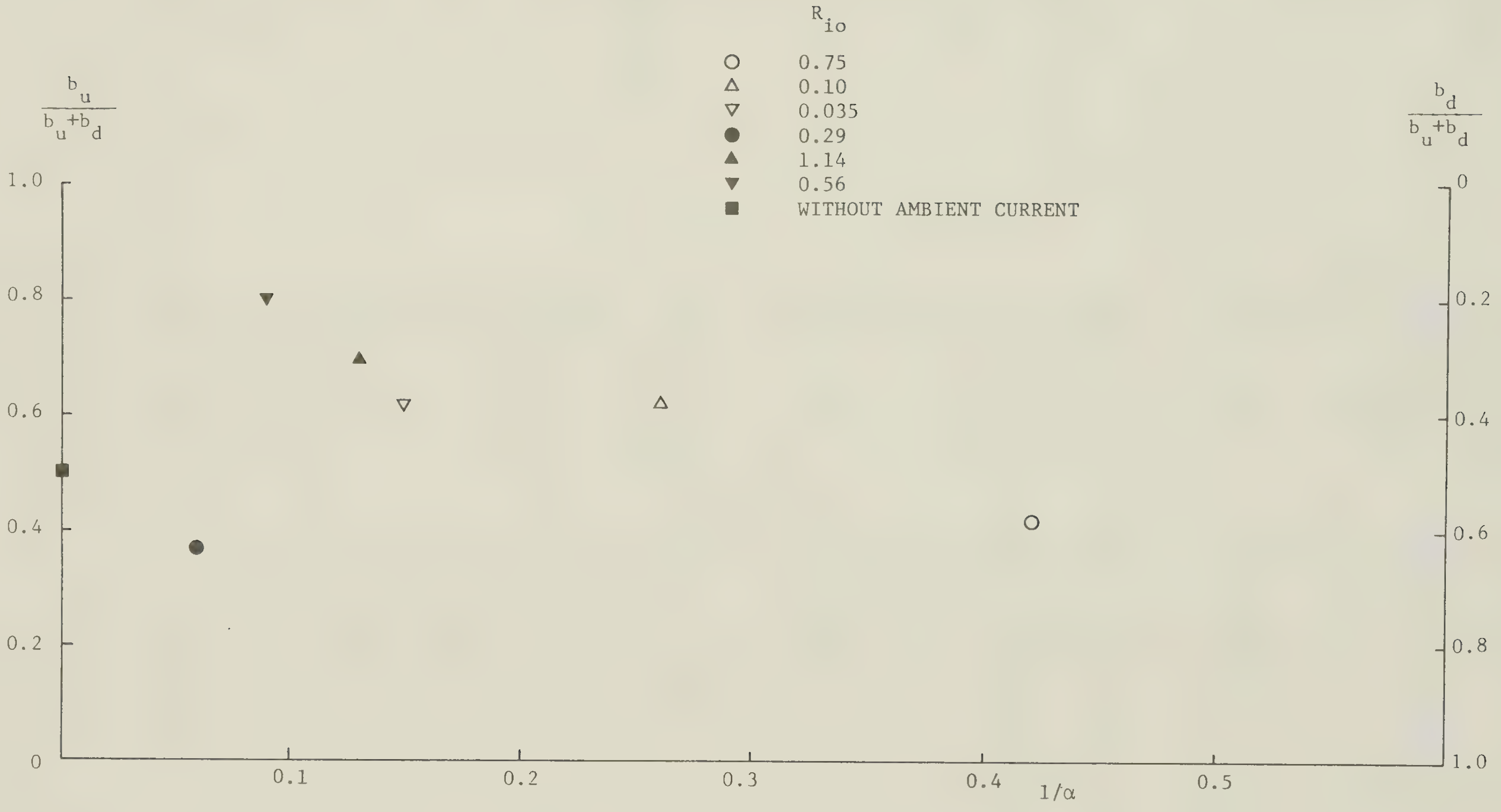

FIGURE 4.36 JET EXPANSION RATIO AGAINST VELOCITY RATIO

LARGE R_{io}

EXP NO	$1/\alpha$	C_b
PANDE	0	1.83
1	0.42	1.00
5	0.13	2.09

MODERATE R_{io}

EXP NO	$1/\alpha$	C_b
PANDE	0	0.81
4	0.06	1.13
6	0.09	1.36

SMALL R_{io}

EXP NO	$1/\alpha$	C_b
WIEGEL	0	1.14
2	0.26	1.68
3	0.15	2.31

Table 4.5 Values of Half-Width Coefficient

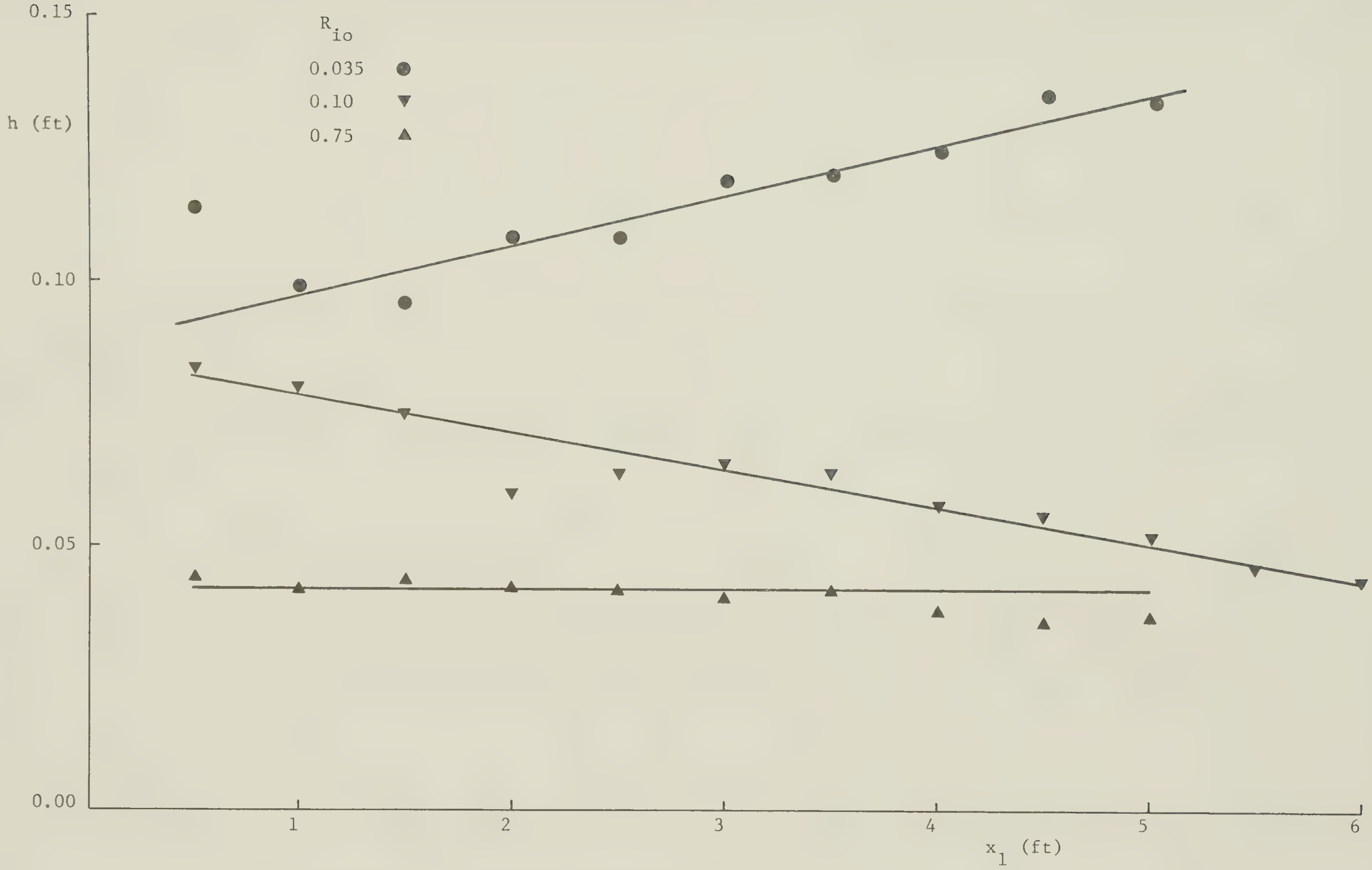

FIGURE 4.37 VARIATION OF HALF-DEPTH WITH DISTANCE ALONG JET AXIS

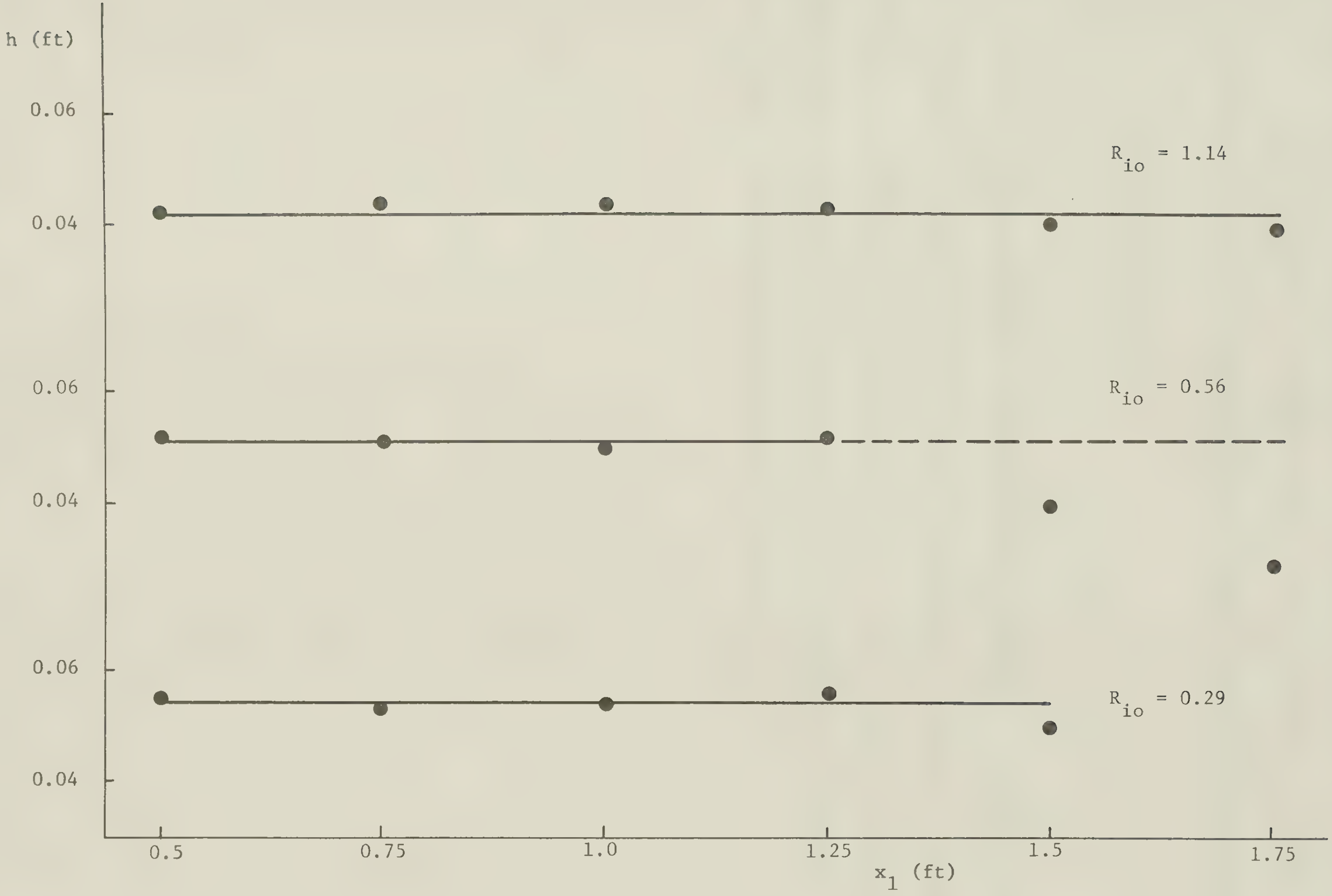

FIGURE 4.38 VARIATION OF HALF-DEPTH WITH DISTANCE ALONG JET AXIS

important role even at this value of R_{io}. A corresponding dimensionless plot is shown in Figure 4.39.

In order to determine the effect of cross flow on the depth scale, we define a depth coefficient C_h as:

$$\frac{h}{h_o} = C_h \, (R_{io})^{-1/8}$$

for large and moderate Richardson number. Table 4.6 gives the values of C_h for different velocity ratio. Figure 4.40 is a plot of C_h against $1/\alpha$. C_h can be taken approximately as 0.3 for all $1/\alpha$ within the range of large and moderate Richardson numbers.

LARGE R_{io}

EXP NO	R_{io}	$1/\alpha$	C_h
PANDE		0	0.26
1	0.75	0.42	0.29
5	1.14	0.13	0.29

MODERATE R_{io}

EXP NO	R_{io}	$1/\alpha$	C_h
PANDE		0	0.30
4	0.29	0.06	0.31
6	0.56	0.09	0.32

Table 4.6 Values of Half-Depth Coefficient

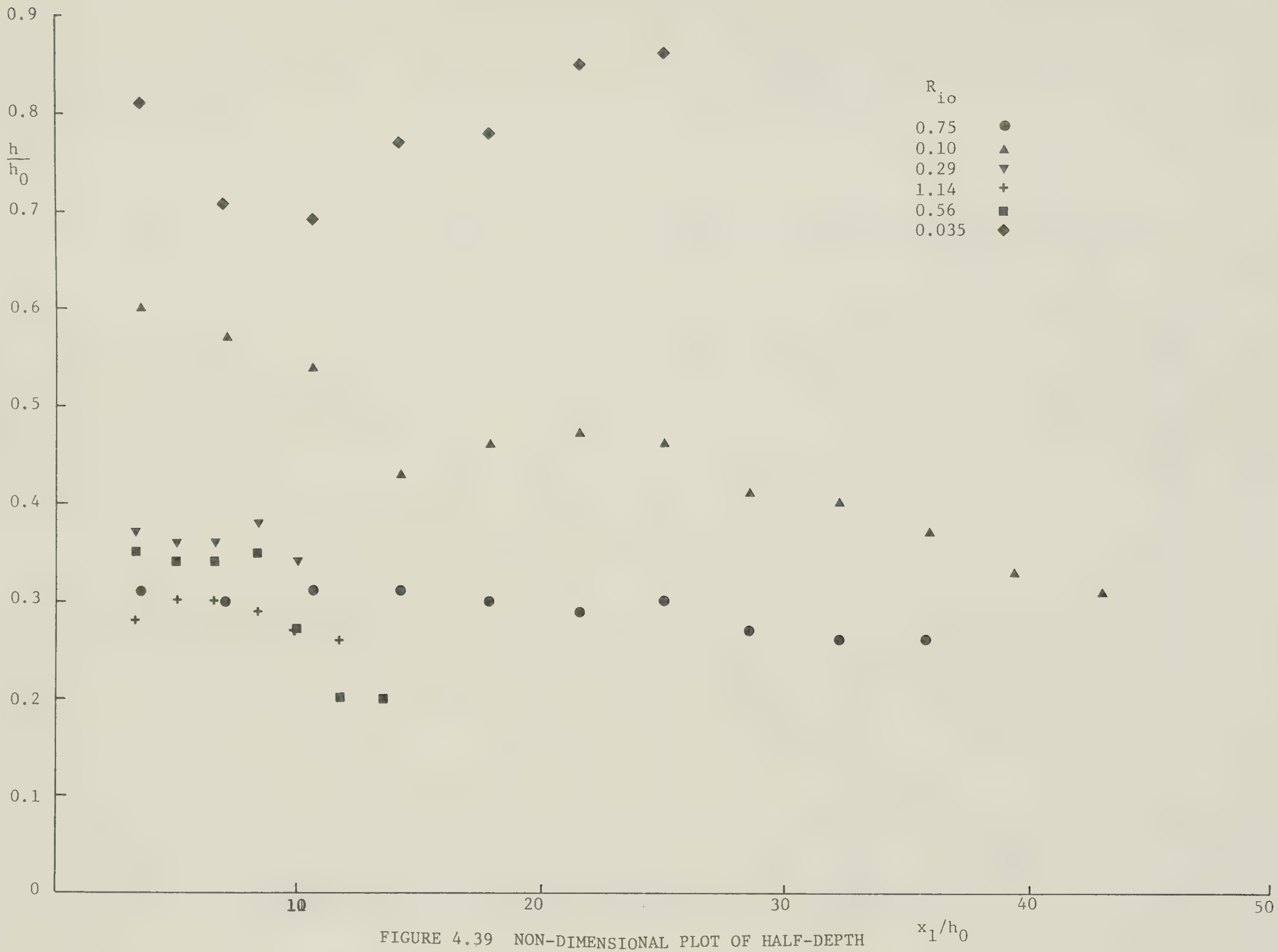

FIGURE 4.39 NON-DIMENSIONAL PLOT OF HALF-DEPTH

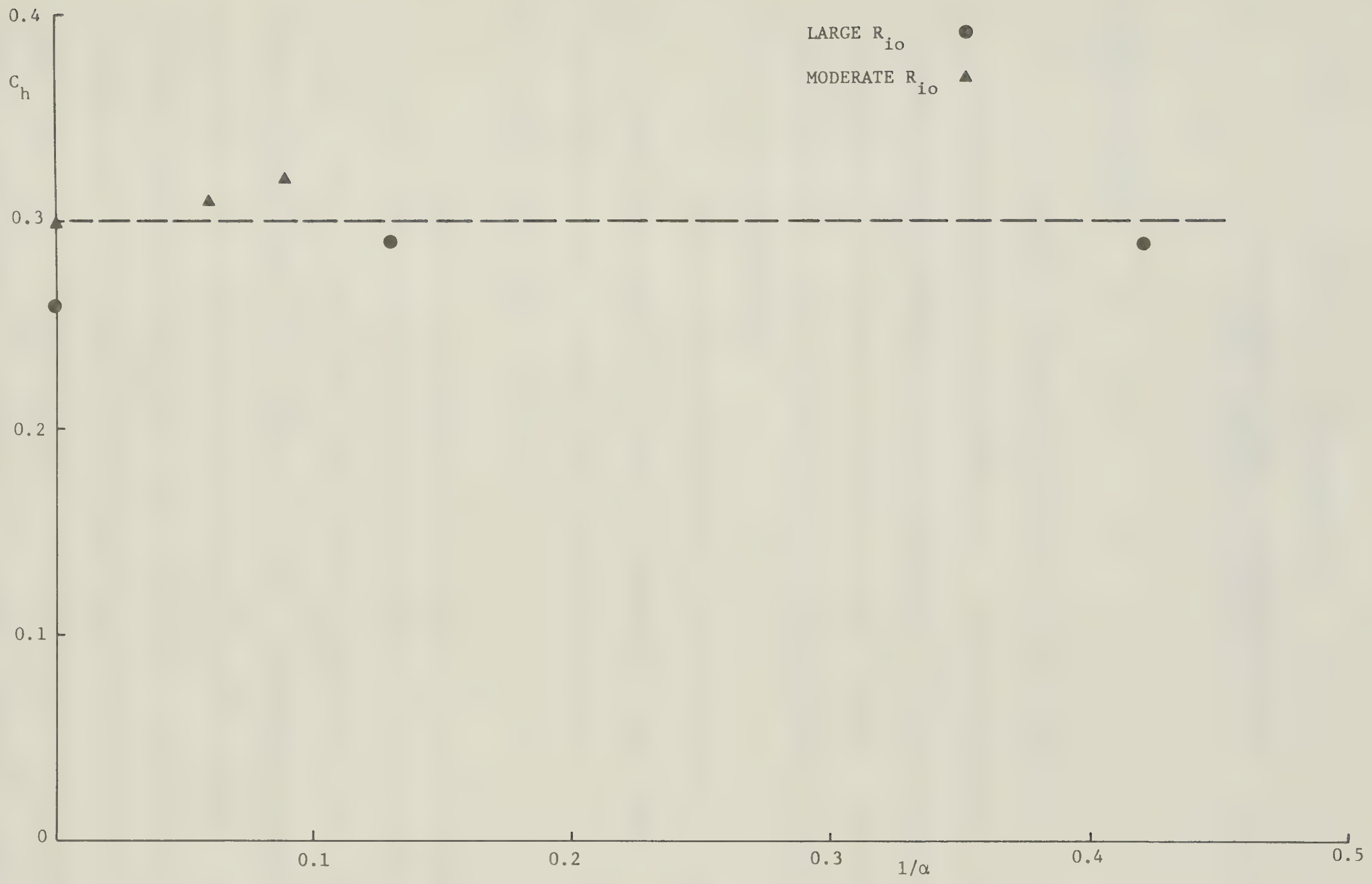

FIGURE 4.40 CORRELATION OF DEPTH COEFFICIENT WITH VELOCITY RATIO

CHAPTER 5

CONCLUSIONS AND RECOMMENDATIONS FOR FURTHER RESEARCH

Conclusions

Thermal discharges from power plants are capable of causing considerable damage to our environment. A thorough understanding of the behavior of the surface discharge is necessary to minimize its impact on the environment and also to maintain the efficiency of the power plant cooling system.

Based on the results of six experiments (with two experiments each for small, moderate, and large Richardson number groups) with cross-currents, the following conclusions are drawn:

The excess temperature profiles in the lateral and vertical directions have been found to be similar and could be described either by the exponential curve or the Schlichting-type distribution. But the excess temperature profiles on the upstream side, even though similar, are strongly distorted by the cross-current; and neither the exponential curve nor Schlichting-type distribution could describe them satisfactorily. The decay of the centerline excess temperature is affected to some extent by the

strength of the cross-current. The temperature generally drops off very rapidly within a short distance from the inlet and then decreases gradually to the ambient temperature. The jet trajectories depend strongly on the velocity ratio. Though the symmetry of the jet is affected by the existence of the cross-flow, the ratio of the jet spreading on either side of the jet centerline to the total width of the jet at any cross-section remains approximately invariant in the axial direction. This ratio depends on the velocity ratio as well as on the Richardson numbers. Further, it has been found that:

for small Richardson number:

$$\Delta T_m \propto \frac{1}{x_1} \qquad b \propto x_1$$

for large Richardson number:

$$\Delta T_m \propto \frac{1}{x_1^{2/3}} \qquad b \propto x_1 \qquad h \propto x_1^{o}$$

and for moderate Richardson number:

$$\Delta T_m \propto \frac{1}{x_1^{2/3}} \qquad b \propto x_1^{4/3} \qquad h \propto x_1^{o}$$

The coefficients in the above equations have been found to be functions of the velocity ratio.

Suggestions for Further Research

The surface spreading of the heated jet with cross-currents should be studied in more detail with measurements of the velocity field. Further, for each Richardson number group, a few more velocity ratios should be investigated.

REFERENCES

1. Abraham, G. "Jet Diffusion in Stagnant Ambient Fluid". Publication No. 29, Delft Hydraulics Laboratory, July 1963.

2. Abramovich, G.N. "The Theory of Turbulent Jets". M.I.T. Press, Cambridge, Massachusetts, (English Translation) 1963.

3. Albertson, M.L., Dai, Y.B., Jensen, R.A. and Rouse, H. "Diffusion of Submerged Jets". Trans. ASCE, Volume 115, 1950, pp. 639-697.

4. An Energy Policy for Canada, Volume I. Analysis issued under the authority of the Ministry of Energy, Mines and Resources, Information Canada, Ottawa, 1973.

5. Asbury, J.G. and Frigo, A.A. "A Phenomenological Relationship for Predicting the Surface Areas of Thermal Plumes in Lakes". ANL/ES-5, April 1971.

6. Chu, V.H., and Goldberg, M.B., "Buoyant Forced-Plumes in Cross Flow". Journal of the Hydraulic Division, ASCE, September 1974. pp. 1203-1214.

7. Chu, V.H., and Vanvari, M.R., "Experimental Study of Turbulent Stratified Shearing Flow". Journal of Hydraulics Division. ASCE, June 1976, pp. 691-706

8. Elliot, R.V. and Harkness, D.G. "A Phenomenological Model for the Prediction of Thermal Plumes in Large lakes". Proceedings, 15th Conference on Great Lakes & Reservoirs, International Association of Great Lakes and Reservoirs, 1972, pp. 544-564.

9. Ellison, T.H. and Turner, J.S. "Turbulent Entrainment in Stratified Flow". Journal of Fluid Mechanics, Volume 6, Part 3, October 1959, pp. 423-448.

10. Engelund, F. and Pedersen, F.B. "Surface Jet at Small Richardson Numbers". Journal of the Hydraulics Division, ASCE, Volume 99, No. HY3, Proc. Paper 9588, March 1973, pp. 405-416.

11. Engelund, F. "Hydraulics of Surface Buoyant Jet". Journal of the Hydraulic Division, ASCE, Volume 102, No. HY9, September 1976, pp. 1315-1326.

12. Fan, L.N. "Turbulent Buoyant Jets into Stratified or Flowing Ambient Fluids". W.W. Keck Laboratory of Hydraulics & Water Resources, Report No. KM-R-15, California Institute of Technology, 1967.

13. Harleman, D.R.F. "Stratified Flow". Section 26, Handbook of Fluid Dynamics, Edited by V.L. Streeter, McGraw-Hill Book Company, 1961.

14. Heinz, J.O. "Turbulence". McGraw-Hill Book Company, 1959.

15. Wiegel, R. and Mobarek, I. "Surface Discharge of Horizontal Warm Water Jets". Journal of Power Division, ASCE, Volume 92, PO2, April 1966, pp. 1-30.

16. Kenney, B.C. "The Physical Effects of Waste Heat Input to the Great lakes". Scientific Series No. 28, Inland Waters Directorate, Canada Centre for Inland Waters, Burlington, Ontario, 1973.

17. Koh, R.C.Y. "Two Dimensional Surface Warm Jets". Journal of the Hydraulic Division, ASCE, Volume 97, No. HY6, Proc. Paper 8186, June 1971, pp. 819-836.

18. Morton, B.R., Taylor, G.I. and Turner, J.S. "Turbulent Gravitational Convection from Maintained and Instantaneous Sources". Proceedings, Royal Society of London, London, England, Series A, Volume 234, 1956, pp. 1-23.

19. Motz, L.H. and Benedict, B.A. "Heated Surface Jet Discharged into a Flowing ambient Stream". Department of Environmental and Water Resources Engineering, Vanderbilt University, Nashville, Tennessee, Report No. 4, August 1970.

20. Paddock, R.A., Policastro, A.J., Frigo, A.A., Frye, D.E. and Tokar, J.V. "Temperature and Velocity Measurements and Predictive Model Comparisions in the Near-Field Region of Surface Thermal Discharges". ANL/ES-25.

21. Pande, B.B. Lal "A Theoretical and Experimental Study of Heated Surface Discharges into Quiescent Ambient". Ph.D. Thesis, University of Alberta, Edmonton, Fall 1975.

22. Pani, B.S. "Three Dimensional Wall Jets". Ph.D. Thesis, The University of Alberta, 1972.

23. Parker, F.L. and Krenkel, P.A. "Engineering Aspects of Thermal Pollution". Vanderbilt University Press, 1969.

24. Policastro, A.J. and Tokar, J.V. "Heated Effluent Dispersion in Large Lakes: State of the Art of Analytical Modelling. Critique of Model Formulations". Argonne National Laboratory, ANL-ES-11, Center for Environmental Studies, 1972.

25. Pratte, B.D., and Baines, W.D., "Profiles of the Round Turbulent Jet in a Cross Flow". Journal of the Hydraulic Division, ASCE, November 1967, pp. 53-64.

26. Rajaratnam, N. and Pani, B.S. "Three Dimensional Turbulent Wall Jets". Proc. ASCE, Journal of the Hydraulic Division, January 1974, pp. 69-83.

27. Rajaratnam, N. and Gangadhariah, T. "Circular Jets in Cross-Flow". Technical Report, Department of Civil Engineering, The University of Alberta, Edmonton, 1975.

28. Schubauer, G.B. and Tchen, C.M. "Turbulent Flow". Princeton Aeronautical Paperbacks, Princeton University Press, New Jersey, 1961.

29. Schlichting, H. "Boundary Layer Theory". McGraw Hill Book Company, New York, 1968.

30. Stolzenbach, K.D. and Harleman, D.R.F. "An Analytical and Experimental Investigation of Surface Discharges of Heated Water". Ralph M. Parson's Laboratory, M.I.T., Cambridge, 1971.

31. Stefan, H. and Schiebe, F.R. "Heated Discharge from Flume Into Tank". Journal of the Sanitary Engineering Division, ASCE, Volume 96, No. SA6, Proc. Paper 7762, December 1970, pp. 1415-1453.

32. Stefan, H. and Vaidyaraman, P. "Jet Type Model for the Three Dimensional Thermal Plume in a Cross Current and Under Wind". St. Anthony Falls Hydraulic Laboratory, Water Resources Research, Technical Paper No. 58, Series A, Volume 8, No. 4, August 1972, pp. 998-1014.

33. Tamai, N., Weigel, R.L. and Tornberg, G.F. "Horizontal Surface Discharges of Warm Water Jets". Journal of the Power Division, ASCE, Proc. Paper 6847, Volume 95, No. PO2, October 1969, pp. 253-276.

34. Townsend, A.A. "The Structure of Turbulent Shear Flow". Cambridge University Press, Cambridge, England, 1956.

35. Wygnanski I., and Fiedler, H., "Some Measurements in the Self-Preserving Jet". Journal of Fluid Mechanic, 1969, Volume 38, Part 3, pp. 577-612.

36. Zeller, R.W., Hoopes, Z.A. and Rohlich, G.A. "Heated Surface Jets in Steady Cross Current". Journal of the Hydraulics Division, ASCE, Volume 97, No. HY9, Proc. Paper 8385, September 1971, pp. 1403-1426.

APPENDIX

PROBE	Calibration Equations
1	$T = 9.8902 + 13.176V^{1.0620} + 0.15236V^{4.3104}$
2	$T = 9.9284 + 13.161V^{1.0746} + 0.10093V^{4.7125}$
3	$T = 9.9385 + 13.016V^{1.0340} + 0.27048V^{3.8399}$
4	$T = 9.9117 + 13.109V^{1.0067} + 0.39729V^{3.4821}$
5	$T = 9.8939 + 13.131V^{0.9879} + 0.43671V^{3.4364}$
6	$T = 9.9361 + 13.138V^{1.0348} + 0.25909V^{3.8411}$
7	$T = 9.9211 + 12.787V^{1.0125} + 0.47769V^{3.3510}$
8	$T = 9.9166 + 12.669V^{1.0040} + 0.72725V^{2.9531}$
9	$T = 9.8836 + 13.011V^{0.9903} + 0.50089V^{3.3110}$
10	$T = 9.9084 + 13.119V^{1.0424} + 0.20069V^{4.1053}$
11	$T = 9.9229 + 13.231V^{1.0474} + 0.17087V^{4.2224}$
12	$T = 9.9283 + 13.020V^{1.0374} + 0.26541V^{3.8470}$
13	$T = 9.9332 + 13.189V^{1.0348} + 0.22638V^{3.9740}$
14	$T = 9.9041 + 13.093V^{1.0041} + 0.41065V^{3.4607}$
15	$T = 9.9210 + 12.566V^{0.9738} + 0.88904V^{2.8314}$
16	$T = 9.8923 + 13.182V^{1.0690} + 0.13126V^{4.4396}$

Table A-1 Calibration Equations for Thermistor Probes

R_{io}	0.75		0.10		0.035		0.29		1.14		0.56	
x_1	T_{mu}	T_{md}	T_{mu}	T_{md}	T_{mu}	T_{md}	T_{mu}	T_{md}	T_{mu}	T_{md}	T_{mu}	T_{md}
0.5			15.0	13.1	11.8	10.2	6.1	7.1	4.9	4.9	7.5	5.2
0.75							3.8	4.8	3.6	3.8	6.4	4.1
1	10.9	7.6	12.0	9.6	8.3	6.7	3.2	4.0	3.0	2.6	5.4	3.0
1.25							2.1	2.9	2.2	2.2	4.9	2.6
1.5	10.2	7.1	8.4	5.7	5.7	3.8	2.0	2.4	1.8	1.8	4.6	2.3
1.75									1.3	1.3	4.3	2.0
2	9.4	6.4	7.1	4.5	5.5	3.6						
2.5	8.8	5.7	5.8	3.2	4.6	2.6						
3	7.9	4.8	5.6	2.8	4.0	2.3						
3.5	7.2	4.6	5.1	2.5	3.5	1.6						
4	6.4	4.0	4.9	2.1	3.4	1.6						
4.5	6.2	3.7	4.7	1.8	3.1	1.1						
5	5.7	3.1	4.6	1.6								
5.5	5.4	2.6										
6	5.2	2.3										
6.5	5.1	2.3										

Table A-2 Measured Excess temperature Decay($^{\circ}$C) Along Jet Centerline on Surface

R_{io}	0.75		0.10		0.035		0.29		1.14		0.56	
x_1	b_u	b_d	b_u	b_d	b_u	b_d	b_u	b_d	b_u	b_d	b_u	b_d
0.5			0.55	0.47	0.35	0.27	0.24	0.42	0.42	0.60	1.20	0.60
0.75							0.42	0.82	1.08	0.60	2.85	0.58
1	0.80	1.05	1.05	0.66	0.72	0.61	0.60	1.05	1.60	1.07	3.22	0.75
1.25							0.98	1.50	2.05	0.60	3.50	0.80
1.5	1.05	1.35	1.68	0.94	1.44	1.00	1.12	1.70	2.17	0.60	4.28	0.80
1.75									0.50	0.54		0.72
2	1.56	1.60	2.15	1.06	1.92	1.05						
2.5	1.55	1.94	2.35	1.21	2.10	1.11						
3	1.70	2.15	2.57	1.46	1.94	1.09						
3.5	1.70	1.92	2.43	1.60	1.85	1.09						
4	0.94	2.25	2.42	1.77	1.74	1.09						
4.5	1.20	2.24	2.40	1.55	1.62							
5	0.73	2.07	2.37	1.55								
5.5	0.74	1.84										
6	0.94	1.70										
6.5	1.13	1.57										

Table A-3 Measured Half-Width(ft) at Surface

R_{io}	0.75	0.10	0.035	0.29	1.14	0.56
x_1	h(ft)					
0.5	0.044	0.084	0.114	0.055	0.042	0.052
0.75				0.053	0.044	0.051
1	0.042	0.080	0.099	0.054	0.044	0.050
1.25				0.056	0.043	0.052
1.5	0.044	0.075	0.096	0.050	0.040	0.040
1.75					0.039	0.029
2	0.043	0.060	0.108			0.030
2.5	0.042	0.064	0.108			
3	0.041	0.066	0.119			
3.5	0.042	0.064	0.120			
4	0.038	0.058	0.124			
4.5	0.036	0.056	0.135			
5	0.037	0.052	0.134			
5.5		0.046				
6		0.044				

Table A-4 Measured Half-Depth along Jet Trajectory

B30169